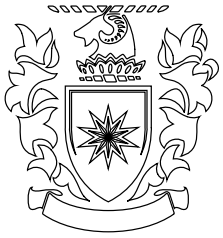

Controlled Synthesis of Silver Nanostructures for use in Surface-Enhanced Raman Spectroscopy

A thesis presented in partial fulfilment of the requirements for the degree of

Master of Science

in

Nanoscience

Supervised by:
Prof. Mark Waterland
Prof. Bill Williams

Sam Otter
January 25, 2022

School of Fundamental Sciences
Massey University
Palmerston North, New Zealand

Abstract

Surface-enhanced Raman scattering (SERS) has been extensively researched in the past few years, with further research being done into the development of noble metal substrates that have been shown to drastically increase the enhancement provided by SERS. Noble metals are exceptionally good at enhancing Raman signals stemming from their innate optical properties. The innate enhancement factor of these noble metals has been essential for SERS research, as without them, the appearance of SERS peaks will be indistinguishable from the background noise. Research has shown that the Raman enhancement provided by noble metals substrates can be improved upon by using controlled, uniform nanostructures with sharp corners and edges instead of standard substrates or heterogeneous mixtures of random nanoparticles. Both silver and gold have been shown to adopt several unique nanostructure shapes ranging from nanocubes to complex nanoflowers. This thesis discusses the synthesis and characterization of three novel silver nanostructures along with the results of using the nanostructures in a variety of Raman spectroscopy experiments. The nanostructures produced were nanocubes, nanoplates and nanowires with all three being used as substrates in several solution based Raman spectroscopy experiments, which included conventional SERS, single molecule SERS, microfluidic SERS and Raman tweezers. The primary hypothesis of the project is that different regions of the substrate will provide different degrees of enhancements due to a difference in localized surface plasmon resonance (LSPR) intensity. In the case of the nanostructures used in this project, there should be a difference in LSPR between the face, edges and corners of the three structures, as each region will contain different degrees of LSPR interaction. To test this hypothesis the data collected from the SERS experiments was processed using several statistical analysis techniques, including Euclidean distance mapping, principal component analysis (PCA) and self-organizing mapping, to test the validity of the hypothesis. For this hypothesis to be correct the data should fit into a discrete number of groups that represent the different regions of the substrate. The experimental data did not appear to support the original hypothesis, indicating that a more nuanced explanation may be required to describe the generation of SERS signal from controlled substrates.

Acknowledgements

I would like to thank my supervisors, Professor Mark Waterland and Professor Bill Williams, for their advice and guidance in the project. I would also like to thank the members of the Manawatu Microscopy & Imaging Centre for their support in this project and their assistance in collecting the TEM images shown in this thesis. Last, but not least, I would like to thank my colleagues, Sam and Andre, for their help in this project as well as my friends and family for their continued support.

Contents

List of Figures

List of Tables

List of Acronyms

Cetrimonium chloride	CTAC
Crystal Violet	CV
Diethylene Glycol	DEG
Ethylene Glycol	EG
Hydrochloric Acid	HCl
Hydrogen Peroxide	H_2O_2
Iron Chloride	$FeCl_3$
Localized Surface Plasmon Resonance	LSPR
Oxygen	O_2
Polyvinylpyrrolidone	PVP
Principal Component Analysis	PCA
Rhodamine 6G	R6G
Self-organizing Map	SOM
Silver Chloride	AgCl
Silver Nanostructures	AgNS
Silver Nitrate	$AgNO_3$
Silver Trifluoroacetic Acid	CF_3COOAg
Single-molecule Surface-enhanced Raman Scattering	SMSERS
Sodium Borohydride	$NaBH_4$
Sodium Hydrosulfide	NaHS
Sulfuric Acid	H_2SO_4
Surface-enhanced Raman Scattering	SERS
Tetraethylene Glycol	TTEG
Transmission Electron Microscopy	TEM
Trisodium Citrate	TSC
Water	H_2O

Prologue

Hypothesis

The main hypothesis of this project was concerned with determining if a SERS signal for a dye molecule could be altered by the substrate providing the enhancement. As part of testing this hypothesis a theory was formulated as to whether the region at which the dye molecule adhered to on the substrate impacted the SERS signal produced. A uniform crystalline substrate will contain different regions which have greater LSPR interactions that may influence the SERS signal of a dye molecule depending on which region it adhered to. This theory proposes that SERS spectra may be distinguishable from each other based on the location of the dye molecule on the substrate, based on this difference in LSPR. The three nanostructures were chosen for their differences in crystal structure, with each offering a different ratio of the three primary regions of interest, regarding LSPR interactions. These regions of interest include crystal faces, edges, and corners, with each of which having different amounts of LSPR intersections, faces having a single LSPR, edges containing two, and corners containing three. As the project is focused on specific nanostructure shapes, there were requirements around the nanostructures produced. The nanostructures need to be a constant size and shape to ensure that the SERS data being collected can be equated to the properties of the nanostructure. The theory posits that a dye molecule adhered to each of these regions will produce a SERS signal that is different enough to become distinguishable from other signals. The difference in signal may be caused the expression weaker vibrational modes of the dye molecules when they are adhered to high energy regions on the substrate. This assumption should result in the appearance of a discrete number of clusters in the spectra based on the number of different regions available on the substrate, for SERS spectra collected within the single molecule region, where only one dye molecule is present on a substrate. This hypothesis

was supported by work done by Jensen that investigated the shift in the LSPR wavelength of Ag nanoparticles upon R6G binding.[1] This shift in LSPR was found to be dependent on the relative spectral position between the AgNS LSPR and the molecular resonance of R6G. It was found that the LSPR wavelength of Ag nanostructures had an extreme sensitivity to small environmental changes in the binding position of R6G molecules. This level of sensitivity illustrates the possibility of detecting molecular level information, such as structural changes in the adsorbents and the location at which they adsorb.[2]

An alternative hypothesis was a theory that proposed that the different regions of LSPR intensity do play a role in enhancing different/weaker vibrational modes, but instead of the formation of a discrete number of groupings, that instead a continuum of different spectra will be present. This continuum would contain an array of spectra, each very similar but with a constant change in which modes are enhanced, with one end of the array containing spectra with only the most easily expressible modes being present, while the other end contains spectra will all available modes expressed. Unlike the clustering theory, the continuum theory should result in the spectra forming a long string of data points when visualised, given the progressively small differences between neighbouring spectra. The thinking behind this theory is like the clustering theory, where the different regions of the substrate will provide different amounts of enhancement based on the number of LSPR interactions at these regions. The difference between the theories stems from the idea that there will be variance in the amount of enhancement provided at the different regions, not a static amount which was assumed for the clustering theory. The cause of this variance could be due to fluctuations in the LSPR present at the different regions.

Research Aims

The goal of this research is to investigate whether different nanostructures provide different SERS signal based on the location at which the dye molecule is adhered to. To achieve this, several more specific aims were established to compartmentalise the project. These include:

- The synthesis of a variety of Ag nanostructures that contain distinctly different

crystal structures.

- Using said nanostructures as Raman substrates to collect both SERS and SMSERS spectra.
- The development of plasmonic optical Raman tweezers to enable the collection of SERS signal from a single molecule adhered to a single substrate crystal.

CHAPTER 1

Introduction

1.1 Raman Spectroscopy

Raman spectroscopy is a powerful, non-destructive chemical analysis technique that can probe the vibrational fingerprints of molecules. This allows for the analysis of simple and complex composite systems to determine chemical, physical, and biological aspects and has been used for chemical detection and environmental monitoring.[3, 4] The weakness of Raman spectroscopy is that it suffers from low sensitivity, due to only a small portion of light used in the collection of data undergoing any Raman scattering, resulting in a very weak signal. When a scattering sample is irradiated with monochromatic light, most of the light is transmitted with no change to its wavelength or energy, but some scattering occurs as the light interacts with the sample. When analysing the wavenumber component of the scattered portion of light there will be components associated with the incident light and components that have been shifted based on the rotational, vibrational, and electronic levels of the sample being irradiated. Raman scattering can be explained in terms of an energy transfer system, between the sample and the incident light source. When a scattering source is irradiated with incident light of a specific wavenumber, there is a transition from a ground energy state to a virtual state. For this transition to occur the incident radiation must have sufficient energy and be at a specific wavelength. The energy requirement is regarded as the absorption of a photon from the incident radiation with the simultaneous emission of a photon from the scattering system at a smaller energy, resulting in the emitted photon having a lower wavenumber than the incident photon. The alternative to this can also occur, where the emitted photon is at a

higher wavenumber than the incident photon. This situation occurs when the incident radiation interacts with a scattering system that causes a net downward transition from a higher energy level to a lower level. These scattering events occur roughly once every million photons interacting with the scattering system, with most photons undergoing Rayleigh scattering. Rayleigh scattering occurs when an incident photon is absorbed by the scattering system while **simultaneously** emitting a photon of equal energy, resulting in no change in wavenumber between the incident and emitted photons. A Raman band is characterized by the difference between the incident radiation and the emitted radiation, and these shifts being known as Raman shift. It is important to distinguish between the lower energy emitted photons (Stokes Raman Scattering) and the higher emitted photons (anti-Stokes Raman Scattering) as the intensity of anti-Stokes compared to Stokes Raman scattering decreases with the increase in Raman shift (Figure 1). This is because the anti-Stokes Raman scattering must start from a vibrationally excited-state, with the excitation being provided by thermal energy which causes the resulting Boltzmann distribution to have control over the relative intensities of both Stokes and anti-Stokes lines. Raman scattering occurs for every vibrational mode that generate a significant change in the molecular polarizability. The scattering intensity can then be plotted against the Raman shift to produce a Raman spectrum.

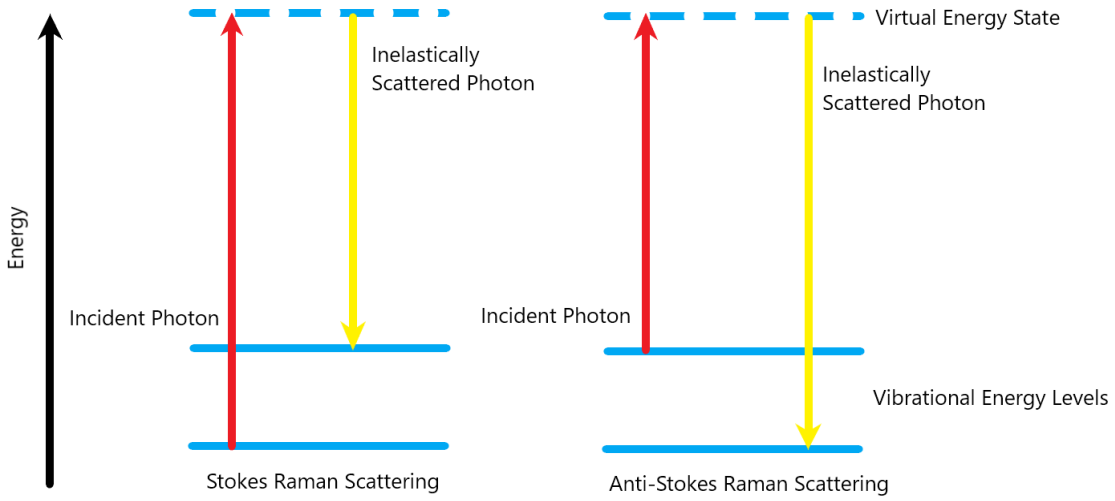

Figure 1: Diagram of the Stokes (left) and Anti-Stokes Raman (right) scattering

1.1.1 Surface-enhanced Raman Spectroscopy

To overcome the inherit weakness of a normal Raman scattering signal, techniques were developed to improve the intensity of Raman scattered light. The most common of these techniques is Surface-enhanced Raman Spectroscopy (SERS), which introduces a roughened or nanostructured metallic surface, causing the formation of localized surface plasmon resonance fields when excited from a radiation source. These localized surface plasmons are enhanced electrical fields that are capable of enhancing the Raman signal of molecules adhered to the surface close to where a surface plasmon is formed. This enhancement boosts the Raman signal to such an extent that detection of molecules at considerably lower concentrations becomes possible, thus overcoming one of the limitations of conventional Raman spectroscopy. It is believed that SERS enhancement is caused by two underlying mechanisms, one being an electromagnetic mechanism and the other being a chemical mechanism.[5, 6] Both the electromagnetic and chemical enhancement can be described as resonances with different electronic states of the plasmon-molecule system.[7] The key feature of this model is its ability to account for interactions between the plasmon and molecule states which are required to correctly describe the wavelength dependence of SERS.

The electromagnetic mechanism stems from the enhanced electric field caused by the surface plasmons of the metallic surface used in SERS.[8] This enhanced electric field increases the number of photons interacting with the target molecules and will in turn increase the number of photons that undergo Raman scattering.[9] As SERS utilizes a rough or nanostructured surface, which results in the collective oscillation of the metallic substrates free electrons, causing a surface plasmon resonance which localizes and concentrates the incident photons at the surface of the SERS substrate.[10] In tandem with the electromagnetic mechanism is the chemical exchange mechanism that involves the charge transfer between the target molecule adhered to the SERS substrate and the metallic substrate. This charge transfer increases the polarizability of the target molecules on the SERS substrate, resulting in an increase in the Raman scattering experienced.[11] This theory has since been refuted with experimental results showing that change-transfer

does not provide a substantial contribution to SERS enhancement under most circumstances [12].

The choice of substrate plays a pivotal role in the degree of enhancement experienced, as different metallic and dielectric surfaces will produce surface plasmons with different degrees of intensity, impacting the polarizability the target molecules experience at the substrate surface. Both metallic and dielectric substrates have been investigated for their potential use as SERS substrates, with findings showing that metallic substrates provide considerably higher enhancement factors, upwards of 10^7, than dielectric substrates, but dielectric substrates do have other advantages, such as lower photothermal heat generation and improved biocompatibility over metallic substrates. [13] Of the possible metallic substrates, the noble metals offer the greatest enhancement, which has led to extensive research into their use as SERS and single-molecule SERS substrates, along with research into how to optimise the surface to achieve the greatest enhancement.[14] The unique properties of noble metals include optical field enhancements that result in strong scattering and absorption of light. This optical enhancement stems from the resonant oscillation of free electrons when radiated with light, i.e. the plasmon.[15] Outside of noble metals, other metals substrates provide excellent SERS enhancement, but have not received the same amount of research as noble metals. These compounds include aluminium and titanium oxide, both of which have displayed enhancement comparable to noble metals.[16, 17] Despite this, both titanium oxide and aluminium SERS substrates are not as commonly used as noble metals as they are more difficult to synthesis, often requiring complex reaction setups to achieve substrates close to those achieved with noble metals, and their respective reactivity can cause issues during experimentation.

The localized surface plasmon resonance (LSPR) of metallic nanostructures occur after the nanostructures are exposed to electromagnetic radiation, which causes the collective oscillation of their conduction electrons. Noble metals contain the some of the largest localized surface plasmon amplitudes and are often used in optical spectroscopy techniques for this reason. The LSPR amplitude is directly correlated with the selective photon absorption, scattering and local electromagnetic field enhancement provided by the metal when used as a substrate. The oscillation frequency of the conduction electrons

is determined by several factors including the density of electrons, the effective electron mass and the size and shape of the charge distribution.[18] It is for these reasons that the size of the LSPR amplitude can be manipulated by changing the size, shape, and structure of the metallic nanostructure. The LSPR of noble metals are also influenced by the electrons outside of the conduction band such as d-orbital electrons. This can lead to a larger LSPR amplitude for noble metals, as the inclusion of d-orbital electrons will increase the density of the electron cloud oscillating. The largest LSPR amplitude is found at sharp points on the nanostructures, such as edges and corners as they are the location of junction points between LSPRs, and for individually isolated nanoparticles. Strong LSPR intensity have been located at the edges and corners of nanocubes, with the largest enhancement being observed at corners.[19] These findings explain why nanostructured metals have such strong plasmon responses, as they are dominated by sharp edges, corners, and junctions. The shape of the nanostructure has been shown to greatly impact the LSPR intensity of the nanostructure, with large differences being measured between commonly used shapes such as nanocubes and nanobipyramids.[20] Because of the strong connection between SERS enhancement and the strength of a nanostructures LSPR, the shape of the nanostructure will affect the quality of SERS enhancement provided by the nanostructure.

For a SERS signal to be produced a Raman scattering sample needs to be near the substrate providing the enhancement, in the case of nanostructures in solution, ideally the scattering sample will be at a junction between two or more nanostructures. This poses an interesting situation for uniform nanostructures, like the ones produced in this project, as different regions on the crystal structure will have varying degrees of surface plasmon resonance, resulting in different levels of SERS enhancement. This situation has been investigated for nanocubes and provided insight into the difference in intensity experienced for a dimer of nanocubes producing SERS signal while at different orientations, face-face, face-edge etc [21]. As a distinguishable difference in SERS enhancement was recorded for nanocubes, it is plausible that other shapes, such as nanoplates and nanowires, will also experience a similar difference in enhancement that is controlled by their respective orientation. During the collection of SERS data using heterogeneous ir-

regular AgNS, which is common for generic SERS experiments, the SERS signal is an average of dye molecules adhered to the uncontrolled crystal faces of the nanostructures. Systems like these have a high degree of variance, as the lack of uniformity in nanostructure shape and sizes leads to an averaging effect caused by the dye molecules adhering to random positions on the nanostructures. The structures synthesised in this project remove a degree of variance, as the dye molecules can only adhere to a known number of crystals faces or edges/corners for each of the structures.

1.1.2 Single Molecule Surface-enhanced Raman Spectroscopy

Single-molecule SERS (SMSERS) has been an area of research that has seen significant interest, as it offers analytical detection of compounds at incredibly low concentrations, femtomolar to attomolar, that are unattainable using conventional Raman techniques.[22] The first recorded SMSERS study was reported in the 1990's and since this time has caused an influx in the development of new spectroscopic and nanoscience technology and techniques to optimise the newly discovered phenomena with the hopes of making it more readily accessible. Early SMSERS was believed to be observed by Nie and Emory who used SERS blinking inside of a colloidal solution as evidence.[23] This evidence has since been refuted as studies found that the blinking may have been occurring due to the diffusion of colloids in and out of the laser focus. The first definitive evidence towards SMSERS collection was provided by le Ru and Etchegoin.[24] The importance of conducting research into SMSERS stems from the advantages it has over conventional Raman and SERS analysis. Both Raman and SERS analysis can be thought of as being an average signal received from all the molecules present inside the focal volume of the laser. SMSERS effectively removes this averaging resulting in the ability to observe and experimentally verify the true homogeneous and inhomogeneous broadening of Raman peaks.[25] The ability to monitor a single molecule via SMSERS increases the range of SMSERS application as real-time monitoring of reactions at the single molecule level can now be achieved to better understand the reaction mechanism.[26] SMSERS is capable of probing the vibrational modes of single molecules adhered to the SMSERS surface, which provides high-content structural information about the individual molecule, that are usually averaged in Raman and SERS. During experimental SMSERS experiments there were observations of SERS in-

tensity fluctuations that were thought to be partially due to the instability in the SERS substrate surfaces. The movement and migration of SERS substrate surface molecules has been shown to influence the intensity of the SMSERS signal.[27] When the concentration of dye molecules reaches the single molecule regime it is believed that only one molecule is present inside the focal volume of the laser used to initiate Raman signal. SMSERS enhancement is caused by a combination of surface plasmon resonance based electromagnetic field formation of hotspots and a $\pi - \pi^*$ transition between the SMSERS substrate and the dye chemical. Given the low concentration of target molecules at single molecule concentration there is a probability that a single molecule can move through the measured volume without encountering a hotspot with sufficient enhancement. As such if there is continuous monitoring for SERS peaks inside the measured volume there would be an expected fluctuation in the SMSERS enhancement observed due to the dynamic motion of the single molecule as it travels through hotspots.[28]

1.2 Optical Tweezers

The trapping and manipulation of small particles by lasers is based around the radiation pressure forces provided by the laser that arises from the momentum of the light itself. Lasers can produce forces large enough to manipulate the position and velocity of small particles and even form stable traps for particles with optimal conditions. This force manipulation is a direct result of the high intensities and large intensity gradients available when using continuous wave coherent light beams. Laser trapping and manipulation has been achieved with a diverse range of particles sizes and compositions and provides an extra degree of control over the dynamics of the trapped particles.[29]

The optical trap is formed via the focusing of continuous wavelength laser through a microscope objective, where the narrowest point in the focused beam contains a strong electric field which attracts the dielectric particles and keeps them in the centre of the beam. The electric field contains two components, an axial component that acts to push the particle in the direction of the beam, and a gradient force that holds the particle at the focus. For successful trapping to occur the gradient force needs to be strong enough to overcome the effects of the axial force. The movement of laser light past the trapped particle

also induces a force on the particles in the direction of beam propagation as photons are absorbed/scattered by the particles, causing a change in their momentum. This propagation force leads to the dielectric particles becoming trapped slightly downstream of the exact middle of the beam centre.

1.3 Noble Metal Substrates

Gold and silver nanocrystals have seen extensive use as substrates in Raman spectroscopy experiments due to their optical transitions and surface plasmons in the visible region that are so intense that they cause a change in the local electromagnetic field. As a result of this, the coherent elastic Rayleigh light scattering is significantly stronger than larger non-noble metal nanocrystals. This leads noble metal nanocrystals to act as nanoantennas as they focus incident light into neighbouring molecules adhered to the surface of the substrate. As metallic nanocrystals are conductive, they contain no band gap, they can become extremely polarizable. Electromagnetic "hotspots" form at the intersections between nanocrystals. Surface molecules are commonly physisorbed to the surface of the nanocrystals, but chemisorption can occur if the nanocrystal and target molecule can undergo favourable bonding.[30] This adsorption leads to the Raman intensity enhancements being controlled by the coupling between the electronic transitions between the metal substrate and target molecule. A charge-transfer interaction can occur between the adhered molecule and the nanocrystal as the exchange of electrons between them becomes available during chemisorption, but is only dominate if the adhering molecule does not have a $\pi - \pi^*$ transition available.[11] This charge-transfer interaction can lead to metal plasmon excitation, which can result in a high enhancement factor as the surface of the nanocrystal dominates plasmon nonradiative relaxation. The surface plasmon of the nanocrystal is dictated by the oscillation of free electrons when outside of an electric field. This oscillation can be controlled by manipulating the shape and size of the nanocrystal, as well as the element the nanocrystal is made.[31] This can lead to the synthesis of nanocrystals with a surface plasmon resonance that have been designed to fit a certain region of the electromagnetic spectrum based solely off the physical characteristics of the nanocrystal.[32] As Raman spectroscopy is a major component of this project,

noble metals were selected as the substrate of choice as they fit best with the requirements of the project. Noble metals nanocrystals have been shown to have surface plasmon resonances in the visible region, meaning they can be excited using a visible laser beam that are commonly used in Raman spectroscopy, and can adopt a variety of novel morphologies, leading to fine control over the SPR by producing nanocrystals of specific sizes and shapes.[33] Both these features, combined with the innate optical properties of noble properties that are superior to most other transition metals, leads them to be the ideal metals for this project.[34] The choice between using gold or silver as the target substrate was resolved when consulting the literature surrounding noble metal SERS experiments. Many experiments that were concerned with specific nanocrystal sizes and shapes used gold as their metal as it was found to be more convenient than silver. Silver nanocrystals were found to be more difficult to work with, especially when both the size and shape of the crystals were trying to be controlled simultaneously. [35] A common problem faced with this type of synthesis is a poor yield in the target nanocrystal, with much of the product being amorphous, irregular nanocrystals. Conversely to this, gold is more forgiving and can readily form specific sizes and shapes while not suffering any degradation in yield. Additionally, when comparing the Raman enhancement of gold and silver, it has been shown that silver is a superior metal substrate choice, despite any difficulties that may be present in synthesis.[36] It is for these reasons that silver was selected over gold for this project, as it would act to fill an area of literature that has not been fully investigated.

1.3.1 Silver Nanostructures

To date, there has been considerable research into the synthesis of different shaped novel nanostructures due to their increased usage over a range of applications. This interest in silver nanostructures (AgNS) stems from silver's unique properties, ranging from optical,[37] catalytic,[38] and anti-bacterial.[39] It has been found that changing the size or the available surface of a silver nanoparticle will result in a change in its physical and chemical properties, leading to research being undertaken into forming new and different shapes.[40] The properties of interest for this project revolve around AgNS's large, LSPR and excellent performance in SERS, that have been shown to be improved when

the nanostructures contain sharp corners and edges.[41] To fully investigate the range of possible uses of AgNS, extensive research has been undertaken to demonstrate the synthesis of the many different types of AgNS. These range from spheres, nanocubes, and octahedra, to longer nanorods and nanowires, with different methods of synthesis being documented for each. There are additional challenges that arise when trying to produce a solution of nanostructures with a small size-distribution and consistent shape. The uniformity that is referred to during this report is concerned with the size-distribution and shape parameters of the nanostructures, with a high uniformity indicating a small size-distribution while maintaining the desired shape. Sharpness of features, including edges and corners, were also considered when determining the effectiveness of a particular method of synthesis, with high degrees of sharpness being the target. These challenges include typical synthesis problems of low yields and poor reproducibility but as the exact structure is trying to be controlled, uniformity of the nanostructures also becomes an issue, along with maintaining the shape of a nanostructure while trying to manipulate its size. The plasmon resonances of metallic nanostructures are strongly dependent on the morphology of the nanostructure, as its size, shape and composition impact the location and intensity of the surface plasmons that are required for SERS enhancement. The electromagnetic field enhancement reaches a maximum at positions where multiple surface plasmons meet, most commonly at corners or edges, and are commonly referred to as “hot spots”.[42] When under resonance conditions, the electromagnetic intensities found at these hotspots are orders of magnitude higher than the applied field intensity. The strength of these hotspots has been directly linked with the geometry of the substrate, leading to research into improving upon the hotspot intensity by engineering substrates with precise control over shape, size and most importantly edge and corner sharpness. The most common metallic SERS substrates are made from noble metals that usually adopt a pseudo-spherical shape when their structure is not controlled. When their structure is controlled, noble metals can adopt a range of shapes, including nanocubes, nanoplates, and nanowires. Each of these structures have different proportions of edge lengths, face sizes and number of corners, meaning that investigating them and comparing the results could provide evidence on the impact of the different structures on the

SERS intensity and whether the SERS signal produced can be distinguished from one another.

1.3.1.1 Nanocubes

Ag nanocubes (Figure 2) have been favoured over other Ag nanoparticle shapes due to the equidistant sharp edges, high number of edges and faces.[43] Ag nanocubes are single crystal Ag nanostructures that are capped by the [100] crystal facets, which leads to intersecting surface plasmons at the edges and corners of the nanocubes, causing exceptional SERS enhancement at these locations (Figure 3). Due to this enhancement there have been several studies concerned with using nanocubes for SERS and SMSERS experiments.[44] To understand the importance of hotspot generation, especially at corners, research into truncated nanocubes has been performed to show the impact of having sharp corners and the resulting hotspots that form at those locations.[41] The results of these pieces of research, along with many others, have shown the potential for nanocubes to be used in ultrasensitive SERS research due to the intensity of the enhancement they provide.

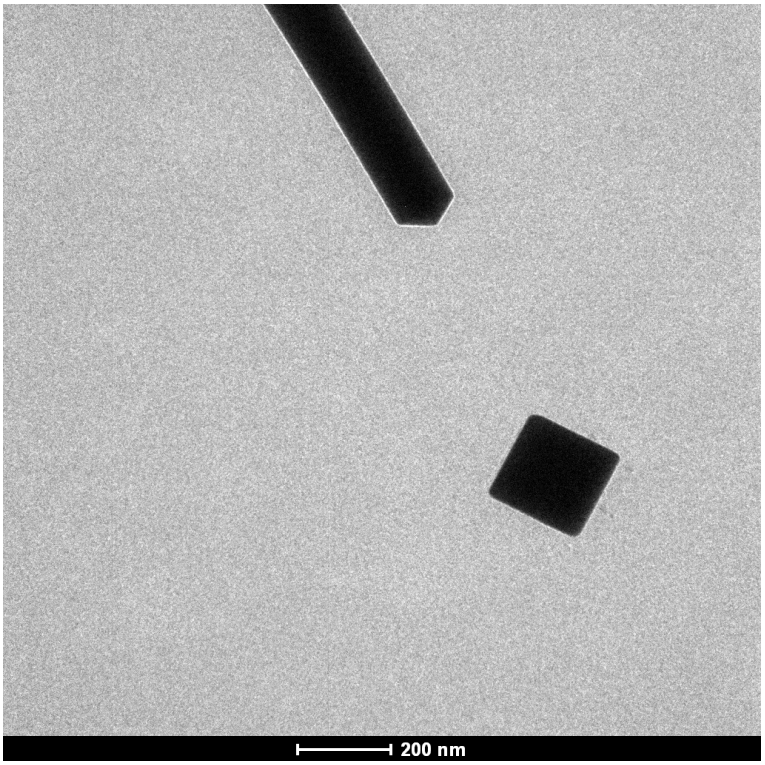

Figure 2: TEM image of a Ag Nanocube

Figure 3: Diagram of Surface Plasmon polaritons on Nanocubes. Sourced from [45]

1.3.1.2 Nanowires

Ag nanowires and nanorods (Figure 4) are two of the other commonly implemented nanostructures for SERS and can be used in comparison to other nanostructures, as their edge to corner ratio is heavily in favour of edges due to their elongated shape. Both nanowires and nanorods have been extensively researched and several methods of synthesis have been developed that result in the formation of uniform nanowires and nanorods with sharp corners and edges. Ag nanowires and nanorods are multiply twinned Ag nanostructures that are capped by [111] crystal facets (Figure 5).[46] It is often difficult to distinguish between nanowires and nanorods, as there are currently no clear specifications for differentiating them, but it is common practice to use the aspect ratio of the nanostructure's width to length ratio as a rough estimate as to whether the nanostructure is a rod or a wire.[47] Nanostructures with an aspect ratio of 1:8 or less are generally considered as nanorods while nanostructures above this aspect ratio are nanowires.[48] The high ratio of edge length to number of corners makes nanowires unfavourable for ultra-sensitive SERS research in comparison to nanocubes, but their extensive edge length ratio makes them suitable for a comparative study to see the impact structural features have on SERS intensity.[49]

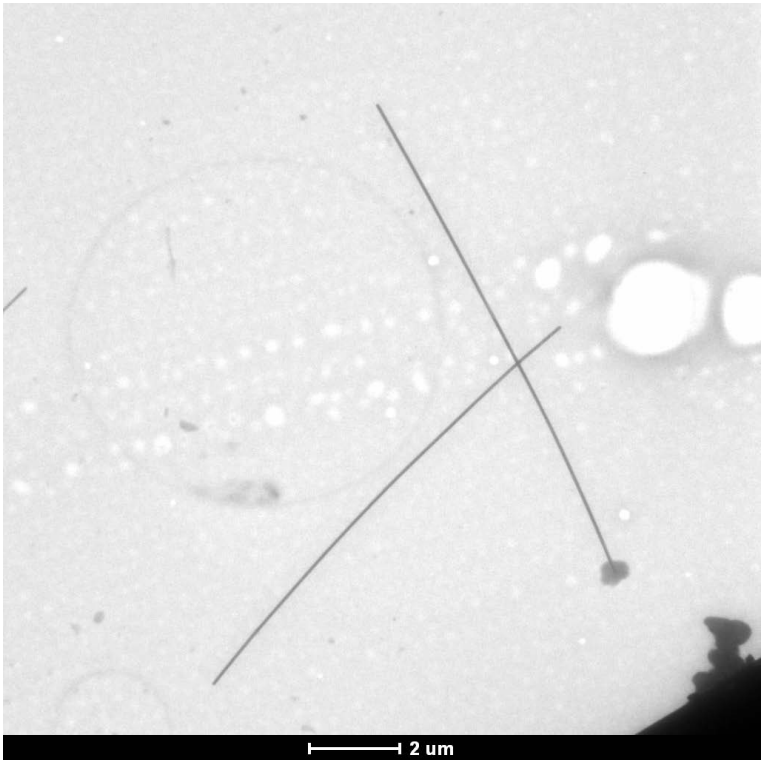

Figure 4: TEM image of Ag Nanowires

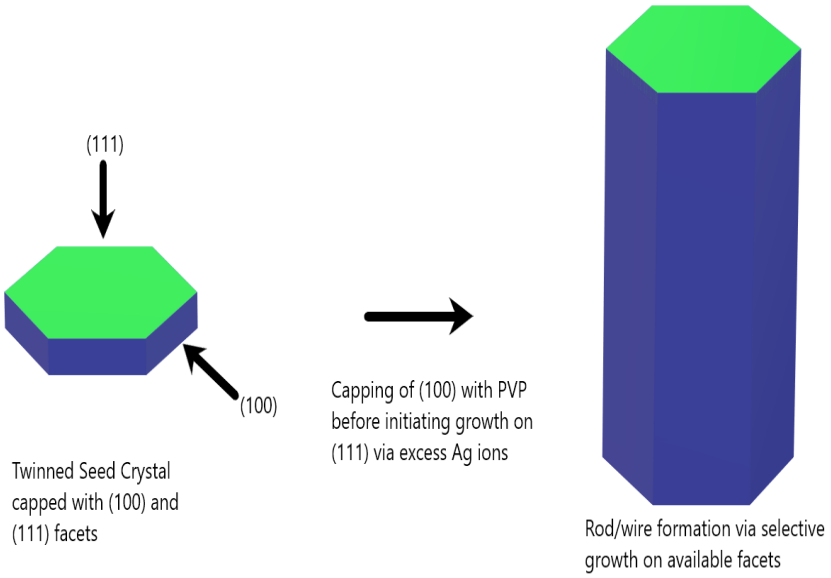

Figure 5: Conceptual diagram of Nanowire growth

1.3.1.3 Nanoplates

The final nanostructure type of interest are triangular nanoplates (Figure 6) that have a closer edge to corner ratio to nanocubes than nanowires, with a similar distribution between corners as seen in nanocubes. A feature that distinguishes a nanoplate from a nanocube is the distance between edges. Nanocube edges are equidistant on the face of every nanocube, while for the nanoplates the edge distance in the 'vertical' direction are

very close, which may allow for the possibility of strong interactions between the plasmon edge nodes. Ag nanoplates are twinned crystals that are capped by both the [111] and [100] crystal facets (Figure 7), resulting in the formation of sharp edges and corners at the intersections of these crystal facets. [50] The largest concern when using nanoplates as SERS substrates stems from their stability inside the collection SERS medium. The nanoplates themselves are often thin and prone to folding onto themselves, which can lead to them becoming damaged and possibly damage their SERS enhancement potential. This instability has led to nanoplates being less favoured compared with nanocubes for ultra-sensitive SERS studies, but they are still viable for conventional SERS studies as the corner and edge sharpness still produces substantial enhancement.[51]

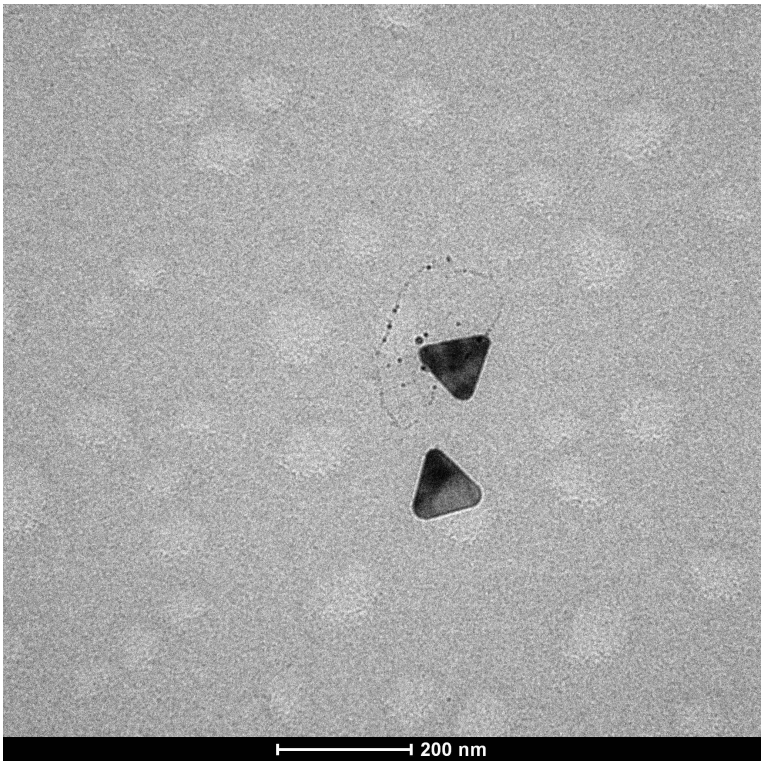

Figure 6: TEM image of Ag Nanoplates

1.4 Silver Nanostructure Synthesis

Controlling the exact size and shape of nanoparticles is a complex and difficult task as the desired products are often kinetically stable and not thermodynamically stable, meaning the structures being formed are only stable under specific experimental conditions. The presence of even a minute amount of trace metal or unwanted reagent will lead to the formation of an undesirable morphology.[52] As a means of overcoming these issues,

several methods of synthesis have been developed and documented for the majority of known AgNS. It is clear from a survey of the literature that identical results are rarely obtained by following a published procedure, minor (or major) modifications are often reported. These modifications are, presumably, required to optimise the previously published procedures for local laboratory conditions. To achieve results close to those seen in the literature the methodologies needed to be adapted to fit the available lab conditions and the reaction conditions needed to be held to extremely strict standards.

Literature has shown that the presence of trace metals, primarily Fe(II) and Fe(III), can interrupt the formation of nanocrystals by acting as etching agents and causing side reactions, resulting in the formation of irregular nanocrystals.[35] The adaptation made to the literature methods revolved around eliminating these trace metal ions and controlling the reaction conditions to the highest possible level, with the largest source of trace metal ion contamination found to be in the reagents. To overcome this, the reagents used during synthesis needed to be of the highest purity available to eliminate as much of the trace metals as possible.

In addition to this the other reactions conditions, mainly the glassware, reaction environment and preparation of reagents, needed to be held to a high level to mitigate any possible contamination. It was found, both through lab work and reviewing literature, that some of the reactions undertaken were sensitive to both H_2O and O_2, as both can act

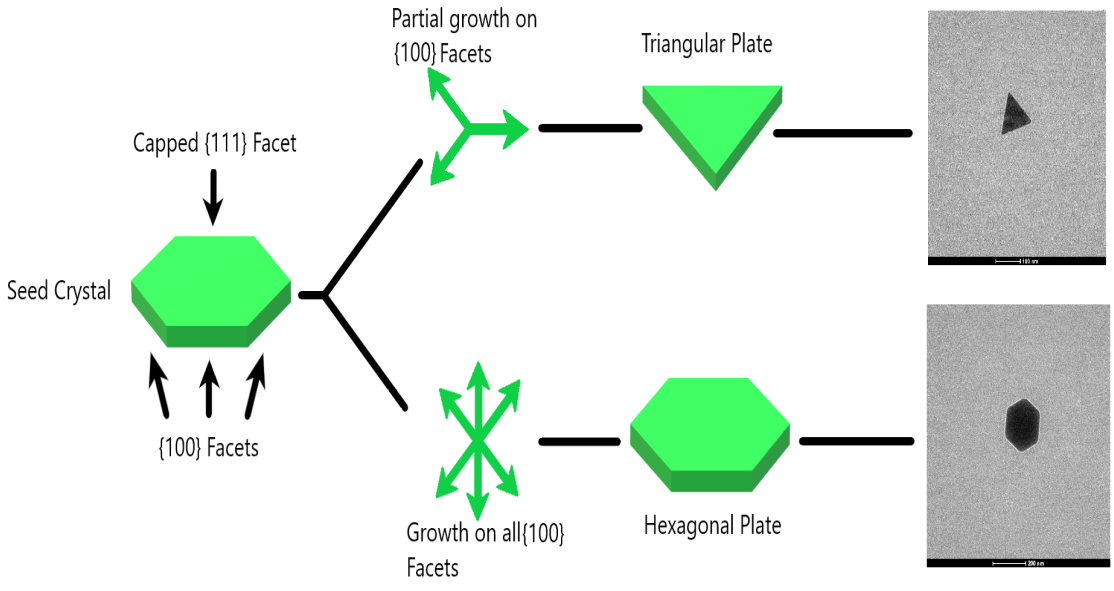

Figure 7: Nanoplate growth diagram

as etching agents which will impact the final shape of the AgNS being produced. The impact of H_2O and O_2 has been investigated using several experiments where H_2O and O_2 were selectively removed, either using anhydrous solvents and rigorous drying of glassware or through the purging of the reaction vessel and running the reaction itself under an inert atmosphere.[35] Oxygen's impact on the final structure of AgNS was insignificant compared to the impact of H_2O, leading to all future reactions of this type being conducted under anhydrous conditions.

The mechanism for AgNS synthesis is well documented and can be manipulated to produce different structures through altering the reactants used in the reaction and the medium in which the reaction is undertaken. The range of AgNS morphologies developed has expanded in previous years to include more intricate shapes that are often controllable over a range of sizes. The synthesis of each of these different morphologies follow similar methods of synthesis, with the biggest differences between them stemming from the initial structure of the seed crystals. The seed crystals are critical for nanostructure growth, as they act as a initial building block for the nanostructure to grow from. Depending on the desired final structure the seed crystals need to have a specific structure, either single or multiply twinned crystals. The available crystal facets of the seed crystals then dictate the possible final shape through the selective growth and capping of the available facets. The remaining reaction parameters, such as temperature, reagents, and reaction time, will assist in dictating which of the available facets are capped and which are available of further crystal growth. More complex nanostructures require more intricate reaction conditions to achieve the desired final morphology, as a careful balance of reagents and reaction conditions is required to force the formation of the typically uncommon morphology. An example of this is in the synthesis of Ag nanoflowers that required the precise control of both temperature and reagent introduction into the reaction vessel to produce AgNS with the desired complex shape.[53]

Tangential to the formation of complex AgNS is the synthesis of extremely uniform nanostructure. As with most chemical synthesis some variance in the total yield of product is anticipated and is often accounted to inefficiencies in the transformation of one compound to another. In nanostructure synthesis this variance in yield is most often seen in

the final concentration of target nanostructure, as a successful synthesis would result in a high concentration of the target nanostructure, 80%. To improve upon this yield often requires similar stringent reaction conditions to the complex nanostructure synthesis, as the diminished yield are often caused by the slightest discrepancies in either the reagents or reaction conditions. Achieving yields above 95% are often impossible as improving the yield of AgNS in particular has diminishing returns as the target AgNS are almost always thermodynamically unfavoured and as a result the reaction system will always favour the formation of irregular structures that are more thermodynamically favoured.[54]

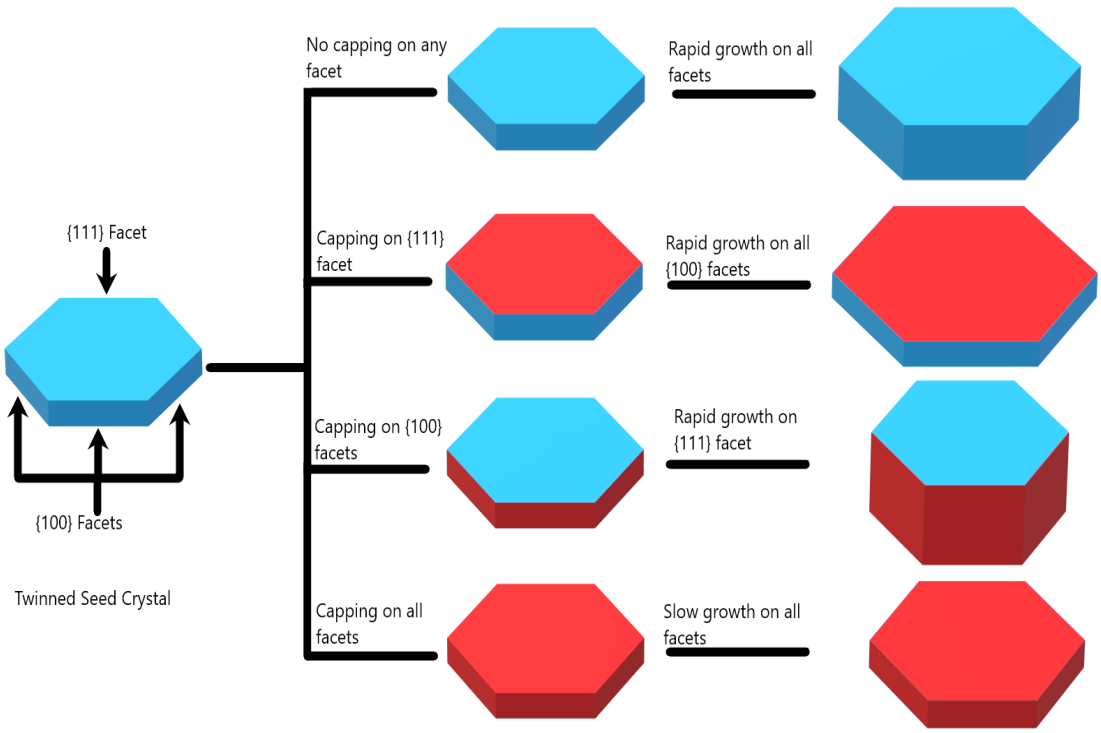

Figure 8: Diagram showing how capping agents affect growth

The general mechanism for AgNS synthesis involves the reduction of a Ag source precursor from Ag(I) to Ag(0) before single and multi-twinned seed Ag(0) crystals begin to grow. Depending on the target structure, an etching agent may be added to remove multi-twinned crystals, etching them back down to Ag(0) atoms, allowing them to reform into single seed crystals. A capping agent is then added that selectively adheres to a specific crystal facet/s on the Ag(0) seed crystals. The capping agent blocks the growth of Ag on the facets being capped, resulting in the accelerated growth of Ag on the uncapped crystal facets. Additional reagents are often used in the synthesis of more com-

plex structures to help with improving the uniformity of structures being produced. The exact methods of synthesis adapted from literature used to produce the AgNS will be discussed in more detail in later sections.

1.4.1 Polyol Reduction

For the synthesis of nanocubes and nanowires a method was sourced from a paper on the synthesis of silver nanocubes using a polyol reduction.[55] This method involves the reduction of silver trifluoroacetate using either ethylene glycol (EG) or diethylene glycol (DEG) as the reducing agent and solvent, polyvinylpyrrolidone (PVP) as the capping agent, hydrochloric acid (HCl) as the etching agent and sodium hydrosulfide (NaHS) as an additional reagent required to produce a higher yield of nanocubes. A systemic problem that plagues many polyol methods is the unexpected impurities contained within commercial reagents, a prime example of this being EG, a solvent/reducing agent that is often contaminated with Fe(II) or Fe(III) stemming from commercial production contamination.[52] Both Fe(II) and Fe(III) influence the oxidative etching of the reaction by interacting with O_2 in the air, which negatively impacts the reproducibility and scalability of the reaction.[56] Variants of the polyol reaction have been extensively researched for the development of uniform nanocubes over varies size ranges.[57]

To optimize the production of nanocubes, independent studies have focused on the impact of each of the reactants that are used in the formation of nanocubes. The studies of interest for this work focus on the solvent and reducing agent, often the same compound, the impact of capping agent and the influence of Cl^-. Each of these reagents were found to greatly impact the formation and reproducibility of nanocubes. The impact of Cl^- on the formation of nanocubes has been recently investigated, with the results of the study finding that the formation of Ag nanocubes can be controlled through the slow release of Cl^- during synthesis, as Cl^- actively adsorbs to, and stabilizes, the [100] facet. As Cl^- favours adsorption onto the [100] facet, it can be used to dictate the shape of the nanocrystal as it forms. This theory has been backed up with ab initio thermodynamic calculations that were consistent with the experimental results, which showed that as the concentration of Cl^- increased, the shape of Ag nanocrystals went from truncated octahedra to nanocubes. [58] Upon the adsorption of Cl^- to the unsaturated Ag [100] facet, the surface

energies of the [100] and [111] facets are reversed so that $\gamma[100] < \gamma[111]$, resulting in the nanocubes becoming the thermodynamically favoured product.[59] The initial interaction between Ag^+ and Cl^- is complex, with the two ions forming AgCl nanocubes which quickly decompose to form a favourable Cl^- chemical potential for the growth of reduced Ag(0) nanocubes. These nanocubes were shown to be independent of the solid Cl^- source assuming the release of Cl^- into the system was sufficient to maintain the favourable Cl^- chemical potential for reduced Ag cube formation.[54]

A pivotal step in the synthesis of AgNS is the initial production of the seed particles required for producing many AgNS. These seed particles can be single, twinned or multiply twinned crystals, and greatly impact the final morphology of the AgNS being produced. The process of using these seed particles during synthesis will be discussed in more detail in a later section. The growth of a seed crystal is determined by the surface free energies of its facets when under thermal equilibrium. In the case of face centred cubic (fcc), metal nanocrystals are often a five-fold multi-twinned structure, where the surface of the crystal is made up of [111] facets that have the lowest-energy of all available facets.[60] But, as most complex crystal growth is not occurring close to thermal equilibrium, the final shape of the crystal cannot be solely determined through the minimisation of surface energy and is instead affected by the growth rate of each respective crystal facet, meaning that the kinetics of the crystal growth need to be taken into consideration. The growth of kinetically stable crystals with morphologies containing multiple facets with differing surface energies have been successfully synthesised through the addition of habit modifying agents into the system during synthesis.[61] One of these habit modifying agents is PVP, which has been shown to have a strong interaction with the surface of the metal nanostructures through coordination between the oxygen and nitrogen atoms of the pyrrolidone ring.[62] PVP has been found to strongly favour the [100] facet of the Ag crystal, leading to an increase in growth on the [111] facet, causing anisotropic growth of the crystal.[48] As the [111] facets have the lowest surface energy, the addition of Ag atoms onto these facets is considerably easier compared to higher surface energy facets or those "capped" with PVP.

It is common in polyol synthesis for the reducing agents to also act as the solvent for the

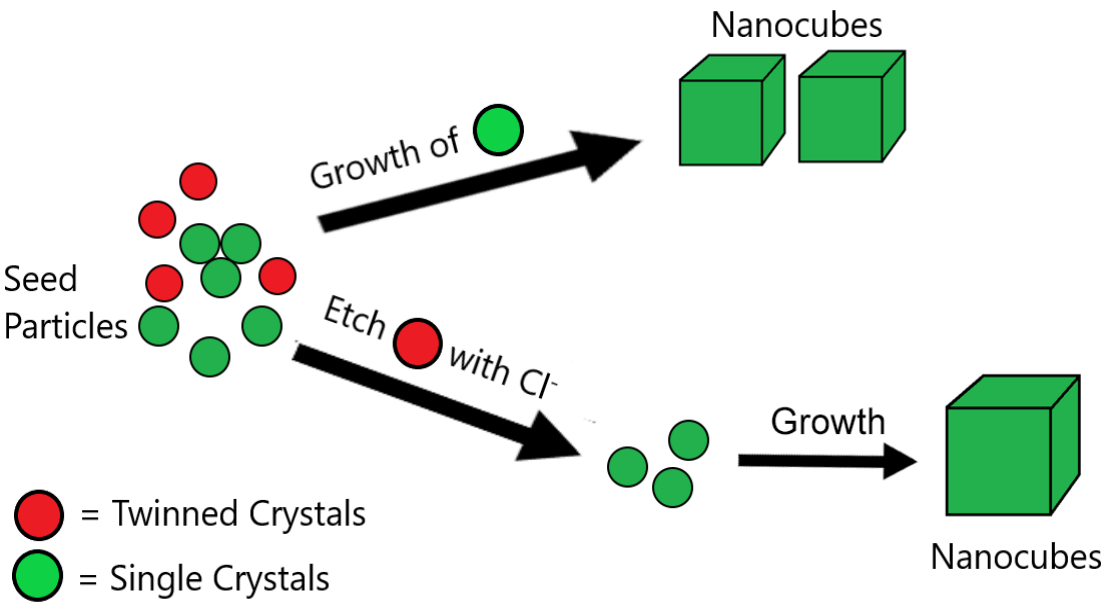

Figure 9: Diagram of the growth process of nanocubes, showing the etching pathways of both single and twinned crystals

reaction as they are often required in large quantities. The reaction kinetics can be manipulated through increasing the length of the hydrocarbon chain of the polyol solvent being used. A direct connection has been made between the growth rate of AgNS and the length of hydrocarbon chain of the polyol solvent, with observations being made on the quality of the initial growth of seed particles when the polyol solvent is changed from EG to tetraethylene glycol (TTEG).[35] As the length of the hydrocarbon chain increased, the reducing power of the compound decreased leading to the formation of Ag seed particles with a broader size distribution compared to when EG was used. [57] In conjunction with this lowered reducing power, the time required to form Ag seed particles increases, resulting in the formation of twinned seed particles as a means of reducing the total surface free energy.[63](Marks, 1994) In the case of nanocubes, single crystal nanocubes were produced using both EG and DEG as the reducing agents under their respective ideal reaction conditions, but for longer chain polyol compounds, TEG and TTEG, nanocube production of the same level of reproducibility and purity could not be achieved. When comparing the results of the shorter chain polyol compounds, there has been separate research into using both in the synthesis of nanocubes and other AgNS, with both achieving similar results. [35, 55] Considering the chemical differences between EG and DEG there is an expected difference in the reducing power between them that appears to be experimentally manageable, considering the depth of literature using both compounds

in nanocube synthesis.

The reducing agent has a secondary effect on the reaction by impacting the nucleation and growth of Ag atoms during the production of seed particles. To force the production of uniform seed particles, the concentration of free Ag atoms formed from the reduction of the Ag salt precursor should increase steadily over the reaction time. Aggregation of Ag atom clusters will begin to form via homogeneous nucleation once the reaction mixture has become supersaturated with free Ag atoms. These clusters will then begin to rapidly grow and cause the concentration of free Ag atoms to decrease below the level of supersaturation. So long as the concentration of free Ag atoms remains below the level of supersaturation, no additional nucleation will occur and the remaining free Ag atoms in solution will be used in the growth of pre-existing clusters. If the concentration of free Ag atoms exceeds the level of supersaturation, then additional nucleation will occur and result in the formation of AgNS at different growth rates compared to clusters formed in the initial stages of the reaction. The choice of reducing agent will greatly impact the concentration of free Ag atoms available in the reaction mixture, as shorter chain polyol compounds (EG) will reduce the Ag salt faster than a longer chain polyol, resulting in the reaction mixture reaching Ag atom supersaturation faster and cause the formation of Ag clusters faster. This will impact the final structure of the AgNS formed as rapid growth of clusters is essential for homogeneous nucleation, and cluster growth over an extended period will result in heterogeneous nucleation and the formation of multi-twinned seed particles.[64]

As the product of the polyol synthesis is heavily dependent on the initial formation of seed particles, forcing the formation of the desirable seed particle is critical to a successful synthesis. For nanocube synthesis, selective oxidative etching agents were added to dissolve twinned and multi-twinned seed particles and promote the formation of single crystal seed particles. Cl^- ions acted alongside O_2 as the selective oxidative etching agents, provided by HCl and the air.[55] The Cl^- ions selectively bond to the twinned crystal seed particles, selectively etching them, before the etched particles are reduced by the reducing agent, EG.[55] This allows for them to reform into single crystal seed particles or adhering to already nucleated single crystal seed particles depending on if the concen-

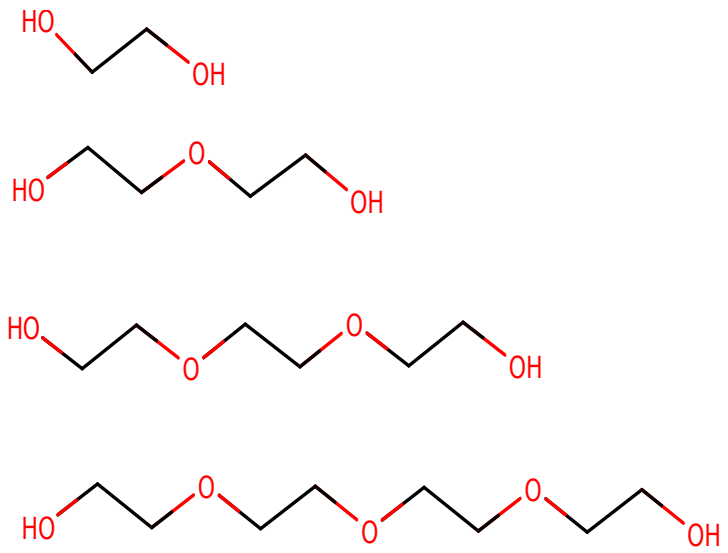

Figure 10: Chemical structure of different polyol compounds often used in polyol synthesis. From top to bottom: Ethylene glycol, Diethylene glycol, Triethylene glycol and Tetraethylene glycol

tration of Ag(0) atoms in solution is below the point of supersaturation.

The polyol reaction is commonly used for the synthesis of nanocubes and nanowires, both of which have been researched extensively.[65] The key difference between the synthesis of nanocubes and nanowires resides in the initial growth of seed particles, with nanocubes relying on single nanocrystals as seed particles and nanowires requiring twinned and multi-twinned nanocrystals.[48] The growth of these seed particles can be manipulated through the introduction rate of the Ag precursor and the capping agent into the reaction vessel. For single crystal formation the introduction of Ag salt needs to occur rapidly to ensure homogeneous nucleation occurs, whereas for twinned and multi-twinned crystals, the rate at which the Ag salt is introduced is delayed, causing heterogeneous nucleation of Ag clusters. These twinned crystals are capped with both [100] and [111] facets that are both available for growth. In combination with this delay, the simultaneous introduction of the capping agent with the Ag salt causes the immediate capping of the [100] facet and insuring growth occurs predominately at the [111] facet. Conversely, most nanocube synthesis involves the addition of the capping agent before the Ag salt, and as single crystals are capped by [100] facets, PVP caps all available facets, resulting in a uniform, slow growth on all facets of the single crystal simultaneously.

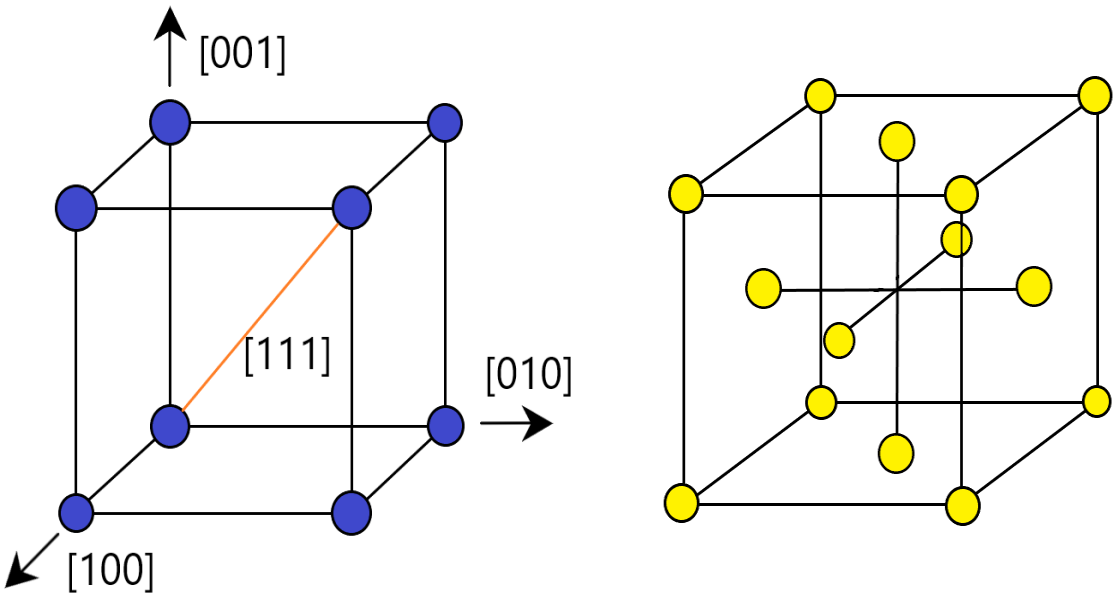

Figure 11: Crystal facet diagrams showing the different facets (Left) and atom packing for a face-centred cubic crystal (Right)

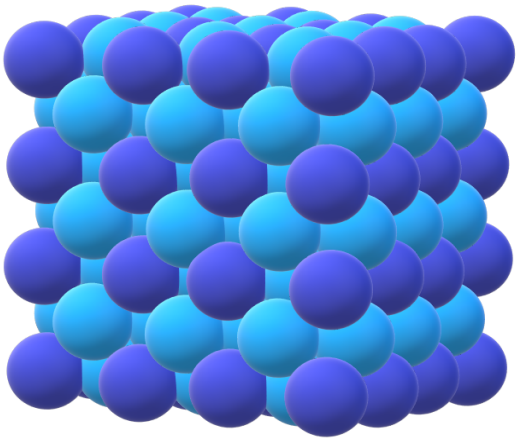

Figure 12: Space filling diagram of a face-centred cubic crystal structure

1.4.1.1 Ratio of Capping Agent to Silver

An important consideration when producing controlled AgNS is the ratio of capping agent to Ag salt precursor. As discussed earlier the rate at which free Ag atoms are released into the initial reaction mixture is dictated by the strength of the reducing agent and will cause the formation of either single or twinned nanocrystals that go on to act as seed particles. Depending on which type of crystal are present, single or twinned, will greatly impact the final shape of the AgNS, as different crystal facets will be available for capping and for growth.[66] The most common capping agent is polyvinylpyrrolidone (PVP)(Figure 13a), that favourably caps the [100] facet of the Ag crystals, leading to rapid growth of the [111] facet as it has the lowest surface energy. Crystal growth will still occur on the [100] facet

but it will be considerably slower compared to the [111] facet. An equimolar solution of PVP and Ag salt is not sufficient to cause a homogeneous product, as there will be insufficient PVP surface coverage on the [100] Ag crystal facet to effectively force the formation of a specific AgNS type. For consistent AgNS growth, the ratio of PVP to Ag atoms needs to be in favour of PVP, with a ratio of 2:1 for cube formation and a ratio of up to 8:1 for nanowires. This ratio needs to be carefully controlled as a lower ratio will lead to growth occurring on all available facets as there is insufficient PVP coverage, leading to irregular nanocrystal formation.[48] If the ratio is too high in favour of PVP then surface coverage will extend to all available facets and will not be limited to just the [100] facet which will also cause the formation of irregular nanocrystals.

1.4.2 Citrate Reduction

The citrate reactions were exclusively targeted towards nanoplate synthesis, with the capping agent, trisodium citrate (TSC)(Figure 13b), selectively binding to the [111] facet of the Ag seed particles. Much like the polyol reaction, the citrate reactions require the addition of seed particles to initiate the reaction and force the formation of the target AgNS. Citrate reactions are often performed at room temperature while under aqueous conditions and have been adapted for the synthesis of different AgNS, but for this project they were used for the synthesis of triangular nanoplates. [50] Unlike the polyol reaction, most citrate reactions are two step reactions, where the initial step involves the formation of seed particles in a separate reaction vessel, before either being left to grow in the original reaction mixture or being used as seed particles in a separate reaction vessel. The reduction of the Ag salt, in most cases $AgNO_3$, is achieved through sodium borohydride ($NaBH_4$), producing Ag(0) atoms that undergo nucleation after reaching supersaturation levels. TSC then selectively binds to the [111] facet of the twinned Ag clusters, resulting in growth on the [100] facet, while single crystal seeds are selectively reduced down to Ag(0) atoms via the addition of hydrogen peroxide (H_2O_2). [67] These free Ag(0) atoms either adhere onto already formed twinned clusters or form new clusters if the concentration of free Ag atoms is above the level of supersaturation. This process of growth and selective oxidative etching is repeated until the majority of Ag atoms are formed into twinned seed crystals and the supply of free Ag(0) atoms has been depleted. It has been theorised that the criti-

cal reagent in this synthesis is H_2O_2, as it promotes the nucleation of nanoplates through the removal of less stable single crystals and when used in turn with TSC the preferential binding to the [111] facet further promotes the formation of nanoplates by stabilizing the twinned seed particles. The preparation of larger triangular nanoplates consisted of producing a growth solution made of acetonitrile, TSC, ascorbic acid and $AgNO_3$, before the reaction is initiated through the addition of a solution of seed particles. Acetonitrile acts as a coordinating agent with the Ag(I) atoms from $AgNO_3$, leading to the suppression of any self-nucleation events that may have occurred during the growth of seed particles into larger nanoplates. TSC acts as a capping agent that was effective in the selective growth of nanoplates as well as acting in the suppression of other morphologies, leading to the formation of nanoplates with high purity.[68] Ascorbic acid is used to reduce the Ag(I) ions from $AgNO_3$ to Ag(0) which were then used to grow the nanoplates. The control of all these different aspects leads this reaction to be scalable through the manipulation of seed particle volume. The reaction kinetics for the growth of nanoplates needed to be tightly monitored to maintain a slow reaction rate. This is achieved through careful control of the reagent concentration, specifically the reducing agent, to keep them below a critical value, and by keeping the reaction temperature at 5°C. Outside of these reaction conditions the product of the reaction quickly transitions from nanoplates to nanoflower type nanostructures, as the accelerated reaction rate leads to uneven deposition of Ag(0) atoms onto the seed particles.[69] The selective binding of TSC on the [111] facet of the nanoplate is sufficient to force the formation of platelike structures. Thus the growth on the [111] facets is minimal as the binding of an organic compound on an inorganic crystal facet cannot completely block crystal growth on the facet. As a result of this, the nanoplates produced are often thin (approximately 7 nm) for a nanoplate with an edge length of 150 nm. [50]

1.4.3 Aqueous Reduction

The polyol reaction suffers from many common drawbacks, primarily its hypersensitivity to chemical impurities, H_2O content and reliance on specific amounts of O_2, which makes the synthesis difficult to replicate. [70] There has therefore been a search to find a method of nanocube synthesis outside of the standard polyol-based reactions. Polyol

reaction nanocubes can often become rounded at the corners and edges, which has been equated to the high reaction temperature and high surface energy, leading to high diffusivity of Ag atoms, high oxidative etching at corners and edges, and inefficient capping of the [100] facets by PVP. [52] Several aqueous nanocube methods have been developed to overcome the drawbacks of the polyol nanocube synthesis. The largest changes made were the removal of the polyol solvent and replacing it with a reducing agent and using H_2O as the solvent for the reaction. A separate reducing agent is required, as H_2O is unable to reduce the Ag(I) to Ag(0). The next adaptation was the replacement of PVP with Cl^- as the capping agent. Lastly, the reaction temperature was lowered to 60°C, as conducting an aqueous reaction at hydrothermal temperatures introduces challenges in monitoring the growth of the Ag seed crystals and AgNS being produced. The growth mechanism of the Ag seed particles produced initially in the aqueous nanocubes synthesis involves the formation of AgCl octahedra seed particles after the addition of the Ag salt into the reaction mixture. Alongside these octahedra are Ag(0) atoms which are the product of Ag(I) ions being reduced by the reducing agent. These AgCl octahedra are slowly reduced over the course of the reaction, while the Ag(0) atoms begin to form large clusters by adhering to one another. The dissolved AgCl octahedra then act as a slow release source of Ag(0) atoms that can adhere to the clusters and assist in forming the nanocubes.[59] Much like the polyol reaction of nanocubes, an additional compound was added to selectively dissolve any twinned seeds that may form during the initial stages of the reaction. In this case $FeCl_3$ was introduced and acted as an oxidative etchant to remove any

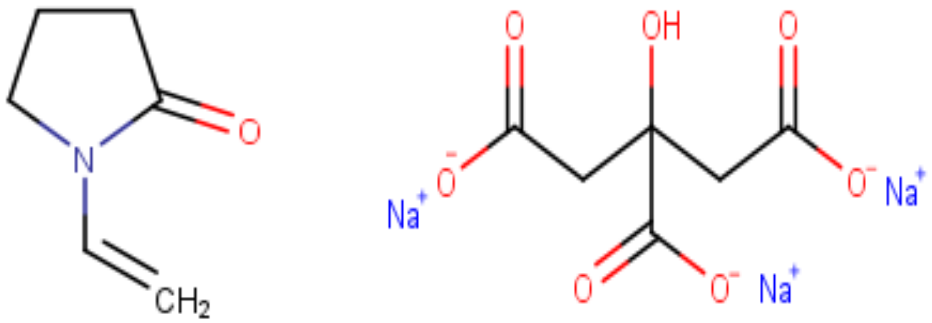

(a) **(b)**

Figure 13: Chemical structure of vinylpyrrolidone (a) and trisodium citrate (b)

twinned crystals, dissolving them back to Ag(0) atoms, which allowed for the growth of more single crystal seeds. The selective capping of the [100] facets in the aqueous method was achieved through the release of Cl^- ions from the CTAC added into the reaction mixture before the Ag salt. The concentration of Cl^- is lower than the concentration of Ag^+, leading to the majority of Ag^+ will remain in the AgCl crystal form, enabling them to be reduced by the reducing agent. Much like the polyol reaction, the ratio of capping agent to silver atoms is critical in the formation of the desired product. For this method the ratio of Cl^-: Ag^+ needed to be well below 1:1, otherwise the product of the reaction would be large, irregular nanoparticles. [50]

1.5 Summary

The three AgNS synthesis techniques have been discussed, including the reaction mechanisms, reaction conditions and the AgNS produced using these techniques (Table 1, 2). The general reaction mechanism for the growth of controlled AgNS is similar in all three of the techniques, with the Ag salt being reduced from Ag(I) to Ag(0) using a reducing agent before the growth of Ag(0) clusters. This growth is controlled through capping and coordinating agents to force growth to occur on specific crystal facets. Ag(0) clusters with unfavourable facets were oxidatively etched back down to Ag(0) atoms to enable the reformation of favourable Ag(0) clusters or deposit on the existing Ag(0) clusters. There are obviously other experimental methods that have been used in the synthesis of AgNS but, as the results presented in the following chapters will show, these three techniques were the most consistent at producing the desired AgNS with the greatest reproducibility.

Table 1: Summary of how different reaction parameters effect the synthesis of AgNS

	Effect on Synthesis
Seeding crystal	Different seeding crystals will be capped by different crystal facets, resulting in different facets being available for growth
Temperature	The temperature directly effects the crystal growth rate, with faster crystal growth leading to more irregular crystals being produced.
Reaction Time	Longer reaction time will lead to more uniformity in the nanostructures produced as more of the undesirable seeding crystals will be transformed into desirable products.
Contamination	Contamination with metal ions leads to uncontrolled etching and side reactions with other reactants
Capping Agent	Capping agents adhere to specific crystal facets and passivate them to minimise growth from these facets.
Reducing Agent	The reducing agent reduces the Ag(I) ions supplied by the Ag salt to Ag(0) atoms which then go on to become seeding crystals
Capping agent:Seed crystal Ratio	Excessive amounts of capping agent will lead to capping on all available crystal facets, leading to poor growth on every facet. Insufficient amounts of lead to incomplete capping on the target facet, which will not completely impede growth.

Table 2: Summary of how the different reaction parameters impact AgNS growth

Summary of Reaction Parameters		
	Nanocubes/Nanowires	Nanoplates
Seeding crystal	Nanocubes require single seed crystals that are capped with [100] facets. Single seed growth promoted with NaHS. Nanowires require twinned seed crystals that are capped with [100] facets.	Nanoplates require twinned seed crystals that are capped with [100] and [111] facets.
Temperature	Require high temperatures to imitate the breakdown of Ag salt into Ag(0).	Performed in an aqueous environment so can be performed at low temperatures to slow reaction kinetics and slow crystal growth.
Reaction Time	Average reaction time of 1 hour, can be altered to produce AgNS of different sizes.	Slower reaction time of 30 minutes, can be altered to produce AgNS of different sizes.
Contamination	Polyol reagents commonly contaminated with Fe ions that cause uncontrolled etching of both seed crystals and AgNS.	Citrate reactions can have trace metal contaminants stemming from the quality of reagent used
Capping Agent	PVP to selectively cap the [100] facet.	Cl^- provided by CTAC that selective cap the [100] and TSC selectively capped the [111] facet.
Reducing Agent	Cl^- ions provided by HCl.	Ascorbic acid
Capping agent:Seed crystal Ratio	Ideal ratio of PVP to Ag is 2:1 to achieve sufficient capping for nanocubes. 0.5:1 ratio for nanowires.	Need to achieve sufficient capping on both the [111] and [100] facets to achieve the platelike structure.

1.5.1 Thesis Outline

1.5.1.1 Chapter 3

This chapter introduces and discusses the different methods and characterisation techniques used to produce and characterize the nanostructures used in this project. The exact scientific methodology used to produce the nanocubes, nanowires and nanoplates will be stated with sufficient detail to enable reproducibility in a different lab environment. Alongside these, the analytical methods and equipment used in the characterization of the nanostructures will be stated and discussed to show the range of techniques used to thoroughly characterise the structures along with the methods used in the collec-

tion of Raman, SERS, and single molecule SERS data.

1.5.1.2 Chapter 4

This chapter discusses the theories behind the Raman experiments undertaken, including SERS, single molecule SERS, microfluidic Raman and plasmonic optical trapping single molecule SERS, as well as a discussion on the different statistical analysis techniques utilized during the project to investigate the possibility of clustering occurring inside the SERS data. Each of these SERS experiments and analysis techniques are discussed in detail and with context to the project.

1.5.1.3 Chapters 5, 6, 7

These chapters discuss the characterisation, synthesis difficulties and results of using the three nanostructures as SERS substrates in the experiments discussed in Chapter 2. Each chapter begins with discussing the synthesis process for each nanostructure including any difficulties faced, the quality of structures produced, and possible improvements that could be made. The results of the characterisation techniques were discussed which included breaking down multiple TEM images and UV-vis spectra and relating them to the overall quality of the structures produced. The SERS results using the nanostructures were then broken-down, beginning with discussing the initial and high intensity SERS spectra, which included discussing peak position, intensity, and other trends. The statistical analysis techniques were then discussed beginning with the results of the PCA analysis. This included commenting on the appearance of the Scree, Loadings and Score's plots, making assumptions on trends that may be present inside the data and relating the PCA results to the observations made about the initial and high intensity spectra. The additional clustering analysis techniques were discussed last, with plots of each technique being displayed and discussed starting with the Euclidean distance map followed by the self-organising map. The results of both these techniques were compared with each other and the PCA results to develop a greater understanding of trends inside the data before a summary was made of the trends observed over the results and a conclusion was made as to which of the prevailing theories best fits the data. Chapter 3 discusses nanocubes, while nanowires and nanoplates are discussed in chapters 4 and 5 respectively.

1.5.1.4 Chapter 8

This chapter discusses the additional SERS experiments undertaken, including contaminant peak experiments and extremely low concentration SERS experiments, along with a comparison of the three nanostructures and a discussion as to which theory best describes the trends in the data. The contamination peak experiments consisted of discussing the pure PVP and TSC Raman spectra with SERS spectra collected for each of the different nanostructures. These comparisons also included comparing the chemical structure of PVP and TSC with the structures of the two dye molecules. The aim of this experiment was to identify the cause of the outlier peaks present in all SERS data, with the hypothesis being that the two nanostructure capping agents are responsible for these peaks. The extremely low concentration data discussed in this chapter was collected using nanocubes as the substrate for both dye molecules with the aim of collecting SERS with the highest probability of there being a single dye molecule adhered to a single nanostructure. The low concentration range used in these experiments guaranteed that any SERS collected was single molecule SERS, and therefore can be used in investigating the hypothesis that dye molecules on different nanostructure regions will result in different SERS signal being generated. The results of the SERS experiments were tabulated, and the rate of SERS spectra occurrence was calculated for each nanostructure. Similar calculations were also made for the high intensity SERS spectra before both rates were compared and conclusions were made. Finally, in this chapter each of the nanostructures were compared and the results of the project were summarised.

CHAPTER 2

Experimental Methods and Characterisation

2.1 Reaction Parameters

All reagents were sourced from Sigma-Aldrich (St Louis, Missouri, US) and were not purified further. All glassware was piranha cleaned using a 3:1 mixture of concentrated sulfuric acid (H_2SO_4) and hydrogen peroxide (H_2O_2) before being thoroughly rinsed with deionized water and dried in a 105°C oven overnight.

2.2 Synthesis of Nanocubes

The method of synthesis for nanocubes was modified from a paper by Zhang et al [55]. All reagents were prepared fresh before each synthesis. A clean, dry 100 mL glass round bottom flask was placed in an oil bath before 5 mL of anhydrous EG was added and heated to 150°C while under stirring. The flask was capped during the entire synthesis process excluding during the addition of reagents. Once the flask reached 150°C it was left for 30 minutes to ensure the EG reached the required temperature. After 30 minutes 60 μL of 3 mM NaHS was added to the flask via autopipette. Two minutes later 0.5 mL of 6 mM HCl and 1.25 mL of 38 mg/mL PVP (MW = 55000) was added. Two minutes after this 0.4 mL of 282 mM CF_3COOAg was added before the flask was capped and heated with stirring for 1 hour. After the reaction was completed the flask was removed from the heat and cooled in an ice bath before being washed using the protocol discussed in section 3.6.1.

2.3 Synthesis of Nanowires

The method of synthesis for nanowires was a modification of the nanocube synthesis discussed in section 3.2. Excluding a change in reagent concentration, the methodology was identical to the nanocube synthesis. The reagents changed were HCl and PVP that were changed from 6 mM to 3 mM and 38 mg/mL to 10 mg/mL respectively.

2.4 Synthesis of Nanoplates

The method of synthesis for nanoplates was modified from a paper by Liu et al [50]. This method involves the synthesis of smaller seed nanoparticles that are then used in the synthesis of the larger triangular nanoplates. The synthesis of seed molecules was as follows: A mixture of 12 mL of 0.0075 M TSC, 200 µL of 0.1 M $AgNO_3$ and 480 µL of 30 wt% H_2O_2 were added to a 250 mL clean, dry glass round bottom flask before 200 mL of deionized water was added. A magnetic stir bar was then added before the mixture was stirred until the reagents were fully dissolved. Under vigorous stirring 1.2 mL of 0.1 M $NaBH_4$ was added quickly. The reaction mixture then undertook several colour changes as the silver nanoparticles began to grow, with the original reaction mixture being colourless before quickly changing to yellow, orange, red then dark purple to blue. The mixture was left stirring for 10 minutes until the solution reached a dark blue colour. This solution acted as the stock solution for the synthesis of nanoplates and a portion of the stock solution was centrifuged down to concentrate the nanoplate solution to one-fifth the original volume. The synthesis of nanoplates was as follows: 10 mL of deionized water was added to a clean, dry 100 mL glass round bottom flask before 5 mL of acetonitrile, 150 µL of 0.1 M ascorbic acid and 100 µL of 0.075 M TSC were added. The reaction mixture was cooled to 5°C using an ice bath and a magnetic stir bar was added to stir the solution. Under vigorous stirring 12 mL of the concentration seed solution was added via autopipette followed by 120 µL of 0.1 M $AgNO_3$ to begin to nanoplate growth process. The reaction mixture was left to react under stirring at 5°C for 30 minutes. After 30 minutes the reaction mixture was taken from the ice bath and washed using the washing protocol described in Section 3.6.1.

2.5 Preparation of Silica Micro-spheres Decorated with AgNS

1 μm and 1.85 μm diameter silica spheres were sourced from Sigma-Aldrich (St Louis, Missouri, US) before being functionalized with an amino silane ligand using the method of Najafi et al. [71] Silica spheres (0.5 g) were refluxed in 25 mL of toluene containing 2.5 mmol of 3-aminopropyltriethoxysilane for 2 hours, the solid product was filtered and washed with toluene and ethanol before being transferred to a watch glass and dried in a 100°C oven until completely dry. The functionalized silica spheres were then decorated with either the previously prepared nanocubes, nanowires or nanoplates by adding 0.06 g of functionalized silica spheres to 0.4 mL of each of the nanostructures before diluting with 0.5 mL of deionized H_2O. This mixture was then sonicated for 5 minutes before being left for 24 hours to let the nanostructures have time to adhere to the silica surface.

2.6 Instruments and Equipment

Transmission electron microscopy images were collected using a FEI Tecnai G2 Biotwin Transmission Electron Microscope with tomography unit provided by the Manawatu Microscopy and Imaging Centre. UV-visible spectra were collected using a benchtop Shimadzu UV-1800 UV-vis spectrograph provided by the School of Fundamental Sciences. Raman spectra were recorded under ambient conditions with a custom-built Raman microscope, consisting of a 532 nm excitation laser (Laser Quantum Torus 532) focused onto the SERS sample via a N. A.= 0.65 (40 x magnification) microscope objective. Back-scattered Raman and Rayleigh scattered light was collected by the same objective and the Rayleigh component was rejected by a 532 nm Raman edge filter (Iridian Spectral Technologies) and focused onto the entrance slit of a Teledyne (Princeton) Instruments Isoplane81 (FERGIE) spectrograph. The laser power focused on the sample was between 1 – 10 mW depending on the type of experiment being run. Spectral data were acquired using LightField 6.1 software. No background removal was applied during data collection. The detector exposure time was 0.1 seconds, and 600 exposures were captured and stored separately prior to data analysis.

All centrifugation steps were performed using a Sigma 1-14 Benchtop Centrifuge provided by the Massey University School of Fundamental Sciences.

2.6.1 Centrifugation and Washing Protocol

Each of the nanostructures produced followed a protocol for separating the structures from the reaction mixture, removing any excess unreacted reagents, and concentrating the quantity of nanostructures in the final solution. The washing protocol was as follows: The reaction mixture was transferred from the reaction vessel to 2 mL Eppendorf centrifuge tubes before being spun at 16162 xg for 20 minutes or until sufficient pelleting occurred. The supernatant fluid was then removed from each of the tubes before the pellet was resuspended in reagent grade acetone and spun at 16162 xg for 5 minutes. This process was repeated up to three times using deionized H_2O instead of acetone before the final pellets were collected and suspended in deionized H_2O inside a suitable container for long term storage.

2.6.2 Transmission Electron Microscopy

Sample preparation for the collection of TEM images followed a simple protocol where a droplet of sample was placed on a piece of parafilm before a Formvar coated copper grid was placed on the droplet and left for 4-5 minutes to provide enough time for the nanostructures to adhere to the Formvar surface. The copper grid was then dried before being used in TEM imaging.

2.6.3 UV-vis Spectroscopy

When collecting UV-vis spectra, a 40 µL droplet of washed nanostructure solution was placed in a glass cuvette before being diluted with 2 mL of deionized H_2O.

2.6.4 Preparation of SERS Samples

Each of the samples used in the collection of SERS data were prepared using the following methodology. A 2:1 mixture by volume of freshly prepared, washed and sonicated nanostructures and dye molecules solution (concentration ranging between $1x10^{-9}$ M - $1x10^{-16}$ M) were mixed in a glass vial before being mixed using a sonication bath until thoroughly combined. To ensure the dye molecules adhere to the surface of the nanostructures, the mixture was then left in a dark place for 24 hours before being used in analysis. Without this aging process, most dye molecules did not have adequate time to adhere

to the surface of the AgNS, leading to poor SERS spectra in comparison to samples where the aging process was utilized. This observation was made after trial and error of trying to optimise the collection of SERS spectra. This ratio of dye molecules to nanostructure appeared to result in sufficient surface coverage and lead to most of the dye molecules adhering to the AgNS rather than staying in solution. Before the collection of SERS spectra, the samples were sonicated in a sonication bath for 10 s to remove any possible aggregation that may have occurred. This was especially important for the nanowire samples, as they are most prone to aggregation due to their size. For the collection of conventional SERS spectra, excluding when using the microfluidic chip, a 40 µL droplet of sample was place onto a glass coverslip before the beam of the laser was focused on the middle of the droplet. Despite the higher laser power used no carbonization was observed. This was because the AgNS were able to shift out of the focal volume of the laser as the gradient force they were experiencing didn't have any external constraints to pin the AgNS against. The glass coverslip was replaced with each new sample to remove any possibility of contamination between samples. SERS samples produced using the functionalized silica spheres decorated with each of the different nanostructures were prepared by mixing 0.2 mL of the decorated silica spheres with 0.1 mL of $1x10^{-9}$ M R6G and then leaving the mixture for 24 hours to achieve sufficient adsorption.

2.6.5 Microfluidic Chip Setup

The microfluidic chip system (Figure 14) consisted of a custom glass chip with three "Y" shaped channels, each containing two input ports and one output ports. Polyether Ether Ketone (PEEK) tubing was then attached to the input ports using a method designed by Rob Ward, with MicroTight Union Assemblies connecting the PEEK tubing to Trajan SGE Microvolume Liquid Chromatography Syringes [72].

When using the microfluidic chip, two 100 µL glass syringes with silicon tipped plungers were filled, one with deionized water and the other with SERS sample, before being injected into the microfluidic chip using two syringe pumps via the intake ports on the chip. Before data collection the chip was flushed with deionized H_2O several times to ensure the main channel of the chip was clean and clear of any obstructions. To check the channel was clear of any contamination from previous experiments a background spectra of

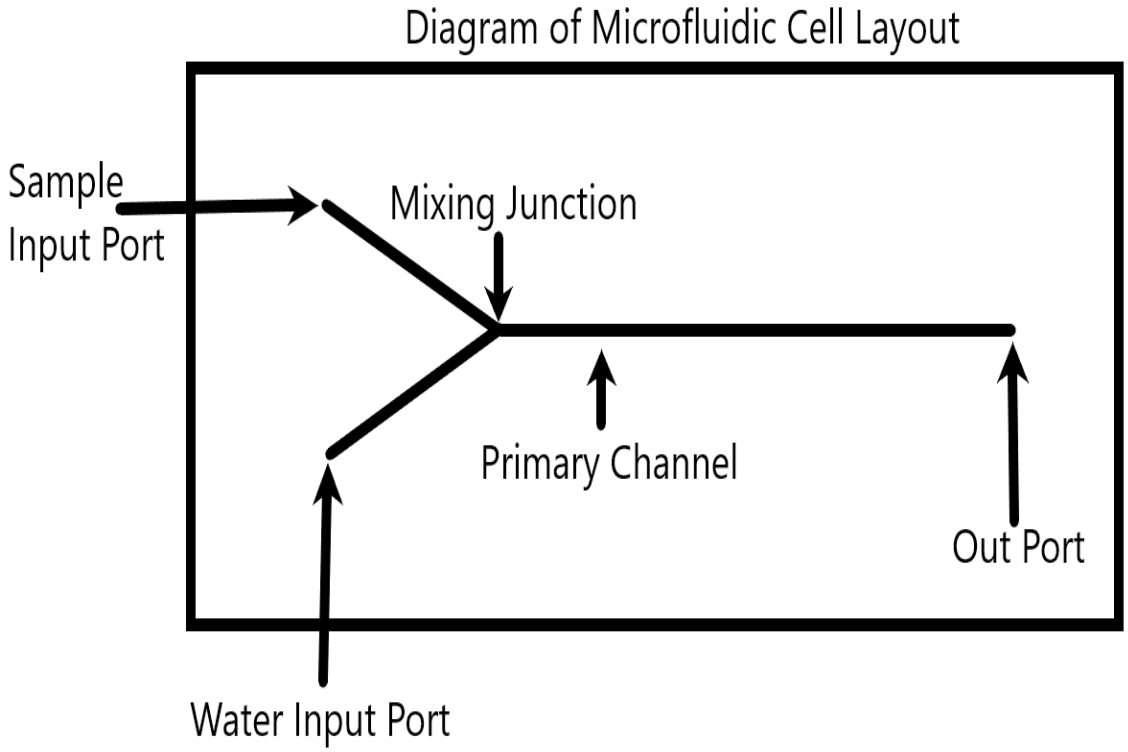

Figure 14: Diagram of the microfluidic chip channel and port layout

the channel was collected after it had been flushed with H_2O. During data collection the flow rate of both the syringes were set at 200 nL/s. The laser power used was 1 mW at 532 nm.

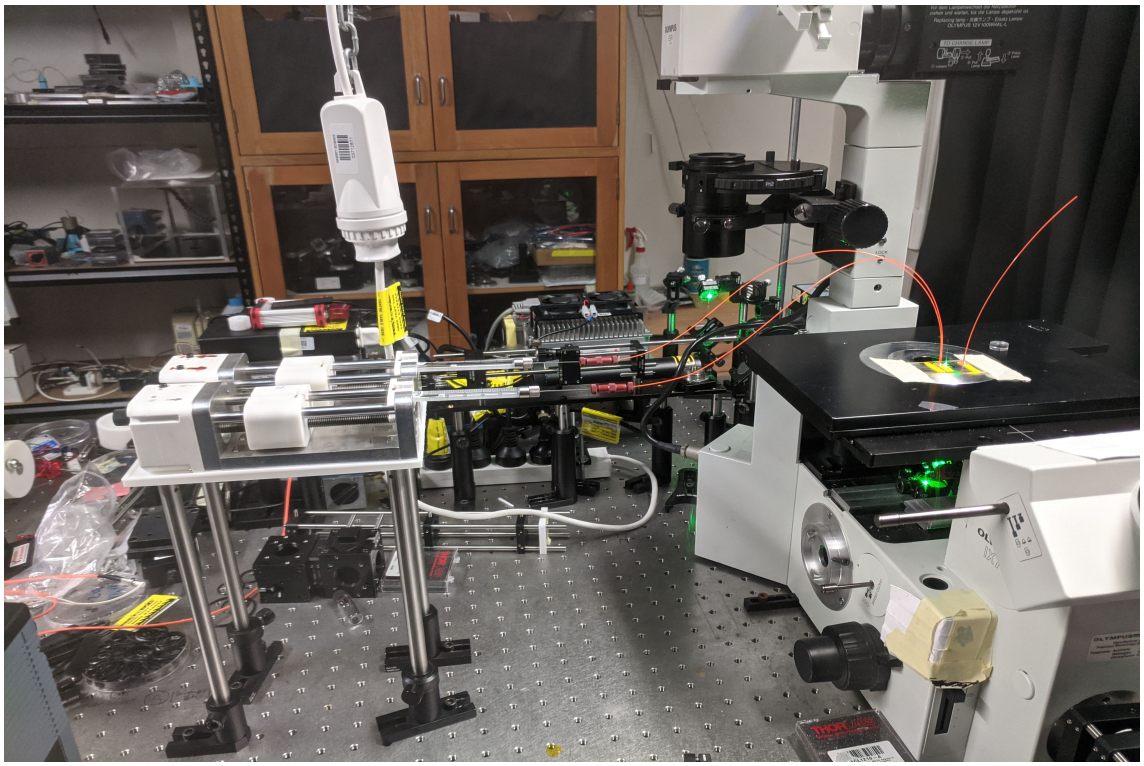

Figure 15: Image of the Microfluidic chip when used in tandem with the confocal Raman setup

2.6.6 Optical Tweezers

The optical tweezers setup utilized was provided by the William's Group (School of Fundamental Science, Massey University) and consisted of a custom-made inverted microscope using a 2 W 1064 nm laser as the trapping laser and a 1 mW 532 nm laser as the probe laser to initiate the Raman signal. The optical trapping samples were prepared by firstly diluting 10 μL of AgNS + dye solution in 10 mL of deionized water. This mixture was shaken before 100 μL of this mixture was placed in the cavity of a single cavity glass coverslip. A second coverslip was placed over the cavity and sealed shut using nail polish. A portion of the 100 μL of sample was trapped inside the cavity of the coverslip and remained inside the cavity for several hours before beginning to degas.

2.7 Statistical Analysis

The basis for all statistical analysis undertaken on the Raman data collected was achieved through code written in Python that was made up of original functions and packages sourced from previous projects. Initially the raw spectral data is brought into the code as individual spectra before being baseline corrected and normalized to minimise variance in the data. Cosmic spikes that may have been collected alongside the Raman data were also removed following this step.

Any spectrum that did not contain a peak over a selected threshold was then removed from the data set and the remaining data was run through a standard Principal Component Analysis (PCA) function. Using the principal components produced from PCA, Scree, Scores and Loadings plots were produced for each of the sets of data. These were critical in building an understanding for what trends are in the data and were used to investigate clustering in data points. Secondarily to PCA, more specialized clustering functions were implemented to investigate possible clustering in the collected data that was theorised to be occurring. These functions included Euclidean distance mapping and self-organizing maps, which are statistical techniques used to find patterns inside data sets based on distance differences between data points. The Euclidean distance and self-organizing maps used the individual spectra as data points and compared them before grouping together spectra that have similarities in peak position and intensity. These

were then plotted as a 2D array of spectra vs spectra while showing the degree of difference/similarity through an intensity subplot.

2.8 Summary

Each of the methods of synthesis used in this project have been stated with sufficient detail to allow them to be reproduced by others. Alongside the discussion of these methods was a detailed discussion of all equipment and analytical techniques used in the characterisation of the nanostructures and the collection of SERS data. To assist in summarising this chapter a table was generated that contained a brief summary of each analytical technique that was implemented during the project (Table 3).

Table 3: List of analytical methods implemented and the information they provide

Technique	What do they measure?
TEM	Physical composition and structure of AgNS
SEM	Physical structure and surface detail of AgNS
UV-vis Spectroscopy	Size and position of the AgNS LSPR peak inside the UV-vis wavelength range.
SERS	A SERS spectrum provides peaks at different wavenumber positions based on the vibrational modes of the dye molecule being investigated.
Scree Plot	Plot of the variance vs principal component that provides detail into how the variance in SERS spectra are being covered by the different PCs.
Loading's Plot	A plot of PC variance against the wavenumber range used in SERS collection that results in the PCs being displayed as a variance spectrum.
Score's Plot	A plot of a PC against another PC that provides insight on how the spectra relate to both PCs and can be used to identify clustering that may be occurring.
Euclidean Distance Maps	A plot of spectra vs spectra that displays the distance value between the spectra using a colour gradient scale bar. This distance value is calculated using Pythagorean theorem for the distance of a right-angled triangles hypotenuse. Two data points act as the ends of the hypotenuse and the distance value is the length of the hypotenuse. The more similar the spectra the lower the distance value.
Self-organizing Maps	A plot made up of nodes that represent groups of spectra that are separated based on how similar they are. The similarity between spectra is determine by comparing each spectra against a set of models that is generated from the total set of spectra. The spectra are then grouped based on how they related to the different models.

CHAPTER 3

Raman Spectroscopy

3.1 Surface-enhanced Raman Scattering

The collection of all SERS data was achieved through the conventional and microfluidic methodology discussed in the Methods and Characterisation Chapter. One of the hypotheses of this project is that the uniformity of these structures should result in the appearance of a finite number of SERS spectra based on the location of the adhered dye molecule. Using nanocubes as an example, where all the capping facets are [100], there is effectively three different regions where a dye molecule can adhere; to a face, an edge, or a corner. Given the impact surface plasmon resonance has on SERS enhancement, there should be a difference in the SERS signal produced if a dye molecule is adhered to a face, edge, or corner as each of these locations contain different surface plasmon resonance environments. Each of the faces will have the same surface energy and will only contain a single surface plasmon. Edges lie at the interface between two faces and as a result will also be the interface between two surface plasmons. This should give rise to greater enhancement compared to a face adhered molecule. Corners should therefore provide the greatest enhancement as they lie at a junction between three faces and therefore three surface plasmons. Following this reasoning there should be a different SERS signal produced if a molecule is adhered to each of these different locations. The number of possible binding sites for dye molecules will be different for each of these regions however, as they will have varying amounts of available surface area. Crystal faces will have the highest number of binding sites, while edges and corners will have substantially less, given their lower surface area. As more binding sites are available for faces it would

be expected that the largest portion of total SERS spectra collected would be generated from face adhered dye molecules. The difficulty in verifying this theory is ensuring the location that the dye molecules adhere to, as thermodynamically all three locations will be favoured for molecule adhesion. As there is no control over the dye molecule adhesion, the resulting SERS signal produced will be an average over all dye molecule locations. Fortunately, this averaging can be removed by lowering the concentration of dye molecules to the single molecule region so only one dye molecule will be adhered to a nanostructure during SERS generation. This interaction between the different regions of nanocubes has been investigated and a difference in intensity was recorded for the different interactions between regions, which correlates to the predictions made during the project.[73]

The orientation of the nanostructure inside the focal volume of the laser may also impact the SERS signal produced during optical trapping as the different locations have stronger interactions with the incident beam depending if the face, edge, or corner is orientated with the polarization and direction of propagation of the laser beam. Statistically there will be more molecules adhered to the crystal faces than the edges and corners as the faces contain a larger surface area to fit more molecules. This is likely not an aspect of any SERS experiment that could be controlled as the gradient force supplied by the laser beam is high enough to force the rapid movement and rotation of the nanostructures as they travel through the focus of the laser. The small size of the nanostructures causes them to be heavily influenced by both Brownian motion caused by thermal fluctuations and gradient forces provided by the laser beam. When using the conventional SERS experimental setup, there was no feasible way to control for this, because as the nanostructures enter the laser focus, they are accelerated and move out of the focus, only remaining inside the focal volume for tenths of a second. The time inside the focal volumes was estimated, assuming a roughly cylindrical focal volume, and it was calculated that a cubic nanostructure with an edge length of 50 nm spent 0.22 s inside the focal volume of the laser (Table 4). These calculations were done using the parameters listed in Tables 5 and 6 and followed Equations 1 and 2.

$$V = \pi r^2 h \tag{1}$$

Table 4: Parameters used in Stokes-Einstein Diffusion calculations

Stokes-Einsteins Diffusion Calculation	
Boltzmann's Constant/K_b $(J.K^{-1})$	1.38E-23
Temperature/T (K)	293.15
Viscosity/ (Nsm^2)	1
Radius of Nanocube (m)	3E-8
Diffusion Coefficient (m^2/s)	7.15E-15
Time in Focal Volume (s)	0.22

Table 5: Parameters used to calculate the number of nanocubes in a sample

Number of Nanocubes in Sample			
Ag Atom Radius (nm)	0.172	TEM Scale Bar (nm)	100
Atom Volume (nm^3)	0.0213	TEM Scale Bar (mm)	15
Nanocube Volume (nm^3)	60	Length of Cube (mm)	9
Ag Atom Packing Coefficient	0.74	Scale Bar:Cube Length Ratio	0.6
Number of Ag atoms per Cube	2083.1	Length of Cube (mm)	60
Moles of Ag (M)	0.282	CF_3COOAg (g/mol)	220.9
Avogadro's Number	6.02E+23	Ag (g/mol)	107.9
Number of Total Atoms	1.7E+23	Ag:CF_3COOAg	0.488
Number of Ag Atoms	8.29E+22		
Volume of Sample (mL)	1		
Cubes per Sample	3.98E+19		

Table 6: Parameters used in laser focal volume calculations

Focal Volume of Laser Calculation	
Spot Size (μm)	10
Spot Size Radius (μm)	5
Height (μm)	60
Focal Volume (μm^3)	1570.75
Focal Volume (m^3)	1.57E-15

$$D = \frac{k_b T}{6\pi\eta r} \tag{2}$$

The time estimation was made using several assumptions. The first assumption was that the nanostructures were cubic and that the laser beam at the focus is roughly cylindrical with a beam height of 20 μm. AgNS form in a face centred cubic formation, with a packing coefficient of 0.74, meaning there is a 26% void volume between Ag atoms as they pack together. The number of Ag atoms was calculated using the number of moles of Ag precursor and the ratio of Ag atoms inside the precursor. The size of the cubic nanostructure was known from the TEM images, so it was possible to calculate how many Ag atoms are required to make up a single cube. As both the total number of Ag atoms and the number

of atoms required to make one nanocube are known it is possible to determine the number of nanocubes present inside a single millilitre of nanocubes. A secondary assumption made during this calculation was that all nanocubes were uniform shape and size, as any difference in either of these physical parameters will change the calculated number of nanocubes present. The focal volume of the laser was estimated using the standard equation for the volume of a cylinder (Equation 1) using the assumptions that it has a height of 20 μm and is a uniform cylinder of light. With a spot size of 10 μm the calculated focal volume of the laser focus is $1.57\text{x}10^{-15}$ m^3. The diffusion rate of the nanocubes in solution was then determined using the Stokes-Einstein diffusion equation (Equation 2) and was found to be $7.15\text{x}10^{-15}$ m^2s^{-1}. With the diffusion rate and the volume of the focus now known it was calculated that a nanocube would spend 0.22 s inside the focus as it diffuses through the solution.

Given the assumptions, this value of 0.22 s can be considered an approximation of the time for a nanocube to spend inside the focus as the beam focus is likely not perfectly cylindrical and the nanocubes contain variance in both their size and shape. This value will also only be relevant for nanocubes, as the nanowires and nanoplates will diffuse at different rates through the solution. Estimating the diffusion coefficients for the nanowires and nanoplates was a more complicated task as there are larger variance in the nanowires and for a non-spherical shape, and it was difficult to determine all the dimensions of the nanoplates. On average the nanowires are several orders of magnitude larger than the nanocubes, meaning that the time they spend inside the focal volume should be considerably longer. The height of the nanoplates is not easily determined, as the TEM was incapable of imaging the structures at a high enough resolution to accurately measure their height. This made determining the volume of the nanoplates difficult, which in turn impeded the ability to accurately estimate their diffusion coefficient. The nanoplates have a cross sectional area of similar size to the nanocubes, but their lower height dimension could greatly impact their diffusion coefficient. The difference in height of the nanocubes and nanoplates is most clearly seen in the TEM images of both structures. When adhered to the surface of the micron-sized silica spheres (Figure 20), the nanocubes protrude out from the surface while the nanoplates lie flat against

the surface. This theory was experimentally observed as all the SERS data collected using the conventional method display short periods of SERS signal, typically over two to three frames. The exposure time for a single frame is 0.1 s, meaning that over two to three frames the nanostructures producing the SERS signal were inside the focal volume between 0.2 s and 0.3 s. Based on this it is likely that the nanostructures are diffusing into the focal volume before being accelerated by the laser beam and escaping the focus. Without a method of trapping the nanostructures inside the focus of the laser, the conventional method of collecting SERS data was deemed unsuitable for the collection of optically trapped SERS data and for determining the impact that the nanostructure's orientation has on the SERS signal it produces.

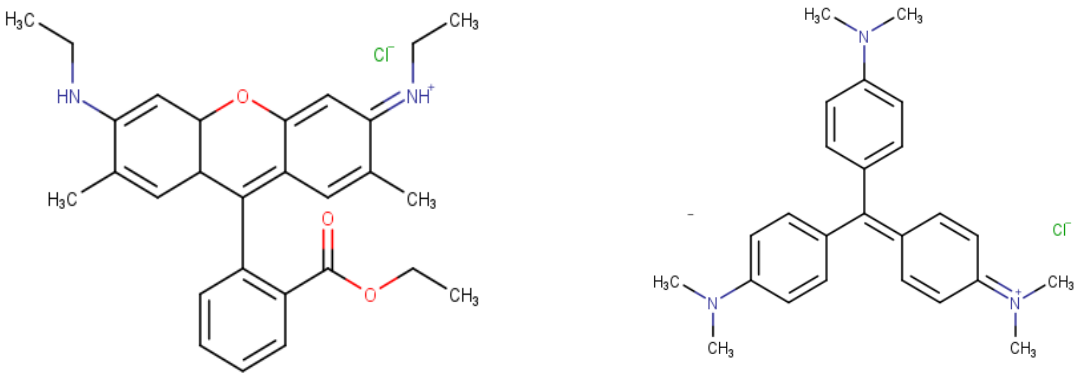

(a) **(b)**

Figure 16: Chemical structure of Rhodamine 6G (a) and Crystal Violet (b)

It is difficult to compare the SERS spectra collected with literature spectra of both Rhodamine 6G and Crystal violet as the literature spectra are collected with a long collection time, and using an amorphous sample, meaning that the literature spectra is often an average Raman spectra. The SERS spectra collected here were collected over a range of concentrations, with a much lower collection time and used a SERS substrate to enhance the Raman signal. This meant that the SERS spectra collected are not average spectra and are instead spectra collected from a small number of molecules or even single molecules, leading to an increase in spectral variance. This variance stems from the position the molecule is adhered to on the SERS substrate, as different conformations will lead to the expression of different vibrational modes and produce a different Raman signal.

3.1.1 Determining dye molecule location based on SERS signal

As the nanostructures are likely tumbling through the focal volume of the laser due to a combination of Brownian motion and buffeting from the gradient force of the laser, it is possible that some of the SERS signal collected was from a nanostructure that had a dye molecule adhered to either a face, edge, or corner. The difficulty comes in distinguishing between these SERS spectra. Fortunately several hundred SERS spectra were collected for each sample, making it possible to use statistical analysis techniques to analyse the SERS data to find evidence of the expected clustering occurring inside the nanostructure. Theoretically there should be a discrete number of clusters corresponding to the number of unique positions a dye molecule could adhere to a given nanostructure. It is also possible that a string of clusters may be present, as it is unlikely for a single dye molecule to be present when a SERS signal is collected, outside of a single molecule concentration. Without performing the experiment at a single molecule concentration range while simultaneously trapping the nanostructures, it is impossible to tell whether a SERS signal is being produced by a single molecule adhered to a single nanostructure. It is for this reason that more sophisticated experiments were attempted to collect SERS data of a single molecule on a single nanostructure. The first of these experiments included the use of a microfluidic chip to increase the amount of control over the position of the nanostructures and possibly enable some optical trapping experiments.

The most intense vibrational bands of R6G lie between 600 cm^{-1} and 1800 cm^{-1}, with bands being caused by aromatic C-C stretching, C-H bending and C-C-C bending. The bands between 1300-1650 cm^{-1} are caused by the C-C aromatic stretch of the aromatic ring of R6G (Figure 17a). The bands at 1120 cm^{-1} and 770 cm^{-1} arise from the C-H bending, both in-plane and out-of-plane bending. And finally, the peaks at 610 cm^{-1} are a result of the C-C-C in-plane bending of the carbon aromatic ring of the R6G.[74, 75] The vibrational bands of CV lie between 1650-600 cm^{-1}, with these bands made up of C-C aromatic ring stretching, in-plane C-O-C bending, both in-plane and out-of-plane C-H stretching and bending along with C-C-C ring bending (Figure 17b). The C-C aromatic stretching bands lie between 1650 cm^{-1} and 1360 cm^{-1} and consist of four bands at 1652 cm^{-1}, 1576 cm^{-1}, 1511 cm^{-1} and 1364 cm^{-1}. The remaining vibrational modes are ex-

pressed as single peaks at 1312 cm^{-1}, 1180 cm^{-1}, 780 cm^{-1} and 614 cm^{-1} respectively for each of the in-plane and out-of-plane stretching and bending modes. C-N bending modes may also be observed at 900 cm^{-1} and 420 cm^{-1}.[76] Shifts in SERS peak posi-

(a) Sourced from [77]

(b) Sourced from [78]

Figure 17: Resonance Raman Spectrum of Rhodamine 6G [77] (a) and Crystal Violet [78] (b)

tions are expected in the Raman spectra of both crystal violet and R6G, as the chemical adsorption of the dye molecule onto the nanostructure will perturb the equilibrium bond lengths and force constants of the dye molecules. It is important to consider that there are other vibrational modes available inside both dye molecules that are often too weak to be accurately recorded with conventional Raman setups. These may be observed when the dye molecules are at single molecule range and sufficient enhancement is achieved. These and other vibrational modes may also only be observed when the dye molecule adheres to specific, high energy areas of nanostructures such as the corners of nanocubes. The difference between a shifted peak and an unexpected peak is difficult to determine, fortunately the expected peaks for both dye molecules are known and have been extensively researched. Labelling of peaks within an expected peak region can also be difficult, as Raman peaks can be shifted depending on the chemical environment of the dye molecule during SERS collection. It is for these reasons that peaks within the literature regions will be considered peak shifted SERS peaks, while peaks outside the literature regions are considered unexpected peaks, that are being caused by contamination or other sources.

3.1.2 Microfluidic Raman Spectroscopy

When collecting SERS data using the microfluidic chip (Figure 18) the laser was focused on the main channel of the chip and moved along its length in between data collection runs to stop any build-up of nanostructures on the roof of the channel. After extensive lasing in one location the dye molecule/AgNS mixture began to carbonize and stick to the glass roof of the channel. The gradient force caused by the focused laser beam caused the movement of AgNS towards the roof of the channel, where they could become trapped when the gradient force is strong enough to overcome any Brownian motion they experience while in solution. R6G was the target molecule of choice for all the microfluidic channel SERS experiments as it provided spectra with the largest level of enhancement of the dye molecules available. Prolonged trapping against the glass will increase the rate of carbonization, as the dye molecules adhered to the surface of the AgNS will begin to burn due to the extended time inside the laser focus. This hypothesis was confirmed when the SERS spectra being collected quickly shifted from the expected sporadic peaks of varying intensity and position, to increasingly intense Raman bands indicative of the D and G bands for graphitized carbon. To overcome this problem, the chip was flushed multiple times with deionized H_2O between samples and after each data collection session. Whenever the appearance of the D and G persisted after flushing with H_2O, the chip was flushed with chloroform to dissolve any R6G that had stuck to the glass surface. Crystal violet could be flushed from the chip with H_2O alone and did not require flushing with chloroform. The collection of SERS data using a microfluidic chip has been researched, with some literature existing on the collection of SMSERS using a microfluidic chip.[79] In the current research the collection of SERS data for each of the nanostructures was achieved using a laser power substantially lower than used for conventional SERS data (1 mW vs 10 mW). If the laser power was unchanged, the dte molecules would rapidly adhere to the glass chip and carbonisation would occur.

The enhancement achieved by using R6G as the dye molecule became problematic when using the microfluidic chip as R6G became strongly adhered onto the sides of the channel. This led to an increased chance of carbonization occurring as the AgNS became stuck inside the laser focus and did not travel further down the channel. This adhesion was mit-

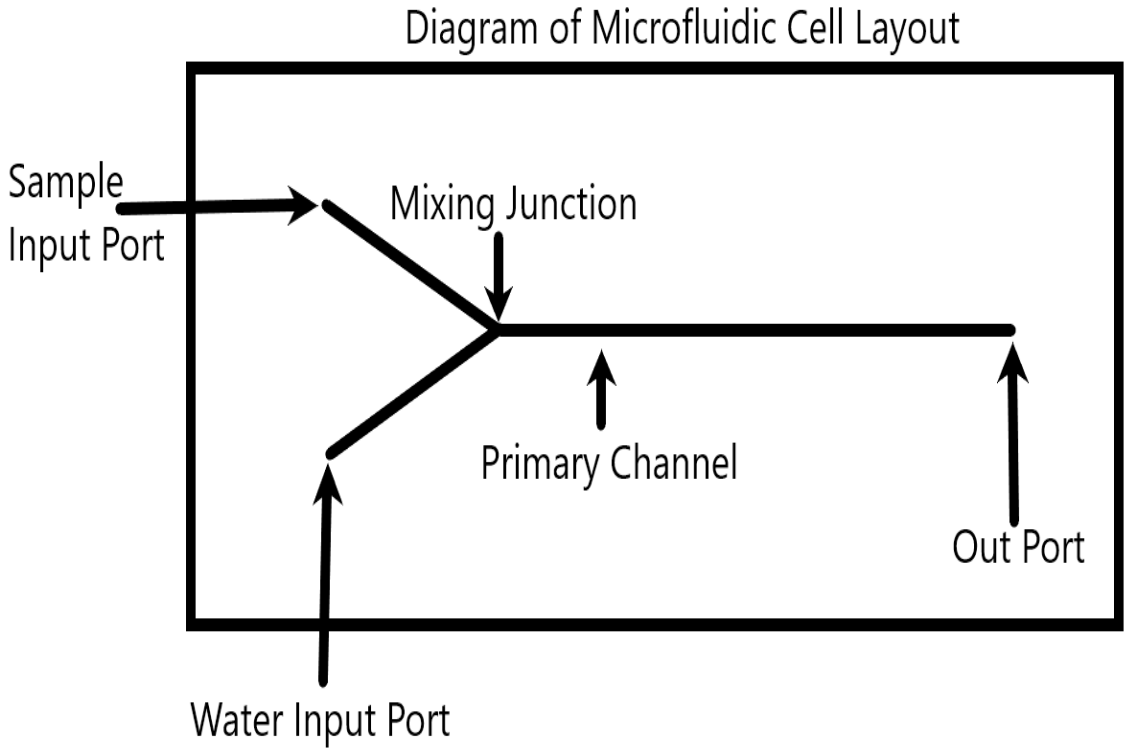

Figure 18: Diagram of the microfluidic chip channel and port layout

igated by increasing the flow rate of the SERS sample into the microfluidic chip. Some adhesion still occurred at the focus, but carbonization was minimised by moving the laser focus along the length of the channel and cleaning the chip between samples. The collection of SERS data was optimised by manipulating the flow rates of the SERS sample and the deionized H_2O and optimizing the laser power to minimise surface adhesion of AgNS, while still enabling the collection of SERS with enough enhancement to overcome any baseline signal-to-noise. The optimal parameters were found to be a low laser power, 1 mW, with relatively high flow rates for the sample and H_2O, 200 nL/s each which is approximately between 1.2 million and 12 thousand molecules per second for samples between 10^{-11} M and 10^{-13} M. A higher laser power greatly increased the rate of carbonization while increasing the flow rate of the SERS sample forced the AgNS out of the focus of the laser faster than the exposure time of the spectrometer, meaning the SERS signal will be diminished. Increasing the flow rate also increased the risk of damaging the chip, as the dimensions of the chip are on the micrometre scale, and an increase in flow rate causes the formation of pressure strong enough to break the walls of the glass channel.

The degree of control provided by microfluidic chips has enabled them to be used for plas-

monic optical trapping of metallic nanostructures, often using multiple lasers to assist in the trapping process.[80] During the collection of microfluidic SERS data some optical trapping may have been observed as an identical SERS signal was recorded over an extended period, roughly 1 seconds or 10 spectra (Figure 19). SERS signal often occurred over 1-3 spectra of 0.1 s exposure time and varied in intensity and peak expression in each of the spectra. The spectra shown in Figure 19 have consistent Raman peak expression, indicating that the AgNS are trapped in the laser focus for an extended period. Unfortunately, it is unclear whether the AgNS are trapped in free space inside channel or if they have been forced against the roof of the channel and are pinned there by the gradient force of the laser.

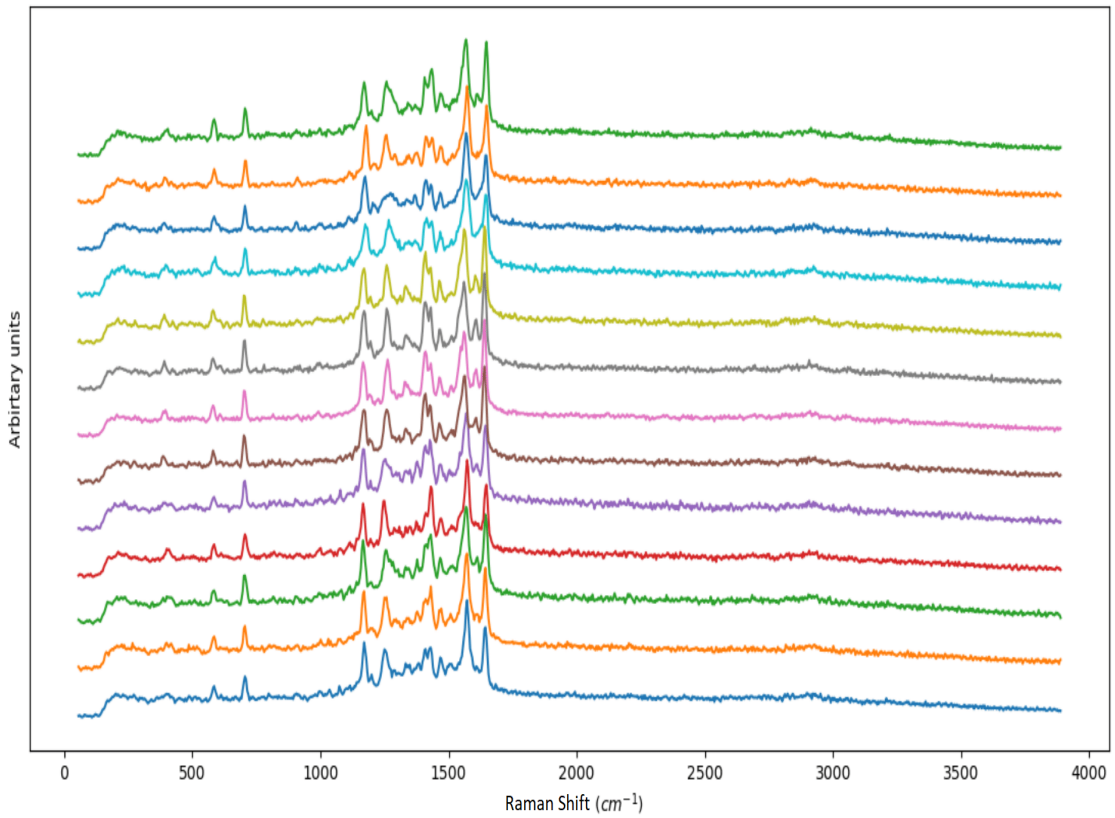

Figure 19: Plot of consecutively collected spectra displaying prolonged uniform SERS enhancement of R6G using the nanocubes substrate using a 3 mW 532 nm laser power with an exposure time of 0.1 s.

When comparing the SERS data collected using the microfluidic chip setup and the conventional SERS collection method the difference is negligible, with similar degrees of enhancement observed using both setups. Given this negligible difference, all SERS data for the samples were collected using the conventional method, as it was easier to set up and collect samples, there were no washing or cleaning protocols required and the con-

ventional method was less prone to contamination. Alongside this, the microfluidic chip failed to provide the consistent trapping required for single molecule/single nanostructure SERS spectra. It is for these reasons that the microfluidic chip was deemed unsuitable for continued experiments and the focus was shifted to the utilization of the optical tweezers setup available at Massey University to develop a Raman tweezers system that has the potential of collecting the desired SMSERS signal.

3.1.3 Plasmonic Optical Trapping

The first challenge faced when attempting to collect SERS spectra from an optically trapped AgNS is achieving sufficient trapping of metallic nanostructures. Optical trapping is often restricted to dielectric particles as the large gradient electric field formed in the middle of the beam focus is unfavourable for small metallic nanostructures and causes them to accelerate out of the trap. Trapping small metallic nanostructures, such as AgNS, is their small size and reflectivity results in the gradient force, typically used to trap particles in the laser focus, to accelerate the AgNS through the laser focus and out of the trap. Recent research surrounding the trapping of metallic and plasmonic nanostructures involve complex optical setups in order to overcome the inherent difficulties of trapping metallic nanoparticles. Despite this, 3D optical trapping of metallic nanoparticles has been achieved for gold nanoparticles.[81] Other common applications of optical trapped metallic nanoparticles involve the collection of analytical data from the trapped nanoparticles such as the collection of a LSPR spectra of a single isolated nanoparticle.[82] The solution attempted to overcome the difficulties of trapping metallic nanoparticles for this project was to deposit the nanocubes, nanowires and nanoplates onto micron-sized silica particles before applying the optical trap on the silica particles rather than the smaller AgNS. The decoration of the silica particles needs to be a partial coverage, as complete coverage would result in complications during trapping, and the particle would begin to act as a core-shell metallic particle rather than a decorated dielectric particle. The decoration process involved the functionalization of micron sized silica particles with an amino ligand before introducing the controlled AgNS. TEM images of the decorated silica particles (Figure 20) showed that partial coverage of AgNS on the silica particles had been achieved for each of the nanostructures. Stable trapping was achieved using the decorated silica

particles, but the optical tweezers setup needed to be modified to collect a SERS signal from the trapped particles. The original optical tweezers setup contained a 675 nm dye laser that was used in fluorescence experiments. Unfortunately, this laser was not suitable for the SERS experiments, as the wavelength was too far above the LSPR peak of the nanostructures, leading to poor energy transfer between the dye molecule and the substrate, resulting in poor SERS enhancement. A problem arose when attempts were made to switch out the 675 nm to a 532 nm laser that was better suited for the collection of R6G SERS spectra. The optical tweezer was built using custom parts and optics that were optimised for a 675 nm probe laser. This meant that several of the optical components were wavelength specific and limited the laser power throughput for any laser that was off wavelength. A direct replacement of lasers was attempted by bringing the 532 nm laser into the optics table via the same fibre optic port but led to poor laser power at the sample and low throughput to the spectrometer, even when using an excellent SERS scattering sample such as sulphur. The 532 nm laser power at the source was 50 mW and was diminished down to 1 mW at the sample. The culprit for this rapid reduction in laser power was a dichroic filter that had been designed to allow 675 nm light to pass through it while transmitting any light below this wavelength. This filter does not have a 100% efficiency, meaning some of the 532 nm light was able to pass through it and reach the sample. As the optical tweezer setup is custom made, the replacement of any components was not available as the setup was used by other people and its alignment needed to be maintained. A work around was attempted, where the optical components of the tweezers were maintained, and the 532 nm laser beam was brought to the objective via a separate laser path to avoid the dichroic filter and any of the other optical components that may be diminishing the laser power. Unfortunately achieving sufficient laser throughput at the sample was a more complicated task than originally thought. Multiple work arounds were attempted, including changing the laser pathway multiple times and using different optical setups with the spectrometer, but a solution to the lower laser power at the sample was not discovered. Due to the time constraints of the project the focus was shifted away from establishing the Raman tweezers apparatus and placed instead on the finishing the SERS experiments and the writing of this thesis. If more time were available the completion

of the Raman tweezers apparatus should be viable as a Raman signal was collected using an initial setup, meaning it should be possible. A Raman signal was collected from sulfur using one of the initial Raman tweezers setups and optical trapping was achieved using the AgNS decorated silica micron size spheres, indicating that both processes required for Raman tweezing was achievable and that with more time a working setup could be established.

3.1.4 Single-molecule Surface-enhanced Raman Scattering

The SMSERS experiment was conducted using the Raman optical tweezers setup which involved the establishment of two optical traps on two decorated silica particles before bringing them close to each other to enable the generation of SERS signal (Figure 20). SMSERS trapping relies on several principals already discussed in this section, including SERS and plasmonic trapping. The adhesion of the AgNS to the silica surfaces was achieved through the surface modification of the silica with an amino silane linking molecule. By controlling both the concentration of dye molecules and the concentration of AgNS, a SERS signal can be collected from a single dye molecule adhered to a single AgNS. This level of precision would theoretically enable the collection of SERS data of a single dye molecule adhered to different positions on a single AgNS. This change in dye molecule position is suspected to be detectable, given the difference in LSPR at different regions. Combining this with the plasmonic optical trapping would enable the precise control of AgNS location and position during SMSERS collection. These types of experiments were of interest for this project as they were suspected to provide the data required to investigate whether the region a dye molecule is adhered to can be isolated and identified.

3.2 Multi-variate Analysis of SERS Spectra

The aim of this analysis was to use a variety of statistical techniques to determine what clustering, if any, occurred within the processed spectral data. The interest in possible clustering was to investigate the hypothesis that there was a discrete number of SERS spectra for each dye molecule based on its position on the AgNS substrate. To observe any clustering, the processed spectral data was analysed further using both PCA and dedicated statistical clustering techniques. It was important to ensure that any clustering of

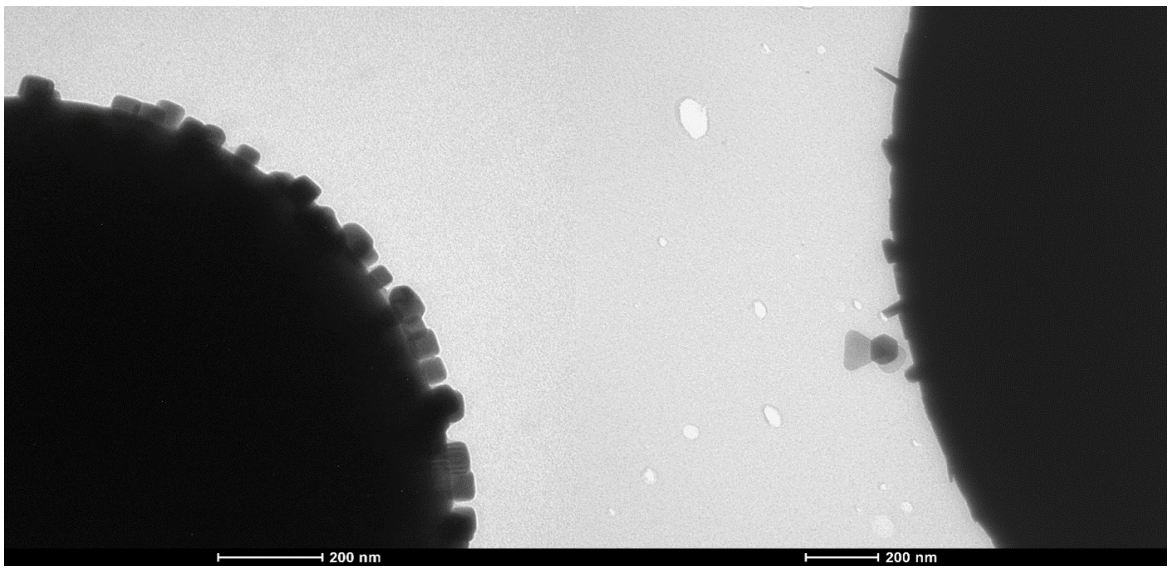

(a) (b)

Figure 20: TEM Images of Nanocubes (a) and Nanoplates (b) adhered to the surface of micron-sized silica spheres.

data points observed could be directly related to the processed spectral data, otherwise the clustering observed may only be observed in the output of the different statistical techniques. Several statistical clustering techniques were compared with each other to get a comprehensive understanding of the patterns and trends that may be occurring inside the processed spectral data.

3.2.1 Principal Component Analysis

The first step of the multi-variate analysis was to process the individual spectra collected using a baseline and normalization function built into the custom Python code. Each SERS experiment consisted of the collection of 600 spectra with an exposure time of 0.1 s per spectra per sample. The occurrence of a SERS signal inside these 600 spectra was low, and most of the spectra only contained the background spectral pattern, usually consisting of two peaks, one for H_2O and the other from the glass coverslip. The baseline and normalization function removed all non-SERS spectra from the list of total spectra by first using an Asymmetric Least Squares Smoothing algorithm to correct for any baseline signal. A normalization algorithm was then utilized to shift the y axis values of the data to fit between 0 – 1 to minimise the impact of maxima and minima peaks on later data analysis techniques. This normalization step was especially crucial as the range of y axis values was large enough to make accurate baseline removal challenging. After both

the baseline and normalization algorithms have been implemented the baseline spectra can be removed by removing all spectra that do not contain a peak with a maxima above a given threshold value. The impact of each of these steps can be visualised in the (Figure 21).

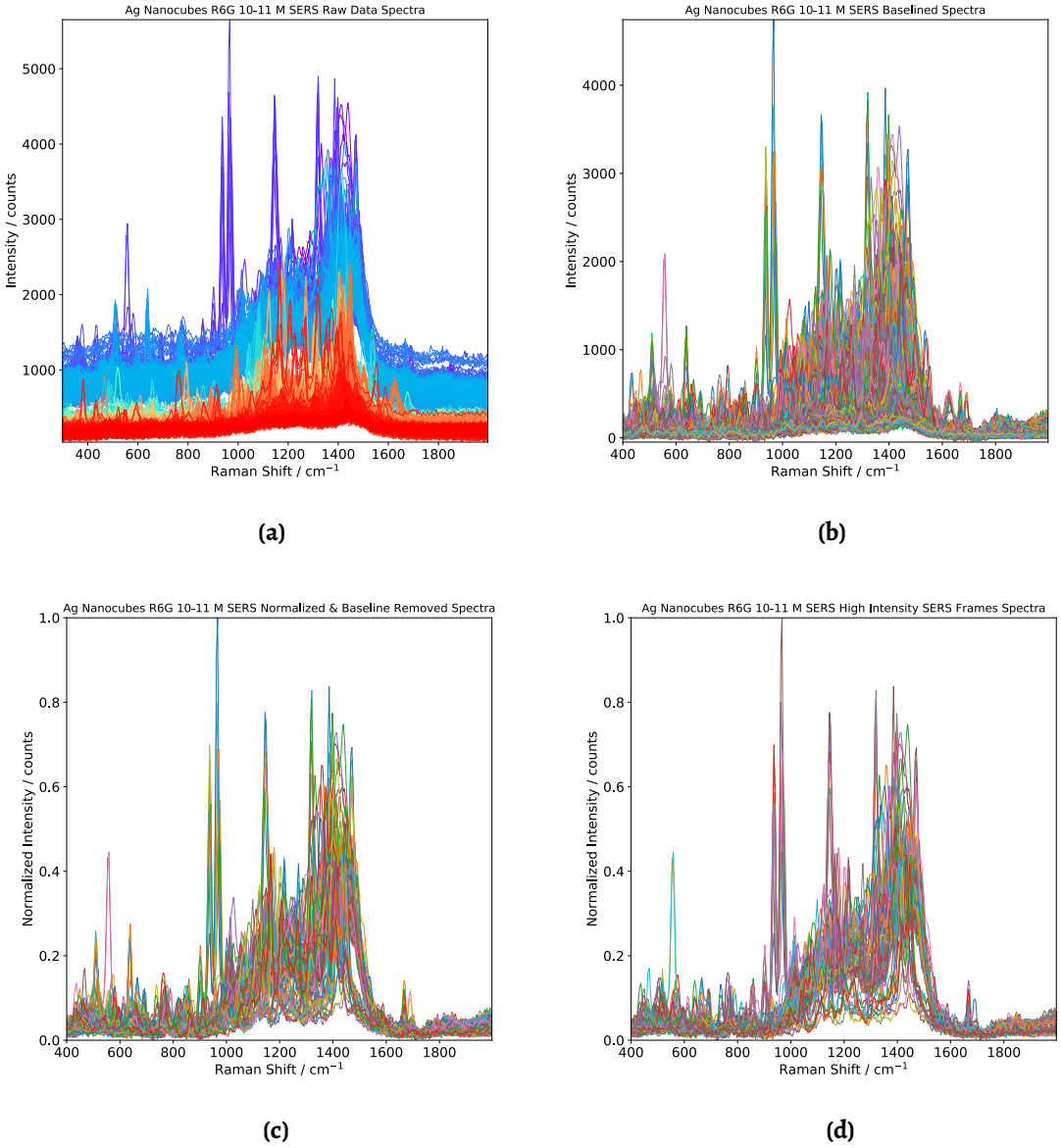

Figure 21: Spectral plots of the different stages of data preprocessing including raw spectral data (a), Baselined data (b), Baselined Normalized data (c), Baselined Normalized data above threshold (d).

The baselined and normalized spectra were then plotted to visualize the data and make preliminary conclusions on the appearance of any trends in the data and to see which Raman bands are being commonly expressed. With pre-processing complete, Principal component analysis was undertaken to reduce the dimensionality of the data into a form that is more interpretable, while still maintaining the spectral information. PCA creates

uncorrelated variables that successively maximise the variance of the data. The creation of the new variables, aka principal components, are defined with the data set available, making the creation of successive principal components are made up of smaller portion of the total data set. This makes PCA an adaptive data analysis technique, that can be thought of producing principal components that best represent the total data. Finding the optimal number of principal components (PCs), i.e., the smallest number of principal components that make up for the most variance, is often achieved using the "elbow" method where a plot of principal component number vs total variance. As the creation of more principal components results in the maximisation of variance, the plot of PCs vs variance results in a logarithmic trend line, so to find the minimum number of PCs responsible for the most amount of variance can be determined through finding the PC nearest to the beginning of the linear portion of the trend line. Another method of determining the suitable number of PCs is by plotting a Scree plot (Figure 22), that shows the variance represented by each of the successive PCs generated. A suitable number of PCs can then be selected based on how much variance is being displayed with them.

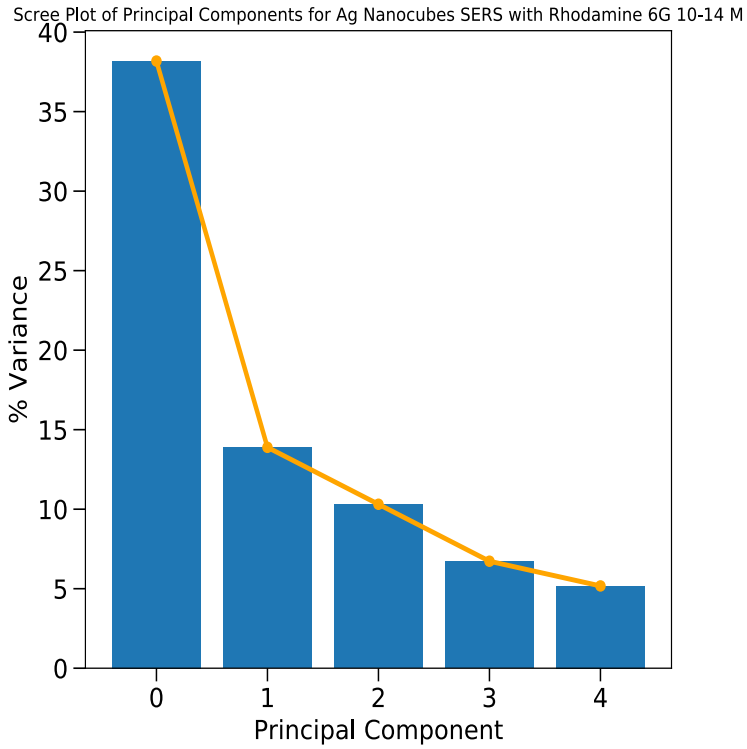

Figure 22: Example of a Scree plot produced using PCA

The baselined normalized spectra were then plotted to visualize the data and make preliminary conclusions on the appearance of any trends in the data and to see which

Raman peaks are being commonly expressed. With pre-processing complete, PCA was undertaken to reduce the dimensionality of the data into a form that was easier to interpret, while still maintaining the spectral information. PCA created uncorrelated variables that successively maximised the variance of the data. The computation of the new variables, a.k.a. principal components (PCs), was defined by the data set available. The creation of successive PCs was achieved using smaller portions of the total data set. This makes PCA an adaptive data analysis technique, that produces PCs that best represent the total data. Finding the optimal number of PCs i.e., the smallest number of PCs that represent most of the variance, is often achieved using the "elbow" method, as shown by a plot of the number of PCs vs total variance covered (Figure 23). As the creation of more PCs results in the maximisation of variance, the plot of PCs vs variance forms a logarithmic trend line. To find the minimum number of PCs responsible for the greatest amount of variance, the PC nearest to the beginning of the linear portion of the trend line will have covered most of the total variance. Another method of determining the suitable number of PCs is by plotting a Scree plot which shows the variance represented by each of the successive PCs generated in bar graph form. A suitable number of PCs can then be selected based on how much variance is being displayed with them. Another method to show this is by plotting the inertia value against the number of clusters. The inertia value used as the y axis of Figure 23 is the sum of the squared distances to the nearest cluster centre. This type of plot shares similarities with the Scree plots produced using PCA and provides an indication of how the variance changes as the number of clusters increases (Figure 22).

The generated PCs, Score's, and Loading's plots for each of sample were used to give a better understanding how the data is being represented by the PCs. The Loading's plot provided a representation of the contribution the original spectral variables to each PC by plotting each of the PCs against the wavenumber range of the Raman data collected. Score's plots were generated by plotting PCs against each other to show how each of the data points inside the PCs were related. This allows for a two-dimensional representation for any possible clustering in the data points that may be occurring. A three-dimensional Score's plot can also be generated by using a third PCs as the z axis, enabling a three-

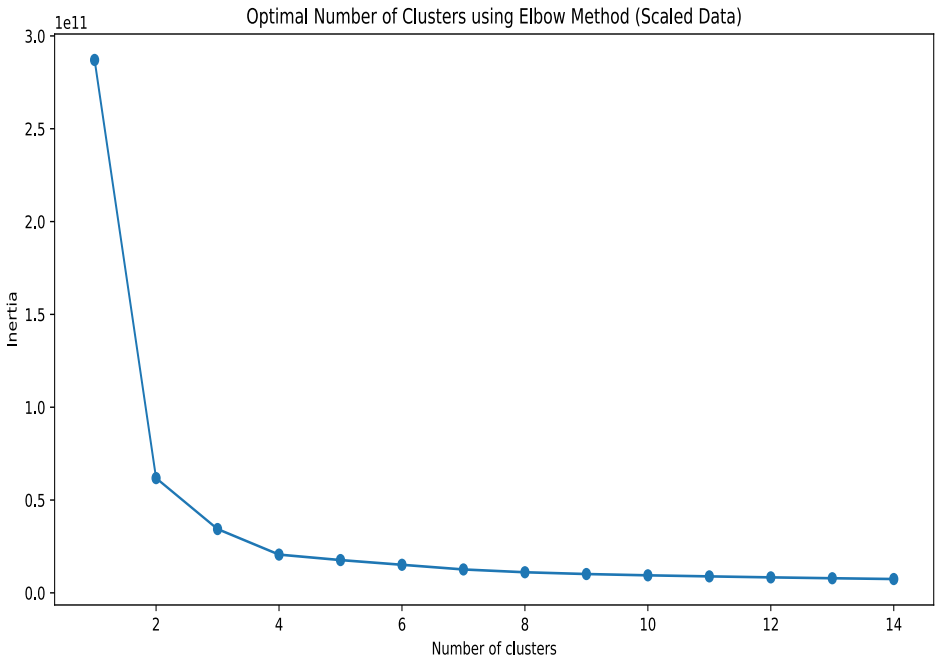

Figure 23: Plot of the variance coverage vs. number of PCs that is used in the Elbow method

dimension view of any clustering that may be occurring. Any clustering present was not clustering between the raw spectral data and instead were similarities between the data points based on how they relate to the PCs. As PCA is an adaptive data analysis technique, it was beneficial to use the first three PCs generated in the formation of a three-dimensional Score's plot, as most of the variance would most likely be represented by these PCs. Five PCs were chosen as they accounted for most of the total variance without requiring an excessive number of PCs. Using too many PCs will greatly reduce the validity of any clustering observed via the Score's plots, as there may be more PC than clusters present, meaning the clusters will be split up to fit the number of PCs. For this reason it is better to initially use the minimal number of PCs that still make up most of the total variance of the system before adapting the number of PCs based on the initial outputs.

3.2.2 Clustering Algorithms

In the hopes of observing clustering inside the processed spectral data several clustering techniques were investigated including k-means clustering, Euclidean distance mapping and self-organizing mapping. Each of these techniques are readily available as functions inside Python, so each were fed the spectral data that had been normalized and baselined,

and the results were collected and compared. During the initial processing of the raw spectral files into the individual spectra a plot is made for each individual spectra and is then saved as an image. These image files were used in the direct clustering, based solely on the appearance of the spectral images and not on the value of the data points.

3.2.3 Euclidean Distance Maps

A Euclidean distance mapping function was investigated to determine whether any evidence of clustering was present in the resultant mapping plot. Euclidean distance mapping produces a distance label for each of the data points inside a given data set based on the distance between each data point. The distance calculation is made using the Pythagorean theorem (Equation 3) for a right-angle triangle, with the two data points acting as the end points of the hypotenuse (Figure 25b). These distances can then be visualised by making a two-dimensional plot with the data points on both axis (Figure 25) and using a separate intensity scale to indicate the distance between data points. As the data points for this project are the processed spectral data, each of the data points seen in the axis of Figure 25 are individual spectra, so the distance value seen between two data points is indicative of how similar the two spectra are to each other.

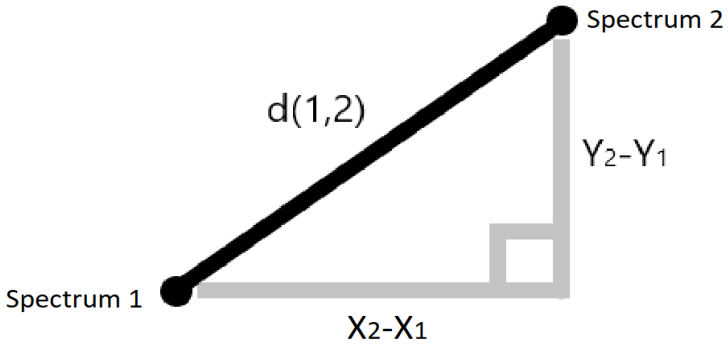

Figure 24: Diagram showing how the Euclidean Distance is calculated between two spectrum; using only two intensity values

$$d(2,1) = \sqrt{((X_2 - X_1)^2 + (Y_2 - Y_1)^2)} \tag{3}$$

Where 1 and 2 are the data points at the end of the hypotenuse with X1, X2 and Y1, Y2 being the Cartesian coordinates of spectrum 1 and spectrum 2.[83]

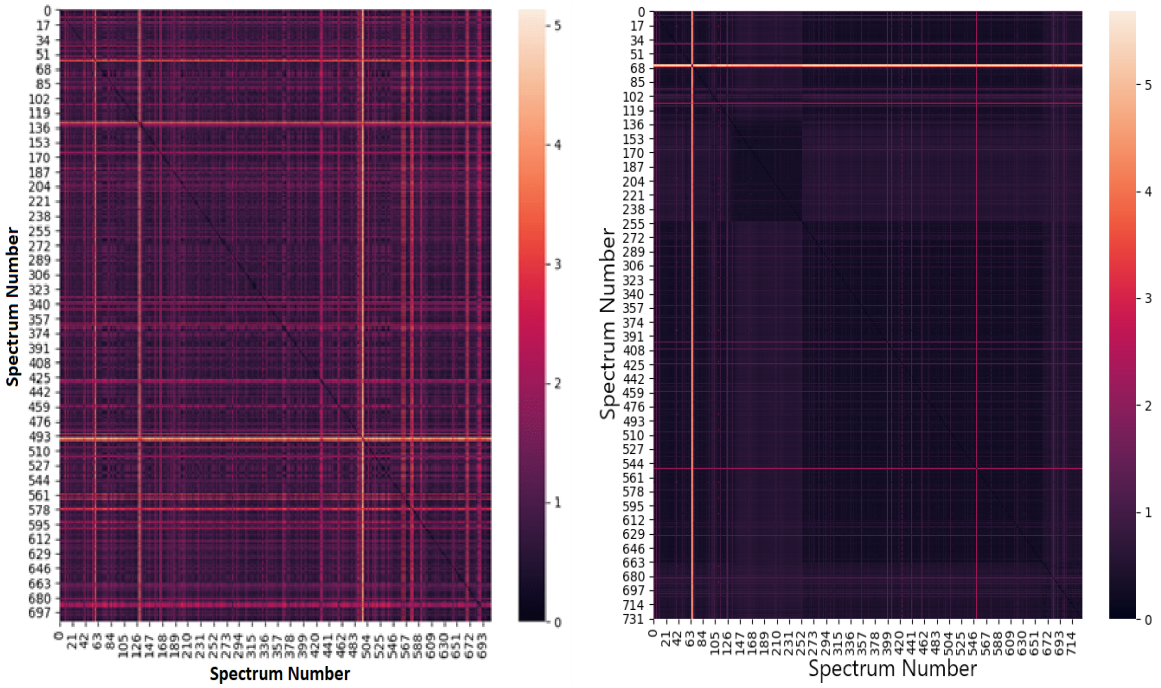

(a) (b)

Figure 25: Euclidean distance example plots showing spectra with large distance differences (a) and spectra with low distance differences (b)

3.2.4 Self-Organising Maps

The creation of self-organising maps (SOM) is an automatic process which is commonly used in the processing and transmission of digital signals.[84] SOM outputs represent a distribution of input data based on a finite set of models that have been establish prior to the input of data. This distribution is automatically associated with nodes on a 2D grid that are organised so that similar models are represented by nodes that are adjacent to each other, while models that share no similarities are placed at nodes distant from each other. Representing the data in this way offers insight into any trends inside the data set and the occurrence of any clustering in the data.[85] If there is already a known number of clusters expected inside the data, then the models can be calibrated to fit this known value. As there is an unknown number of clusters, if any at all, present in the SERS data, no calibration was made to the model. To generate the SOMs used in this project a Python module was used that was sourced from Vettigli.[86]

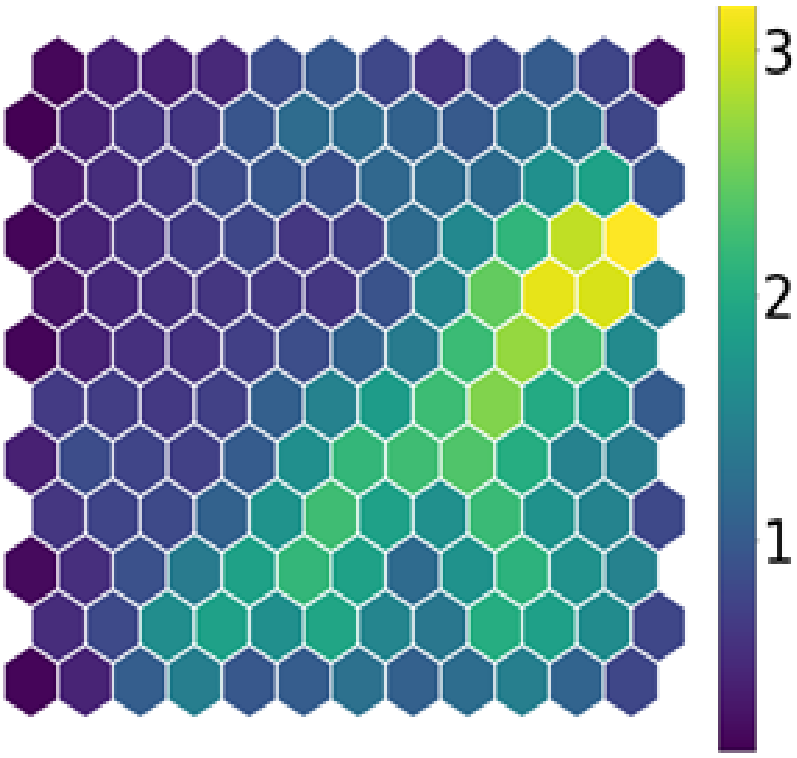

Figure 26: Example of a Self-organizing map

CHAPTER 4

Nanocubes

4.1 Synthesis and Characterisation

The nanocube synthesis followed the method discussed in Section 3.2 and underwent several iterations while attempting to optimize it. The largest difficulty that needed to be overcome was the identification and removal of unwanted etching agents that were believed to be the source of inconsistent results that were originally being observed. Excess amounts of both oxygen and water were originally suspected to be the primary cause of the unwanted etching, so initial testing involved the selective removal of both compounds and observing the effect on the nanocubes produced. Oxygen was found to have minimal impact on the nanocubes formed while the removal of water had a greater positive impact on the nanocubes. The removal of either of these compounds did not however result in the production of nanocubes resembling the literature, meaning an additional compound was responsible for the unwanted etching.

After consulting the literature, it was discovered that the polyol compounds commonly used in nanocube synthesis are often contaminated with trace metals such as Fe^{3+}, which could be responsible for the unwanted etching, because Fe^{3+} is a strong oxidant. The polyol solution, EG, was replaced with an anhydrous equivalent, which appeared to resolve the problems of excessive etching as the nanocubes produced closely resembled the literature nanocubes. The use of anhydrous polyol solvents removes the water from the reaction vessel, which will remove a large portion of unwanted etching. Removing trace metals such as Fe^{3+} is a more complex problem, as the source of these trace metals stem from the synthesis of the polyol solvents, which often involves using metal reaction ves-

sels and lead to metal ions leeching into the polyol solvent.[56] Further attempts at optimizing the synthesis revealed that the quality and quantity of nanocubes produced could be simultaneously improved by completing the synthesis with regents of the highest purity. The best results were accomplished using anhydrous polyol solution and when all reagents used were of the highest possible purity. The best example of this was in the Ag source reagent, silver trifluoroacetate (CF_3COOAg), as the most uniform nanocube synthesis was observed after the switch from the original 98% purity sample to a 99.999% sample. Obviously nanocube synthesis is an incredibly nuanced process and is affected by a range of factors, so it is unlikely that just the removal of H_2O or trace metals impacted the quality of nanocube produced. It is likely a combination of both these factors as well as other factors that were not fully realized. Another factor to consider is my improved understanding in both the reaction mechanism and synthesis in general that occurred during the project. After the changes to eliminate H_2O and trace metals were implemented, the quality of products produced were greatly improved in both the uniformity of nanocubes produced and the quality of the nanocubes themselves (sharp edges and corners). Any changes made after this point were made solely to optimise the edge and corner sharpness of the nanocubes being produced and involved minute changes in reagent concentrations.

4.1.1 Transmission Electron Microscopy

The TEM images collected after the optimization of the nanocube synthesis showed a mixture of nanostructures that were dominated by nanocubes with a low concentration of other nanostructures. The optimization process consisted of maximising the yield of nanocubes, while maintaining their size, shape, and sharpness. This progressive optimisation was followed using TEM as the primary method of characterisation, as it gave the greatest insight into the physical structure of the nanostructures produced. TEM only provided a one-dimensional view of the nanostructures, as the images produced are effectively a projection of the top face of the nanostructures present. Fortunately for this nanostructure, all faces should be identical, so the projection of the top face should be sufficient to determine the overall structure of the nanostructure. The nanocubes shown in the TEM images show some variance in edge length, ± 10% (Figure 27 and 28).

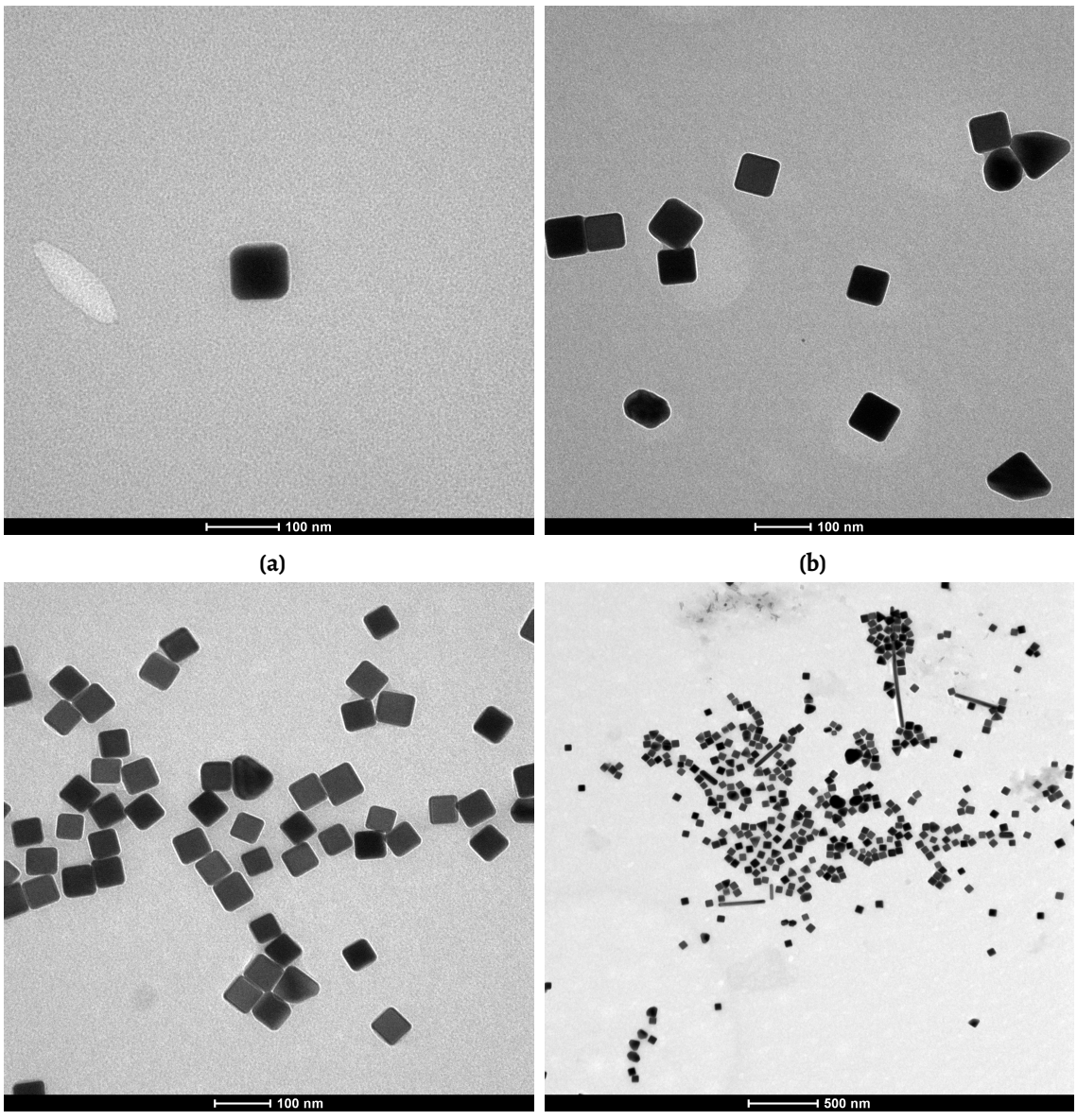

(a) (b)

(c) (d)

Figure 27: TEM Images of Ag nanocubes synthesised using the polyol reaction discussed in Section 3.2

This unfortunately appears to be a persistent problem that is difficult to overcome, as several of the literature images appear to have a similar problem.[55] The overall concentration of nanocubes produced was lower than literature but considering the complexity of this type of synthesis this observation was expected.[35] The appearance of other irregular nanostructures present in these TEM images was consistent with literature, although the concentration of irregular nanostructure present in this work was larger than that of the literature. Due to the kinetics of the reaction, some thermodynamically favourable products were expected to be formed, even allowing for the introduction of reagents to force the formation of the kinetically stable nanocubes. The thermodynamically stable

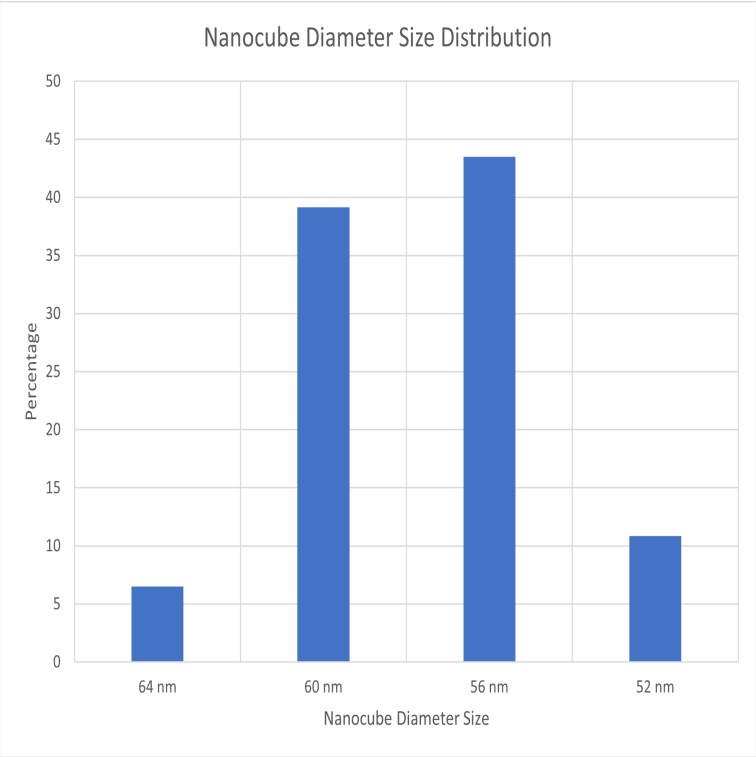

Figure 28: Bar graph showing the size distribution of nanocube diameters

product of AgNS synthesis are often spherical nanostructures, that form over a large size distribution, and are favoured as they minimise surface energy on the available crystal facets. The limitations of using TEM as a characterisation technique arose from the poor resolution of the technique at higher magnifications. Combining this with the metallic composition of the nanostructures, and the thickness of the nanocubes, it was impossible to gain any detailed insight on the surface structure of the nanocubes and the sharpness of their corners and edges. Unfortunately, the scanning electron microscope (SEM) available was also not designed for high resolution imaging, making it impossible to image the nanocubes, let alone inspect their surface structure.

The quality of nanocubes shown in Figure 27 were deemed to be of a suitable quality, with high uniformity and concentration, to act as substrates in subsequent Raman experiments. The final concentration of nanocubes could be improved upon, given a reasonable timeframe, but the results would likely be diminishing due to constant compromise against the formation of the thermodynamically favoured products. As this project was not focused on optimising the synthesis of nanocubes or any AgNS, it was decided that these nanocubes were of high enough quality and uniformity to act as Raman substrates. The separation of the nanocubes from the irregular structure is a difficult task as the ir-

regular structures often have similar sizes and weights. The larger structures were removed via centrifugation, but the structures closer in size to the nanocubes are often impossible to remove completely, as filtration or dialysis are incapable of distinguishing between nanocubes and irregular AgNS. The distribution of nanostructures shown in Figure 29 were determined using the many TEM images collected of the polyol nanocube solution.

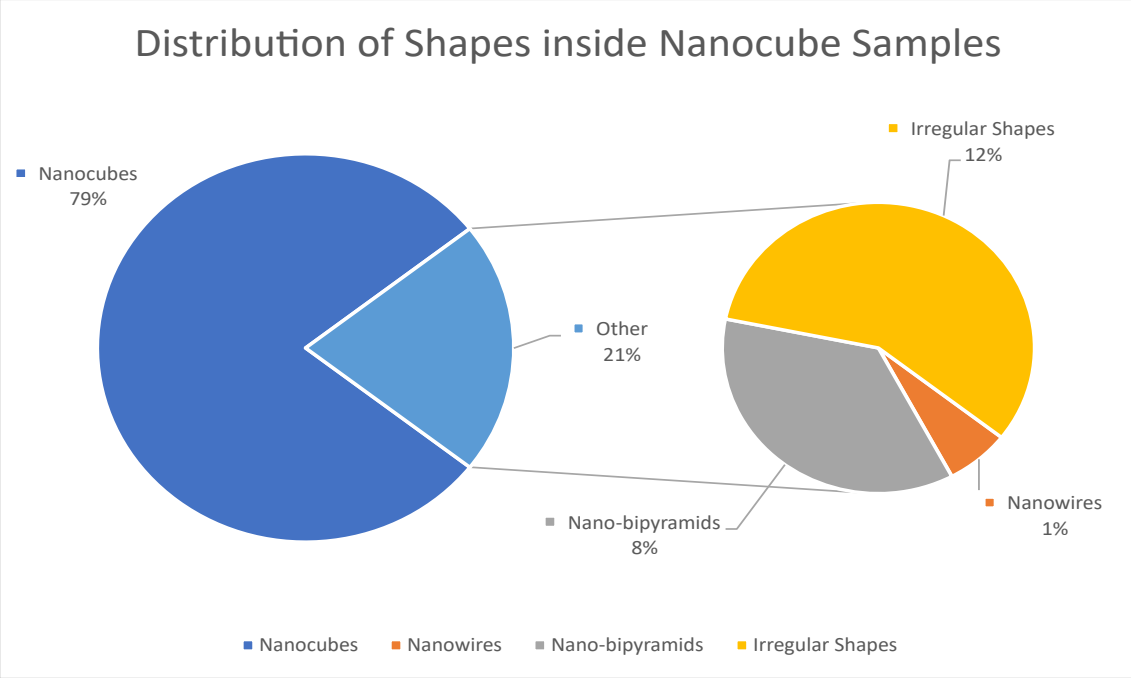

Figure 29: Pie graph showing the distribution of nanostructures present in polyol nanocube samples

4.1.2 UV-visible Spectroscopy

The UV-vis spectra collected of the nanocubes (Figure 30a) showed a single, sharp peak at approximately 450 nm wavelength that had several shoulders below 400 nm. These shoulder peaks have been theorised to be linked with the sharpness of the corners, with the larger the intensity being indicative of the sharpness of the cube's corners.[35] The position of the peak seen in Figure 30a is controlled by the LSPR of the nanostructures in solution, which in turn is controlled by the physical dimensions of the nanostructure. Large nanostructures will have large (or long) wavelength surface plasmons, leading to a red shift in their respective UV-vis peak, while smaller nanostructures will be blue shifted. The uniformity of the nanostructure also impacts the shape of the LSPR peak, as a wide diversity in nanostructure size will lead to a broadening in the LSPR peak, as there will be

a range of surface plasmons present. The sharpness of the LSPR peak for the nanocubes indicates a low range of nanostructures sizes present in the nanocube mixture and when comparing the position of the LSPR peak to the literature, it is indicative of nanocubes with edge lengths between 50-70 nm and is similar in overall appearance.[55] For comparison, Figure 30b shows the UV-vis spectrum for a sample of Ag nanostructures that were produced early in the project. The sample was dominated by irregularly shaped nanostructures with a large size distribution. The spectrum only displays one sharp peak at approximately 300 nm and a large broad peak over the remaining spectral range. The broad peak between 400 nm and 1000 nm was likely indicative of a large size distribution in the nanostructures as a multiple LSPR peaks of different wavelengths will result in this type of inhomogeneous peak broadening.

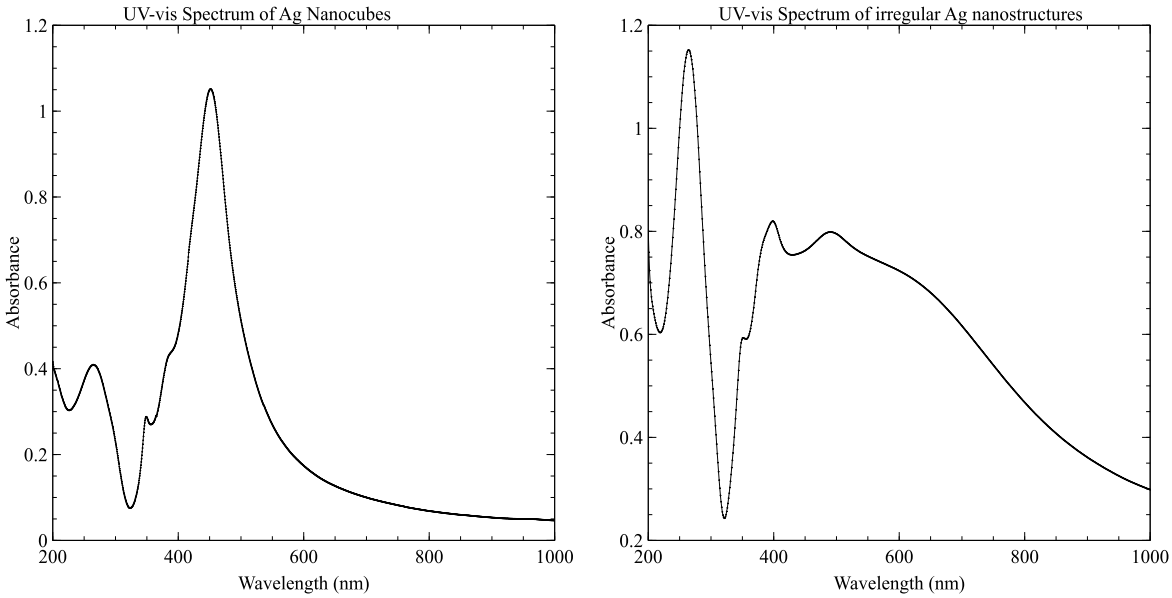

Figure 30: UV-visible spectra of Ag nanocubes (a) and irregular Ag nanostructures (b)

4.2 Raman Analysis

4.2.1 Surface-enhanced Raman Scattering of Rhodamine 6G

The processed SERS spectra of Rhodamine 6G using nanocubes as the substrate are shown in Figure 31a. They show the consistent enhancement of several Raman bands, along with some bands being enhanced in single spectra. There was a baseline peak present between the 1200-1600 cm^{-1} range that was dominated by the D and G band of graphitized carbon.

This indicated that there was probably some carbonation occurring during the collection of the signal. The sharp peaks between 1100-1600 cm^{-1} were caused by the C-C stretching of the aromatic rings of R6G. The peaks between 1000-800 cm^{-1} were the in-plane and out-of-plane bending of the C-H bonds, while the peaks around 600 cm^{-1} were due to the C-C-C in-plane bending. The variance in the peak position within these ranges was most likely a result of the change in the chemical bond strength inside R6G as strengthening of bond strength will cause a shift in their respective peak to a higher wavenumber and vice versa. Another factor that will influence the frequency is exposure to solvents, and molecules at the edges or corners will be more affected than molecules on the faces. The solvent will perturb the electronic structure of the molecules and thus affect the bond strength. The bond strength of R6G may be fluctuating based on their location on the nanocubes, as a R6G molecule adhered to a corner is exposed to substantially more LSPR energy than a molecule adhered to a face. This minor fluctuation in bond strength would result in a slight shift in Raman peak position.

From Figure 31a there appeared to be several regions with high peaks density that were each within a region of interest for R6G, with outlier peaks surrounding these regions. Given the enhancement provided by the nanocubes, the other peaks that are distant from others and only appear in a small number of spectra are likely from dust or other contaminants. At the extremes of the enhancement provided by the nanocubes, some typically weak Raman bands, such as in-plane C-H bending, become strongly enhanced. The amount of variance seen in the peak position and the number of additional peaks was difficult to account for, as the amount of peak shift variance in some cases was significant enough to be caused by bond strength changes and was more indicative of other compounds being present during SERS collection. Given the sensitivity of this SERS collection method it was possible that the contaminant concentration could be as low as $1x10^{-15}$ M and still appear in the collected SERS spectra. $1x10^{-15}$ M was the lowest concentration that SERS spectra was successfully collected at for R6G. Contaminants at these concentrations are impossible to control as they are often present in and around the Raman instrument used for SERS collection and as residue on glassware. Fortunately, any spectra that were dominated by contaminant peaks are minimal in comparison to the total

spectra collected, which will greatly reduce their impact on any analysis conducted using them.

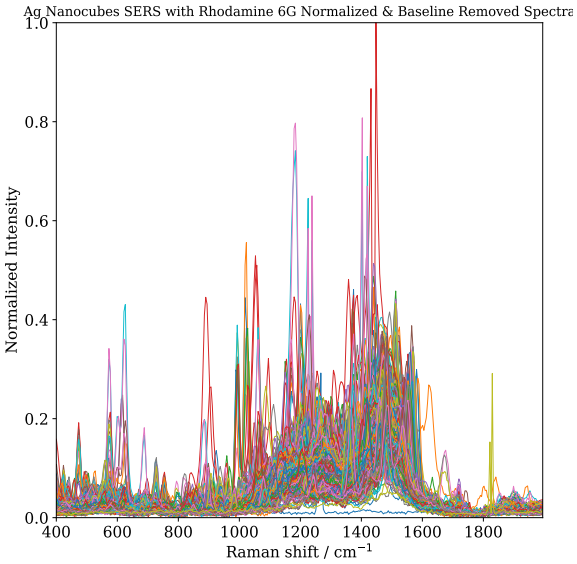

(a) Spectral plot of R6G nanocubes SERS spectra made up of 526 spectra

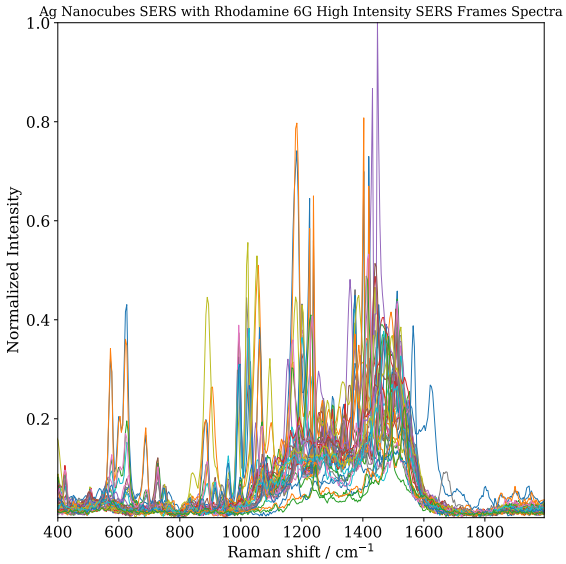

(b) Spectral Plot of R6G nanocube high intensity SERS spectra made up of 261 spectra

Figure 31: Spectral plots of nanocube R6G SERS spectra for both normal (a) and high intensity spectra (b).

During the data processing step a secondary threshold cut off was applied to isolate spectra that contain peaks that are close to the maximum intensity. The plot of these spectra (Figure 31b) provide insight into the extent of Raman band enhancement provided by the nanocubes. This plot of the high intensity spectra had a higher signal-to-noise ratio than the initial SERS plot and showed the extent of band expression achieved when the enhancement at a maximum. Several of the spectra shown in the high intensity plot have a high number of peaks between 1200 cm^{-1} and 1600 cm^{-1} which was considered the region of interest for C-C and C-H bending and stretching modes. Many of these peaks were weak enough that they could be considered background noise, or they could be the expression of bending or stretching modes that are typically too weak to be observed with normal Raman or other SERS experiments. It is currently uncertain which of these is the more likely reason for these peaks' appearance. The enhancement provided by the nanocubes was seen over the entire spectral range and did not appear to be isolated to specific Raman peaks. Given the high number of spectra used to construct Figures 31a and 31b, 526 and 261 respectively, it was difficult to elucidate the appearance of individ-

ual spectrum inside the plots. To overcome this a grid of spectra was produced (Figure 32), all of which were present in the high intensity spectral plot, and showed the range of different spectra present. The difference in band enhancement is clearly shown in this grid, with a range of bands being enhanced over all the spectra shown in the grid. A pos-

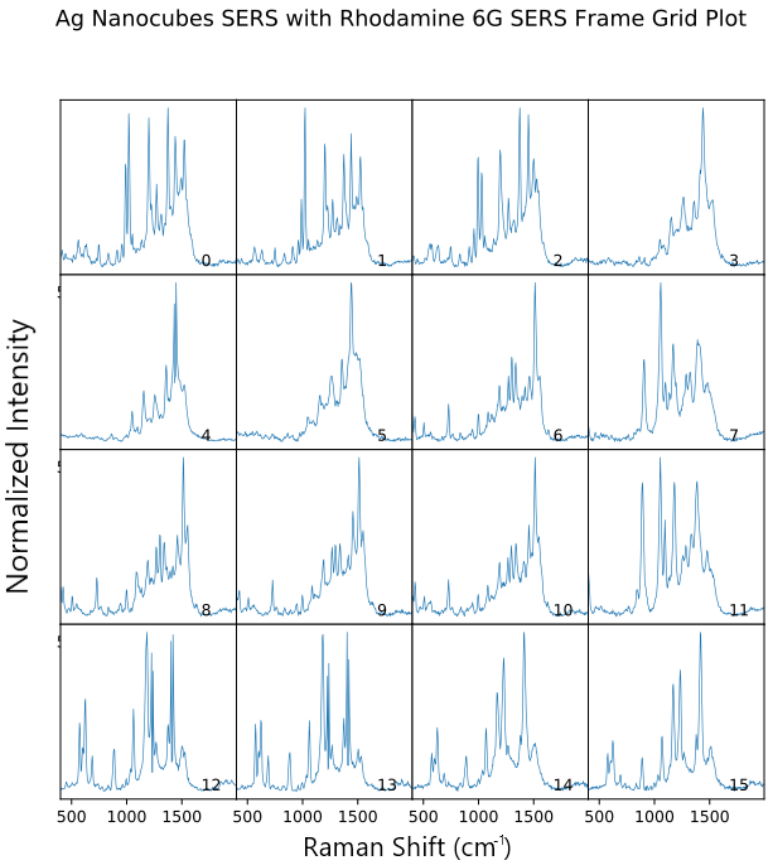

Figure 32: Grid plot of high intensity R6G nanocube spectra

sible explanation for the appearance of unexpected peaks was the capping agent used in the production of the nanocubes. PVP is Raman active but due to its size and structure it would have a different Raman spectrum to R6G. Despite being Raman active a SERS signal for PVP was not obtained when collecting Raman data from a sample of nanocubes with no dye molecule present. This means that PVP is a weak Raman scattering compound and/or is of low enough concentration to not show any peak enhancement above the background noise. PVP cannot be removed from the nanocubes, as it was required to maintain their shape, and without it the nanocubes would rapidly breakdown and form irregular structures. Due to the size of the nanocubes, the concentration of PVP during SERS collection would be within the same concentration range as R6G, and although PVP

is not a strong Raman analyte like R6G, it is possible that the sharp edges and corners of the nanocubes result in some PVP band expression.

4.2.1.1 Principal Component Analysis Data

Principal component analysis was conducted using the SERS spectra isolated after the first threshold cut off was introduced. The Scree plot (Figure 33) produced showed the variance inside the spectra was maximised using 5 principal components, with the first principal component making up around 19% of the variance. The large drop in variance between PCs 1 and 2 most probably indicated that the spectral data was being covered in large part by the first component, while the remaining components covered the remainder of the spectral data variance. The threshold filtering was achieved by running the spectra through a custom Python code that searched each spectrum for maximum peaks and sorted them into two groups depending on if the spectrum contained a peak above a predetermined value. This value was determined based on the strength of the baseline noise of each set of spectra. Only the spectra that contained a peak above this threshold value were used during data analysis.

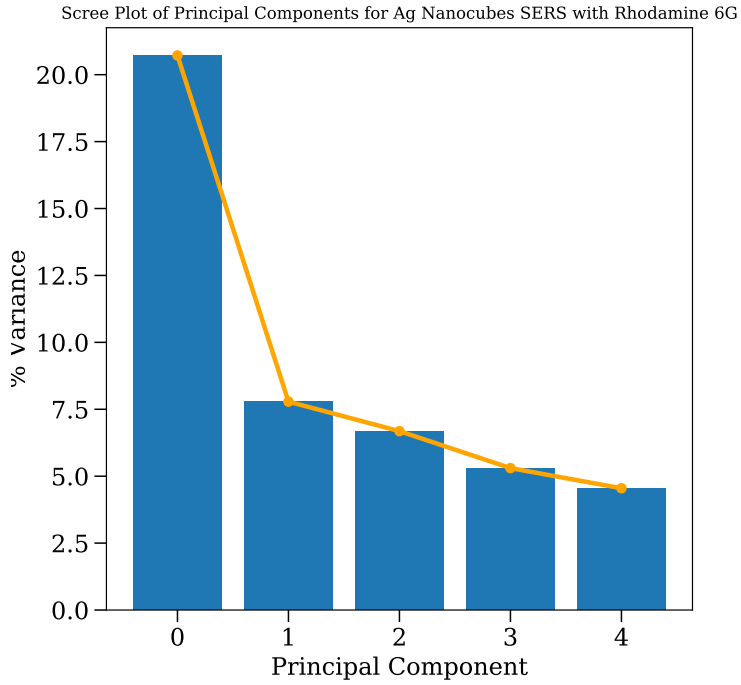

Figure 33: Scree plot of R6G nanocube SERS data

A Loadings plot (Figure 34a) was produced to visualise the appearance of the PCs pro-

duced using PCA. In the Loadings plot the weight of each variable in that PC is plotted against the wavenumber range of the spectra, and if a single component maximises the variance then its respective Loadings plot will have the appearance of an average spectra (Figure 34b). The weight of the variables inside each PC are determined by the variance. The Loadings plot for nanocubes and R6G bore little resemblance to the spectral data, implying that all the components were required to achieve sufficient variance maximization. Along with maximising variance, the Loadings plot also provided information into the degree of variance inside the spectral range, with the height of the Loadings plot being indicative of the degree of variance present at a given wavenumber. The areas of high variance were different between all the components with PC1 showing a high variance area between 1100 cm^{-1} and 1600 cm^{-1}, while the areas of high variance were at 800 cm^{-1} for PC2 and PC5, and 1600 cm^{-1} for PC2 and PC4. These areas of high variance were expected as they appeared over the same wavenumber range as the SERS peaks, and there was an expected difference between the baseline of the spectra and regions where a SERS peak occurred. Variance also occurred at wavenumbers where SERS peaks occur over multiple spectra, as the intensity of the SERS peak differs considerably between spectra.

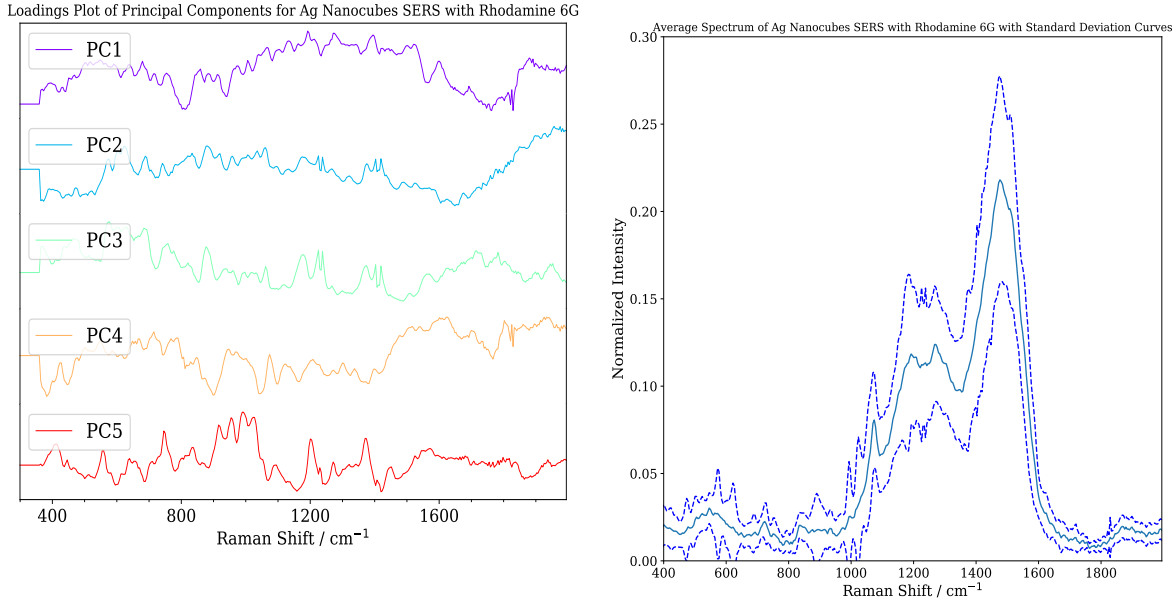

(a) **(b)**

Figure 34: Loadings plot (a) and average spectrum with standard deviation curves (b) for R6G nanocube SERS data

To gain an understanding of how the spectral data's variance was being maximised, a

series of Scores plots were produced using the principal components as axis and plotting the spectra against the respective components (Figure 35a). This produced a 2D plot that showed how related the spectra are to each other based on how well the components represent them. This 2D plot was not enough to develop a complete understanding for how the spectra relate to one another as multiple components were needed to maximise the variance of the data. To improve upon the information provided by the 2D Score's plot array, a 3D Score's plot (Figure 35b) was generated using the first three PCs as the x, y and z axis.

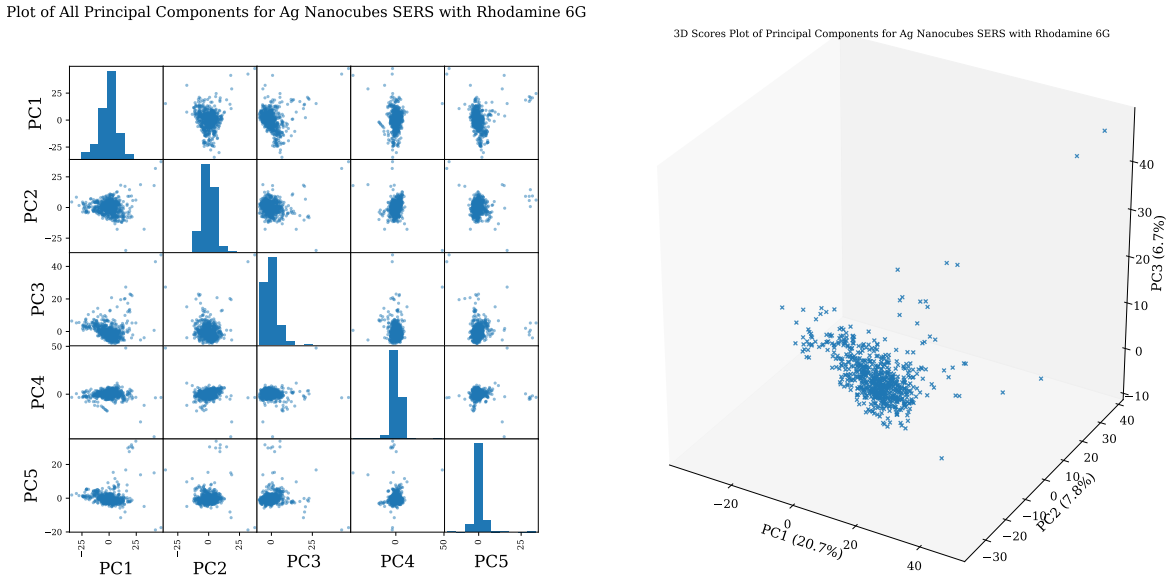

(a) **(b)**

Figure 35: Scores scatter plot (a) and 3D Scores plot (b) of R6G nanocube SERS data

When reviewing the 3D Score plot array, the spectra appeared to form a single, large cluster when plotted against each of the different component permutations. There were also outlier spectra that surround the cluster in each of the Score's plots. The appearance of a single large cluster of spectra was expected in the SERS spectra plots (Figure 35a), as most of the spectra share similarities. The small clusters, especially in the Score's plots using component 1 as one of the axis, could be a result of different spectra being collected of R6G with the target molecule being located at different regions on the nanocubes. Component 1 accounts for the single largest amount of variance of the components used, so Score's plots produced using component 1 as one of the axis would be expected to be more informative on the relationship between the spectra than plots that do not contain component 1. Unfortunately, the information provided by these Score's plots was insufficient

to determine if clustering was occurring inside the spectral data, so a three-dimensional Score's plot was produced using the first three PCs to better visualise the data points. The clustering observed in the 2D Score's plot was also present in the 3D plot, with a tight cluster of data points surrounded by both random outlier points and what appeared to be a trail of data points adjacent to the primary cluster. The tightness of the primary cluster, together with the minimal number of outlier peaks, suggested that there may be discrete clusters inside the primary cluster and that these could not be separated by PCA. Another possible explanation was that an observation bias is being applied and no clusters are present. The trail of data points was an interesting occurrence as it indicated that a continuum of spectra was present, with each successive spectra being slightly different from the last. Another possible explanation for the appearance of the Score's plots could be the ratio of molecules adsorbed on the faces, edges, and corner sites. If the hypothesis that molecules adhered to a face, edge, or corner produce distinguishable SERS signal, then the surface area available for molecules adhere to will also impact the amount of SERS spectra produced. Crystal faces have a larger surface area than edges and corners, so the chance of a molecule adhering to it should be larger than edges or corners. This idea would mean that the large cluster of data points in the Score's plots would correspond to molecules adhered to faces, while any outlier data points would correspond to molecules adhered to edges or corners. Outside of these observations, it was difficult to garner more information from the plots produced using PCA, as the primary cluster was tightly packed and did not appear to contain any secondary clusters.

To better understand how the PCA program was organizing the spectra, the spectra correlated to the outlier peaks observed in the 2D and 3D Score's plot's (Figures 36b and 35a) were isolated and plotted in a grid plot (Figure 36a. From this plot it appeared that the largest similarity between the spectra was the large baseline noise in 5 of the 6 spectra. The first spectra appeared to contain a cosmic spike that was not removed during data processing. Peak enhancement was observed in the remaining spectra, with many peaks occurring at the expected Raman shifts for R6G. The large background noise is possibly the reason for the separation of these spectra from the rest of the spectra. This idea is somewhat supported by the Loadings plot of the nanocube R6G data, with the outlier

spectra being significantly different to most of the PCs. It appeared that many of the outlier spectra displayed in the various Score's plots also related to large Euclidean distance values, which could be indicating that the perceived separation of spectra shown in the PCA outputs is supported by the corresponding Euclidean distance plot.

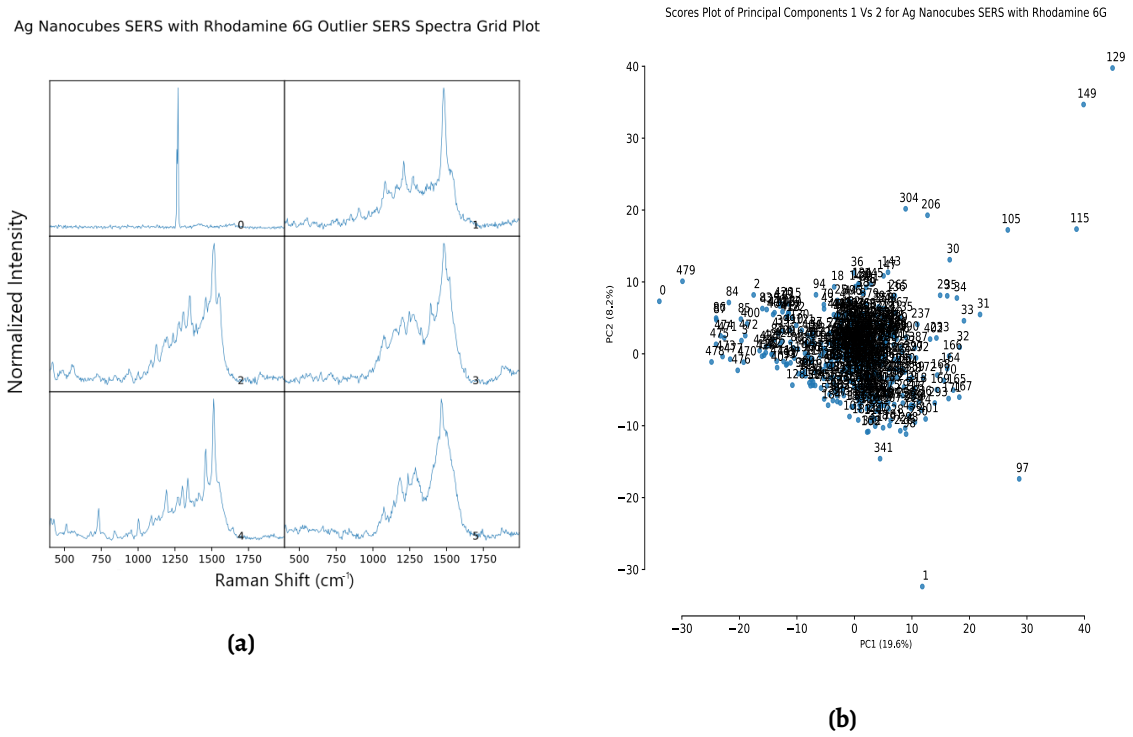

Figure 36: Spectral grid plot of outlier spectra (a) and Scores plot of PC1 and PC2 (b) for R6G nanocube SERS data

4.2.1.2 Clustering Data

The Euclidean distance is the straight line distance between two points inside a 2D plane. The formula (Equation 4) used to calculate this distance is derived from the Pythagorean theorem for the hypotenuse of a right angle triangle, where the two data points sit at each end of the hypotenuse and the length of the hypotenuse is the Euclidean distance. This equation is used to calculate the value that corresponds to a single point in the Euclidean distance map shown below (Figure 37). For data sets such as the ones investigated in this project, each data point will represent an individual spectrum. Given the range of spectra present inside a given data set, best seen in the Crystal Violet section of this chapter, the data points will likely be spread across the entire 2D plane, with some possible clustering occurring for data points that are similar, such as the spectra displayed in Figure 19. The

Euclidean distance between the data points will then represent the degree of similarity between two data points, where a low distance value will be indicative of a large amount of similarity.

$$d(2,1) = \sqrt{((X_2 - X_1)^2 + (Y_2 - Y_1)^2)} \tag{4}$$

The Euclidean distance map (Figure 37) plot produced using the R6G nanocube spectral data offered greater insight into the possibility of clustering suspected inside the data by directly comparing the spectra and determining the Euclidean distance between them. The larger the Euclidean distance, the larger the difference between the spectra, with this distance being represented through the colour gradient scale seen beside the map. As expected from the Score's plots most spectra have a low Euclidean distance, indicating that they are very similar to one another. Unlike the Score's plot however, the Euclidean distance map indicated which of the spectra are very unlike the others. The colour of the lines on the distance map represent the distance between spectra based on the colour gradient scale to the right of the map. The best example of a high distance spectra is the bright line beginning at the 112 spectra number on the y axis running across all other spectral numbers. The bright colour of this line indicates that spectra 112 has a Euclidean distance of at least 2.5 away from all other spectra. This is the major improvement of using Euclidean distance mapping, as it allows for the exact isolation of spectra that are distinctly different from the other spectra. Another interesting feature is the appearance of bands inside the Euclidean distance matrix plot. These bands may suggest that certain sections of sequential spectra have larger Euclidean distances than the average.

An additional observation from the distance map is the large number of spectra with a distance below 1, indicating that they are spectrally similar. These spectra are most probably reasonable for the primary cluster observed in the PCA given the lowest distance between them, while the spectra with large distance values are likely to represent the outlier data points from the PCA plot.

The outlier spectra observed in the Score's plots were linked with the Euclidean distance map output, as they often correlated with high distance values. The spectra that made up Figure 36a, spectra numbered 0, 30, 105, 115, 129 and 149, all appeared to have large

distance values, often above 1.5. Given the appearance of spectrum 0, shown top left of Figure 36a, it was expected that this spectrum would have an extremely large distance value, due to how dissimilar it is from the other spectra. But it appears to have a value similar to the other spectra shown in Figure 36a, possibly indicating that PCA and Euclidean distance mapping discriminate the spectral data differently, leading to different spectra being isolated by the different techniques.

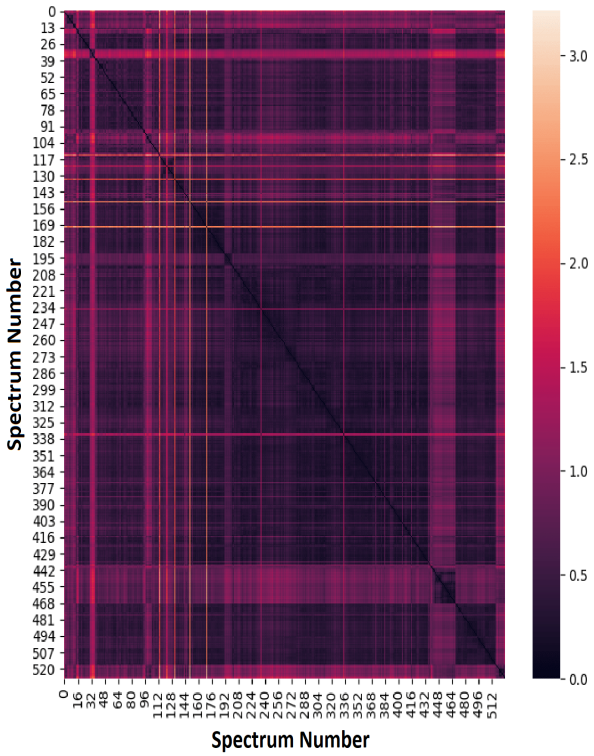

Figure 37: Euclidean distance map of R6G nanocube SERS data

The self-organising map (Figure 38) confirmed the existence of both the large primary cluster and the trail of data points that was neighbouring the cluster in the 3D Score's plot. The primary cluster was most probably being depicted by the yellow nodes in the bottom right corner of the self-organising map, while the trail of data points was most probably the light green nodes neighbouring yellow cluster nodes and the green nodes travelling towards the centre of the map. The green nodes at the top right of the map are possibly another cluster of data points that are neighbouring the primary cluster, given the greenish blue nodes between the primary cluster and this cluster.

From the evidence provided by the PCA, Euclidean distance map and Self-organising map the initial hypothesis of there being a discrete number of clusters inside the spectral data that correspond to SERS signals from R6G molecules adhered to different regions

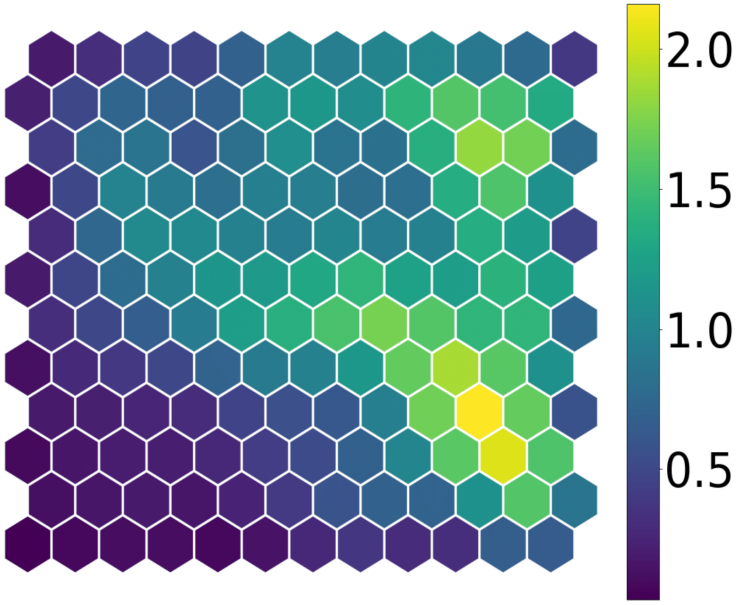

Figure 38: Self-organizing map of R6G nanocube SERS data

on nanocubes appears to be incorrect, as the data seems to form a continuum, where spectrally distinct spectra are at the extremes and most other spectra fit between these points, with neighbouring spectra being slightly different from each other. Another possible explanation for the possible clusters observed in the Euclidean distance map stems from the idea brought up in the discussion of the Score's plot where the largest cluster of data points correspond to molecules adhered to the crystal face given the large surface area. In this case instead of a clear distinction between the molecules adhered to faces, edges, or corners, there is some degree of variation between the locations to the extent where some of the spectra appear to be similar but belong to a different location.

4.2.2 Surface-enhanced Raman Scattering of Crystal Violet

The SERS spectra collected of CV using the nanocube substrate (Figure 39a) showed some consistency with the expected peak positioning, with obvious peaks at 1580 cm^{-1}, 1300 cm^{-1} and 800 cm^{-1} as best seen in the high intensity spectra. There appeared to be a much larger spread in peak position and/or a larger number of unexpected peaks inside the spectra compared with the R6G spectra. There are several possible explanations for this, such as the chemical shift of peaks could be due to chemical adsorption of dye molecules to the nanocubes decreasing the bond strength of CV.

The high intensity spectra plot (Figure 39b) provided similar insight into the distribution of peaks and clustering that may be occurring inside the spectra compared to the initial SERS spectra. There appeared to be several large clusters of peaks at 1600 cm^{-1}, 1300 cm^{-1} and 800 cm^{-1} with each of these regions having a broad peak distribution of roughly $\pm$ 20 cm^{-1} from the centre of each cluster. The cluster at 1600 cm^{-1} corresponded to the C-C aromatic stretching mode, and is expected to have some variance in peak location due to the difference in chemical environment of the different aromatic carbons inside CV. The cluster at 1300 cm^{-1} corresponded to the C-C centre stretching mode, and the 800 cm^{-1} cluster can be ascribed to C-H bending modes. The remaining peaks outside these clusters were more difficult to assign, as many of them appeared to only occur over a

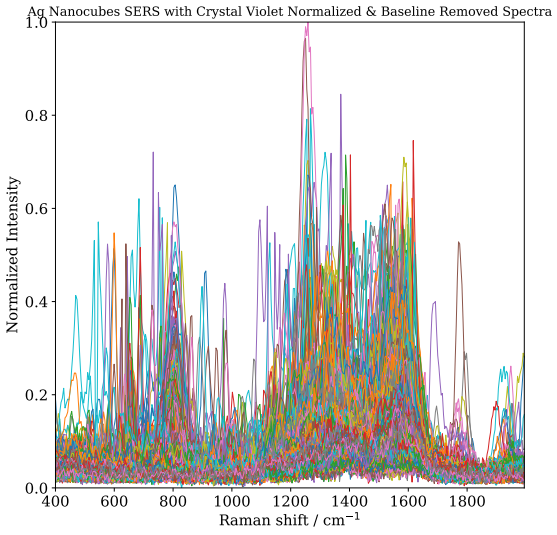

(a) Spectral plot of CV nanocube SERS spectra made up of 706 spectra

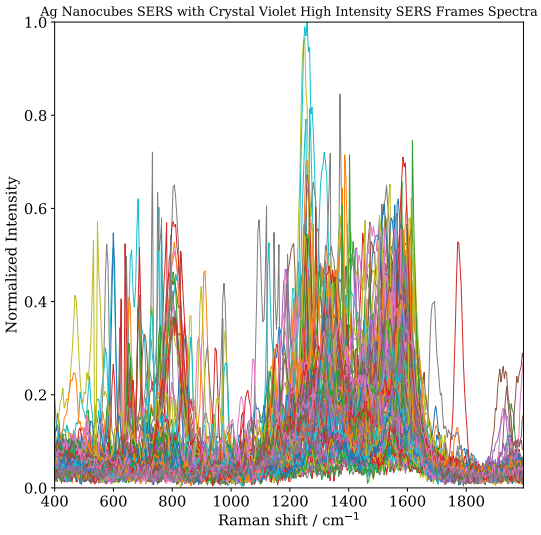

(b) Spectral plot of CV nanocube high intensity SERS dpectra made up of 298 spectra

Figure 39: Spectral plots of CV SERS spectra for both normal (a) and high intensity spectra (b).

small percentage of the total spectra. This suggested that these peaks could be additional stretching and bending modes of CV that are often not expressed, or they could be from an external source such as contaminants. I suspect that some of the peaks between the 1600 cm^{-1} and 1300 cm^{-1} clusters are caused by chemically shifted C-C or C-H vibrational modes but given the poor signal-to-noise ratio in this region, it was difficult to discern much information from either of the spectral plots. There are other vibrational modes expected for CV SERS that were not seen in either of the spectral plots with the same intensity as the already discussed modes. These modes included the radical-ring skeletal vibration and C-N bending vibration mode that should be observed at 900 cm^{-1} and 420 cm^{-1}. Some peaks were observed at the 900 cm^{-1} range but not to the same extent or intensity as the other bands. Only two spectra displayed any peaks at the 420 cm^{-1} range, which was somewhat expected. This was presumed to be because as CV undergoes chemical adsorption onto the nanocubes via the lone-pair of electrons of the nitrogen atom, there is a change in the bond strength of the C-N bond, resulting in a shift in the C-N bending mode to a lower wavenumber, outside the spectral collection range.(Upender et al., 2012)

Much like the R6G nanocube data, the CV nanocube spectral plots (Figures 39a and 39b), which were made up of 706 and 298 spectra respectively, were too densely overlapped to identify trends in which peaks are being enhanced most often. The spectral grid plot produced for the CV nanocube data (Figure 40) provided the greatest degree of insight into which peaks are most readily enhanced, and also showed the diversity in which peaks were enhanced. There appeared to be some similarities between the spectra present, namely plots 4,5 and 8, but there did not appear to be any obvious trends in the other plots.

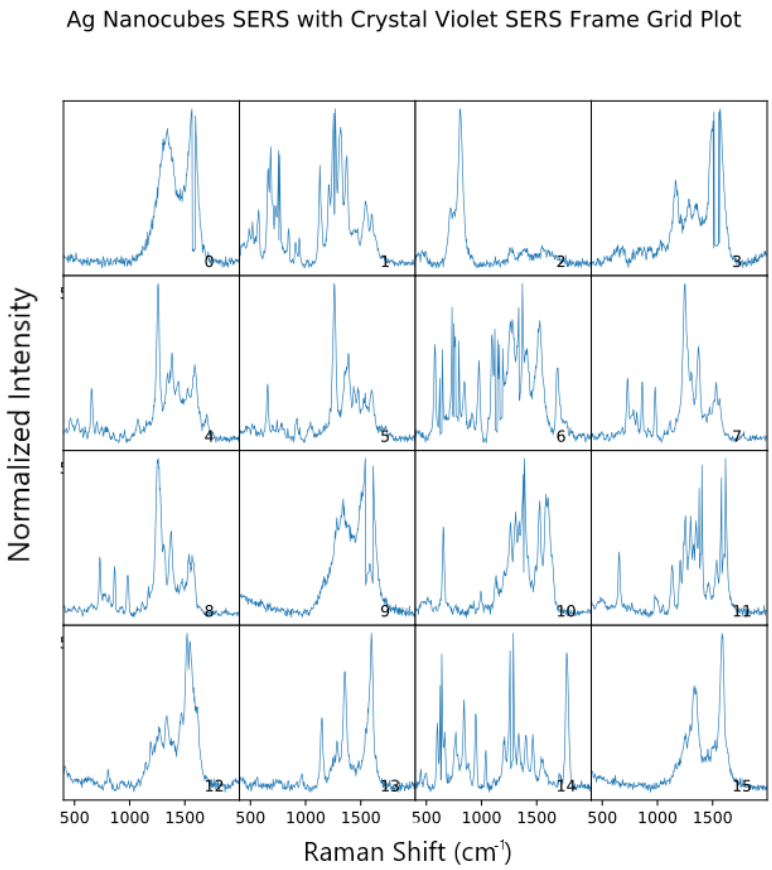

Figure 40: Grid plot of CV high intensity spectra showing the difference in bands being enhanced

4.2.2.1 Principal Component Analysis Data

Much like the nanocube R6G SERS data, the Scree plot (Figure 41) produced using the CV SERS spectral data showed that the first PC contained a significant portion of the total variance at roughly 23%, with the remaining PCs experiencing a drop off in the variance with each successive PC. This variance coverage by the first PC was expected and was also seen in the R6G nanocube SERS data, as many of the spectra used in PCA will have similar peak positions and intensity. The variance shown in the subsequent PCs was most probably derived from spectra that contain chemically shifted peaks and/or unexpected peaks.

Both the Scree and Loadings plots (Figure 41 and Figure 42a) produced using the CV SERS data had similar trends to those of the R6G SERS data. The Loadings plot had areas of high variance near the wavenumber areas of interest that contain a large density of peaks, much like the Loadings plot for the R6G SERS. The distribution of variance in the Loadings plots matched the results from the R6G nanocubes, as the different PCs con-

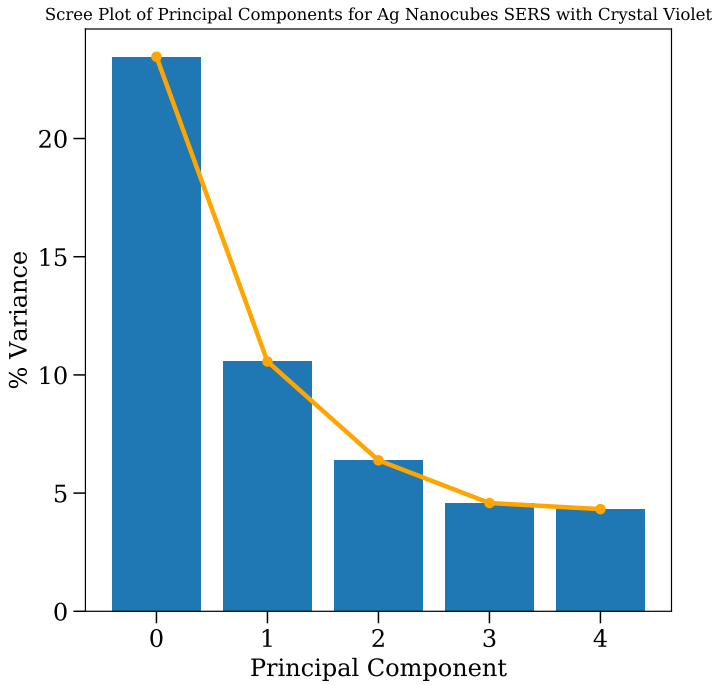

Figure 41: Scree Plot of CV nanocube SERS Data

tained different areas of high variance, many of which do not contain high variance in the wavenumber regions of interest for the CV SERS peaks. As the Loadings plots were effectively spectral representations of the PCs, they do provide information on what the average spectra will look like for a given cluster. Outside of this there wasn't any additional information that can be gathered from the Scree and Loadings plots regarding any possible clustering that may or may not be occurring inside the spectral data. Alongside the Loadings plot an average spectral plot (Figure 42b) was produced to show how the Loading's plot weights correlate to the average spectra. Standard deviation curves are plotted alongside the average spectra to show the range of intensity experienced across all spectra collected.

The Score's plots (Figure 43a) produced for the CV SERS provided more information than the Scree and Loadings plots, especially when inspecting the Score's plots produced using the first PC. Unlike the Score's plots for R6G, these Score's plots showed less clustering within the spectral data, with a much greater spread and separation between the data points. Some clustering was observed for the Score's plots constructed using PC4, but the remaining plots showed very little clustering, with most of the data points being spread across both axis.

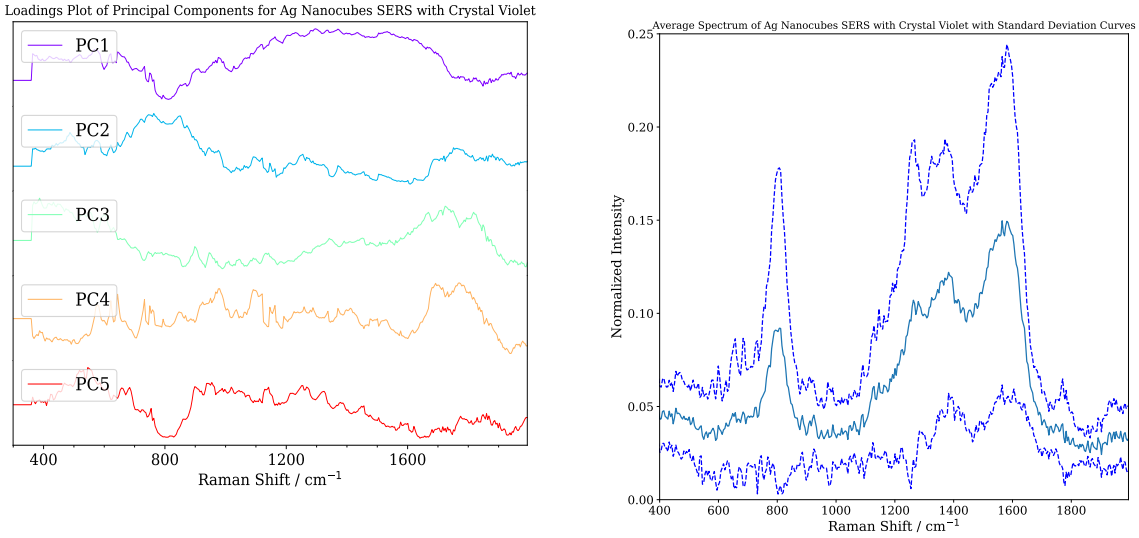

(a) **(b)**

Figure 42: Loadings plot (a) and average spectrum with standard deviation curves (b) for CV nanocube SERS data

The 3D Score's plot of the first three PCs provided some additional information on the large cluster of data points observed in the 2D Score's plots (Figure 43b). There appeared to be a large grouping of data points surrounded by outlier points that span the rest of the plot. There does seem to be some minor separation in the main group at around the mid-point, but as there was overlap of data points in this region it may suggest that this perceived separation may be caused by the orientation of the plot. Outside the main group the data points were widespread and showed no signs of clustering or grouping, appearing as a diverse spread of points over all three axes. There were also some outlier peaks that sat at the extremes of the axes and were separate from the groups and other data points in some cases.

The outlier spectral plot for the CV nanocube data (Figure 44a) displayed similar results to the R6G nanocube data, with all of the plots having broad strong peaks that did not fit with the Loading plot outputs, likely leading to why they were plotted outside of the other data points on the Score's plots. From these plots there did not appear to be any obvious trends as to which peaks were being enhanced, but given how isolated each spectra was on the Scores plots (Figure 63), this was expected, as similar spectra would be grouped together even if they were outliers from the main group of spectra. When comparing the outlier spectra with their respective Euclidean distance value, it appeared that the

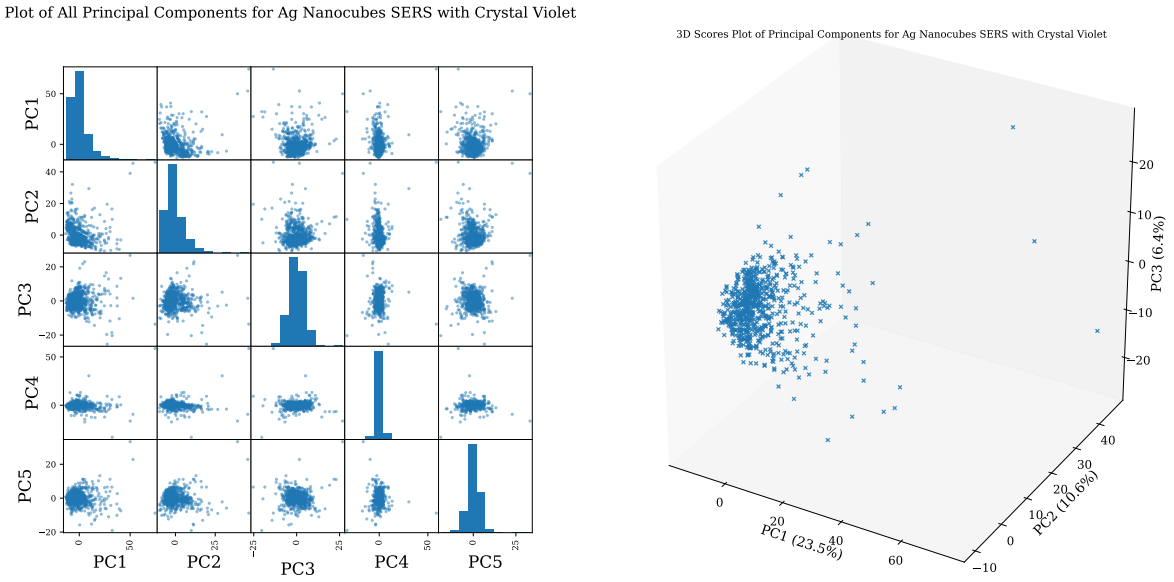

(a) **(b)**

Figure 43: Scores scatter plot (a) and 3D Scores plot (b) for CV nanocube SERS data

majority of them contain values lower than expected given the apparent differences that existed between them and the other spectra. It appeared that spectra 58 had the largest distance value of approximately 4, well the remaining outlier spectra had much lower values.

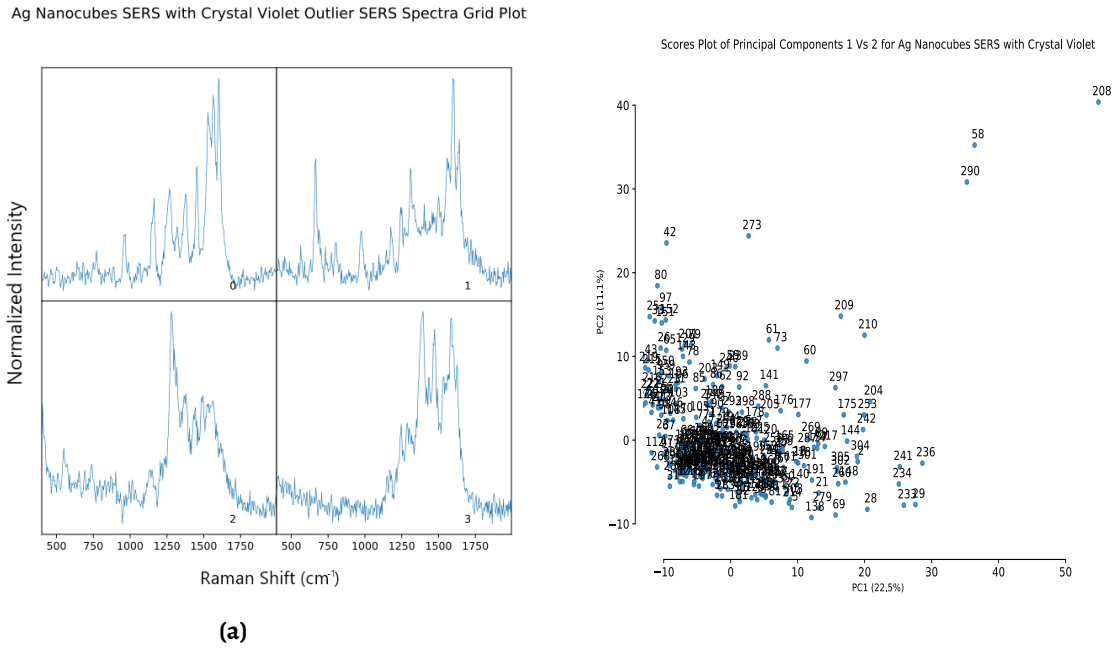

(a) **(b)**

Figure 44: Spectral grid plot of outlier spectra (a) and Scores plot of PC1 and PC2 (b) for CV nanocube SERS data

4.2.2.2 Clustering Data

The Euclidean distance map for the CV data provided more evidence that no clustering was present inside the data (Figure 45). The number of spectra with a Euclidean distance above 2 occurred more often, with several spectra having a distance around 5. The spectra with high distance values are likely to be the outlier data points seen in the 3D Scores plot, while the spectra with a distance above 2 are the data points that are spread out surrounding the two possible cluster of the 3D Scores plot. An additional, and possibly larger piece of evidence against the presence of clustering, was a low Euclidean distance was indicative of spectra there were similar. In comparison to the distance map of the R6G cube data, there was considerably less low distance spectra present in the CV data, indicating that the spectra are more disperse and spectrally different from one another, unlike the R6G distance map that indicated a significant portion of the spectra were spectrally similar, as indicated by the large number of spectra with a Euclidean distance below 1.

When comparing the outlier spectra, seen in Figure 44a, with the spectra identified with

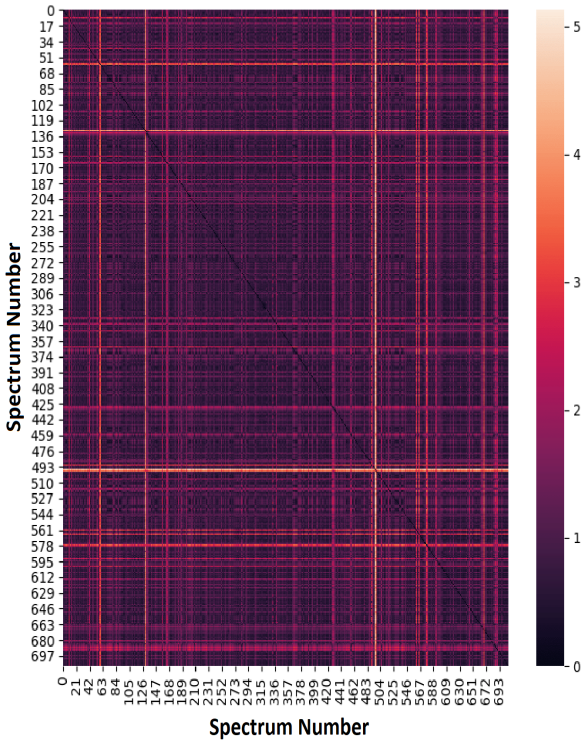

Figure 45: Euclidean distance Map of CV nanocube SERS data

large distance values in the Euclidean distance map, there did appear to be some overlap. The outlier spectra plotted in Figure 44a were linked to high value spectra on the distance map, namely spectra number 42, 58, 208 and 290, all of which appear to have distance

values above 3. Surprisingly, the spectra with the largest value, spectra 495-7, were not displayed on either of the Score's plots as outlier peaks. As Euclidean distance mapping and PCA involve different mathematical methods of separation it is possible that several spectra could have been separated from the main group using one technique and clustered together with the main group in another. Nevertheless, the outlier peaks that were present in the Score's plots were identified on the Euclidean distance map, indicating that the techniques did share some similarities how they discriminate between spectra.

The self-organizing map constructed with the CV data (Figure 46) partially validated the theory of a large cluster existing inside the data as it showed a single, large grouping of points (blue nodes). This cluster is dispersed over several nodes that progressively get more spectrally different, indicated through the change in colour from blue to green to yellow. The green nodes inside the blue cluster have a distance difference, indicating that instead of a discrete number of clusters existing inside the data set, it was more likely that a continuum of spectra existed, similar to the R6G nanocubes data, but with a much larger spread and variance. The yellow nodes probably represent the outlier peaks, given the large distance values compared to the surrounding nodes.

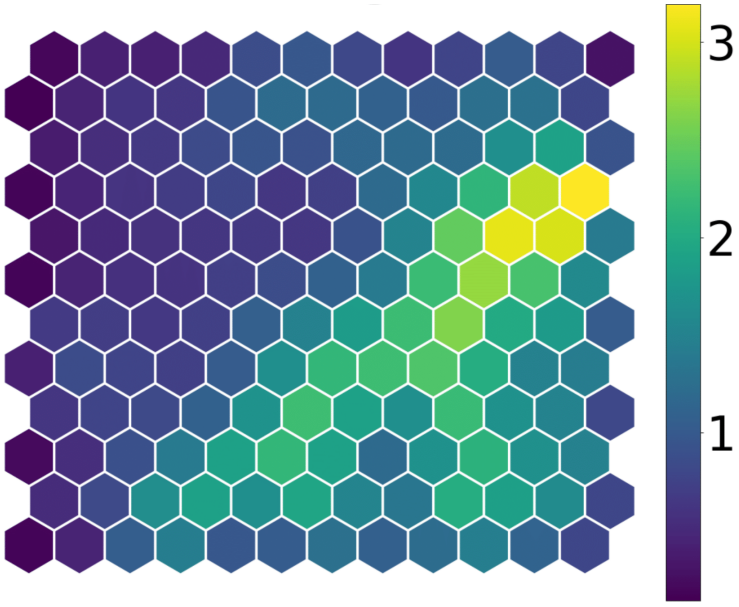

Figure 46: Self-organizing map of CV nanocube SERS data

This theory would be consistent with the evidence provided by both the PCA and the clustering algorithms, as the PCA and self-organising maps showed the existence of a

large, wide-spread cluster, while all three outputs effectively refuted the existence of multiple, discrete clusters, which was the original hypothesis.

Unfortunately, linking the clusters observed in the self-organizing map with the exact spectra they represent was more complex than with the Euclidean distance map. This was because during the generation of the self-organizing map the spectrum number labels are separated from the spectral data and discarded, resulting in the final output map of the spectral data becoming disconnected from the spectral labels. During the generation of the Euclidean distance map these labels are maintained, which lead to precise links being possible between the map and the PCA outputs, which also maintain their labels.

4.3 Summary

After reviewing the data collected using the nanocubes over both dye molecules, it appeared that the R6G adhered to nanocubes produced the greatest SERS enhancement with the highest uniformity and consistency with respected to which Raman bands were being expressed. Despite this excellent SERS enhancement however, the nanocubes failed to replicate this enhancement when adhered to CV. Alongside this, the SERS data for both dye molecules did not provide conclusive evidence in favour of the clustering theory, and instead provided possible evidence towards the continuum theory. The overall uniformity of the nanocubes may have been a limitation to the collection of quality SERS spectra/-data. I suspect that the appearance of irregular nanostructures inside the nanocube solution impacted the quality and consistency of the SERS signal collected, resulting in more variation in the SERS spectra collected. This would account for the large number of outliers in both the R6G and CV data and could also be the reason behind the loosely packed cluster observed in the CV Score's plot. Improving the uniformity of the nanocubes was theoretically possible and has been shown to be experimentally possible in literature but would require a greater time commitment than was available for this project. Nevertheless, the data collected using the synthesised nanocubes provided considerable insight into the quality and enhancement of SERS collected, and what patterns and trends may be present inside the SERS signal.

CHAPTER 5

Nanowires

5.1 Synthesis and Characterisation

During the optimisation of the nanocube synthesis, a product of one of the methods included an abundance of nanorods and nanowires. At the time nanorods and nanowires were not the target structure, so the observation was noted, and work continued into the optimisation of the nanocubes. After the method of nanocube synthesis was deemed suitable for this project, the focus was shift to other structures that could act as comparative surfaces to the nanocubes in Raman experiments. Nanowires were chosen as one of these structures due to their shape, size and more importantly their edge to corner ratio being larger than nanocubes. Thanks to the observation of nanorods and nanowires, their synthesis was easier to isolate and replicate. The only difference between the synthesis of nanocubes and nanorods/wires was a slight change in the concentration of etching agent and a shift in the PVP:Ag atom ratio to favour the formation of larger structures by minimising the degree of surface coverage and facet pacification that PVP had on the Ag(0) clusters. These changes were both easy to implement and optimise, making the formation of nanowires relatively straightforward. The difficulty in nanowire synthesis arose when attempts were made at controlling the length of the nanowires formed. The etching agent was responsible for this, as when in excess it would actively inhibit the formation of longer structures, while too little etching agent result in the formation of irregular structures. The interest in controlling nanowire length was to ensure a large difference between the physical dimensions of the nanocubes and the nanowires, so a comparative study could be run with guarantees that any differences observed were being caused by

these physical differences. Fortunately, a method was developed that lead to the formation of long nanowires with consistent width distribution. The lengths of the nanowires produced were more widely distributed than the nanowire width. Growth on the facets responsible for the width of the nanowires are controlled by actively capping the facets with a capping agent. Controlling the length of the nanowires was more complex than controlling the width, as the facets located at the ends of each wire are uncapped, allowing for growth to occur unimpeded. It was for these reasons that the length of the nanowires was not actively controlled for, while attempts were made to control the width of the nanowires.

Much like the nanocube synthesis, the formation of irregular structures alongside the desired product was prevalent in the nanowire synthesis. A review of the literature found that this was found that this problem is systemic in all Ag nanowire synthesis, and that a yield of under 80% nanowires was common for these types of synthetic methods.[87] Unlike the nanocube synthesis however, this problem was easily mitigated through centrifugation, as the nanowires were often 10-15x larger than the irregular structures and rapidly pellet out of solution when spun, making it possible to isolate the nanowires with minimal effort.

5.1.1 Transmission Electron Microscopy

The TEM images shown below (Figure 47) of the nanowires were collected after the washing procedure (discussed in Section 2.6.1) had been completed. Most of the smaller structures formed during nanowire synthesis were easily removed using centrifugation, but some did remain, possibly adhered to the surface of the nanowires, or were stuck to one another via an interaction between the PVP molecules capping both structures. Given the ratio of nanowires to irregular structures after centrifugation was massively in favour of the nanowires, the adhesion of these irregular structures should not have a large impact on any Raman experiments. When investigating the quality of nanowires produced there was some variance in the width of the nanowire, ±10% on the average width of 50 nm, and a large variance in the length of the nanowires. The growth of the nanowires was only halted when the concentration of free Ag(0) atoms reaches 0 and each available site on the

growing nanowires has equal surface energy, meaning a distribution of nanowire lengths was expected. The width distribution was probably caused by some of the nanowires receiving insufficient surface capping by PVP, resulting in unwanted growth on the capped (111) facet. The appearance of this nanowires width distribution should not impact the Raman signal produced, as many of the nanowires are similar enough to dominate any Raman enhancement observed.

The multi-twinned crystal structure of the nanowires can be clearly seen in Figure 47a, with the ends of the nanowire being the meeting point of the many facets capping the nanowire, resulting in a rounded appearance. Unlike nanocubes which are capped by identical facets, the nanowires are capped with multiple facets, which leads to the end of the nanowires forming into a point where all these facets meet. These facets run the length of the nanowire and are observed through the contrast shown in the TEM images, as there was clearly an edge facing in the direction the image was collected, resulting in a dark line running the length of the wire. The nanowire was probably resting with the edge facing towards the electron beam, with this edge being the point of focus for the TEM, causing the facets beyond the point of focus being less affected by the electron beam. As these nanowires were produced using a method developed during the project it was difficult to accurately compare their appearance with other literature images. Many of the literature methods were attempted during this project, with the hopes of reproducing their results, but none were as successful as the method developed from the nanocube synthesis. Many of the most cited nanowire synthesis methods required the simultaneous addition of the silver salt solution and capping agent via a dual channel syringe pump system, which unfortunately was not available, making it difficult to accuately reproduce the methodology and results.

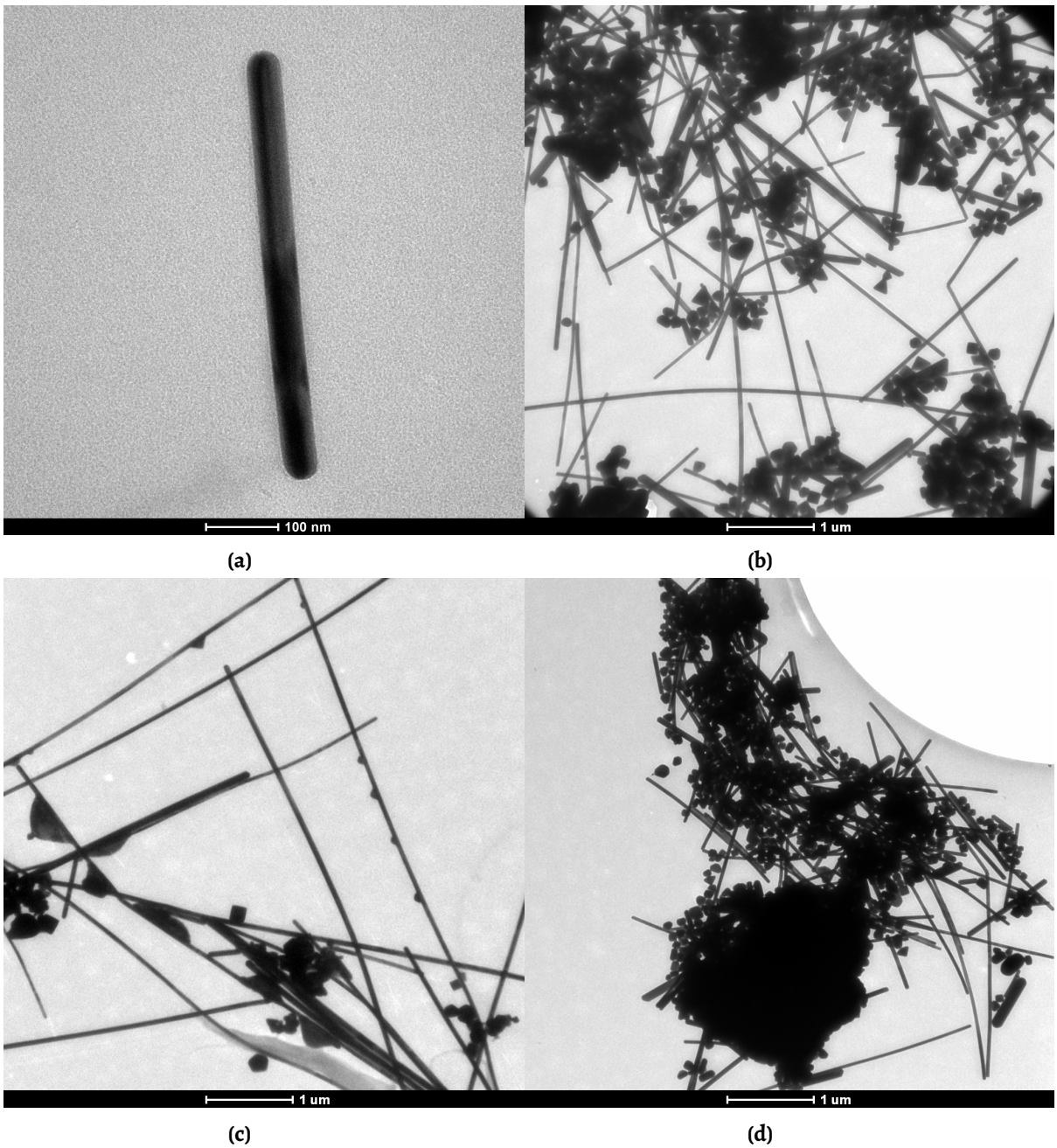

Figure 47: TEM Images of Ag nanowires synthesised using the modified polyol method discussed in Section 3.3

Given the impact that sharp edges and corners have on the SERS enhancement, attempts were made to produce nanowires with sharp edges and corners, like nanocubes. A change in seed particle structure was experimented with to try and force the formation of single crystal nanowires rather than multi-twinned nanowires. While this was partially successful the concentration of cubic nanowires (Figure 48) was not high enough to be used in Raman experiments and no optimisation could be achieved to improve their concentration. Determining the distribution of nanowires in solution based on the TEM images is more difficult than with the nanocubes as the nanowires which much more

tightly packed, leading to a high density of overlapping structures. This made distinguishing between overlapping nanowires complicated and even impeded accurately determining the amount of non-nanowire structures present.

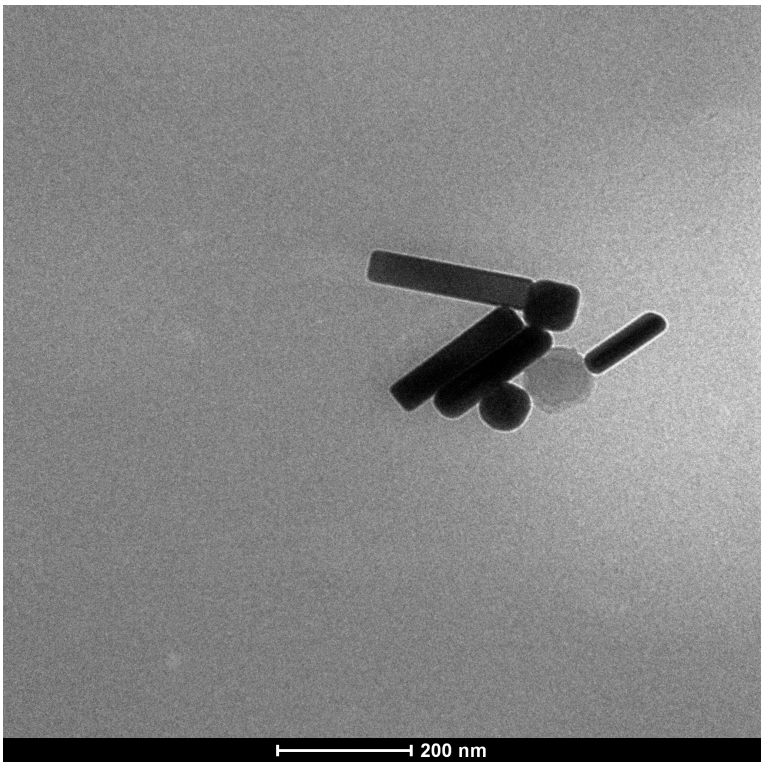

Figure 48: TEM image of cubic based nanorods

5.1.2 UV-visible Spectroscopy

The UV-vis spectra collected for all the nanowires samples (Figure 49) always produced a broad, weak spectrum with no clear peaks. This was unfortunately a known weakness of using UV-vis spectroscopy as a method for characterizing large structures such as nanowires as they contain LSPR peaks well beyond the collection range of UV-vis spectrometers. Also, due to the large variance in nanowire length, the strength of these LSPR will be variable, leading to the peak broadening seen over the entire collection range. It was for these reasons that little information could be gathered from the UV-vis spectrum collected. A slight peak was observed around the 400 nm range, which was probably caused by the small irregular nanostructures and their weaker LSPR peaks, indicating that even after centrifugation there were still some remaining in the nanowire mixture. The most likely cause of the peak broadening observed in Figure 49 is the large length distribution of the nanowires, which leads to each different length generating a new peak with a maxima at different wavelength. These peaks will overlap with one another and result the formation of a single broad peak over the entire wavelength range with no clear peak maxima.

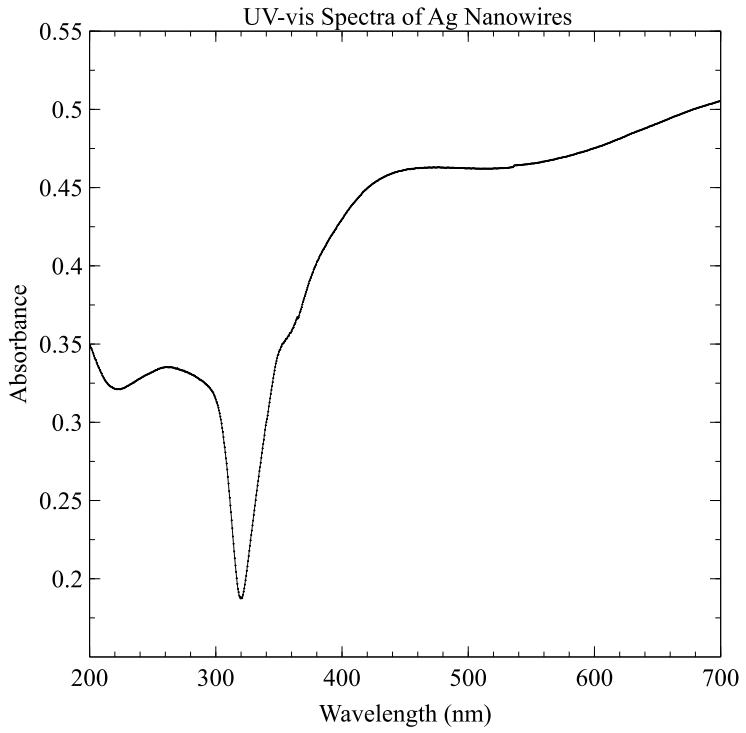

Figure 49: UV-vis spectrum of Ag nanowires collected in water

5.2 Raman Analysis

5.2.1 Surface-enhanced Raman Scattering of R6G

The SERS spectra collected using the R6G adhered to nanowires (Figure 50a) showed similar vibrational mode enhancement to the R6G-bound nanocubes, although most of the modes enhanced appeared to be between 1200-1600 cm^{-1}, with minimal enhancement over the rest of the spectral range. This region between 1200-1600 cm^{-1} is associated with C-C aromatic bending and stretching modes. There appeared to be some spectra that contained strong sharp peaks below 1200 cm^{-1}, but many of these spectra consisted of only peaks in the C-C aromatic range. R6G SERS spectra should contain some peaks below 1200 cm^{-1}, such as C-H bending and stretching modes, but these peaks were not present in most of the nanowire SERS spectra, this is possibly because the nanowires lack the required edge sharpness to enhance these weaker modes to a point where they become noticeable above the noise of the spectra. The high intensity spectra (Figure 50b)

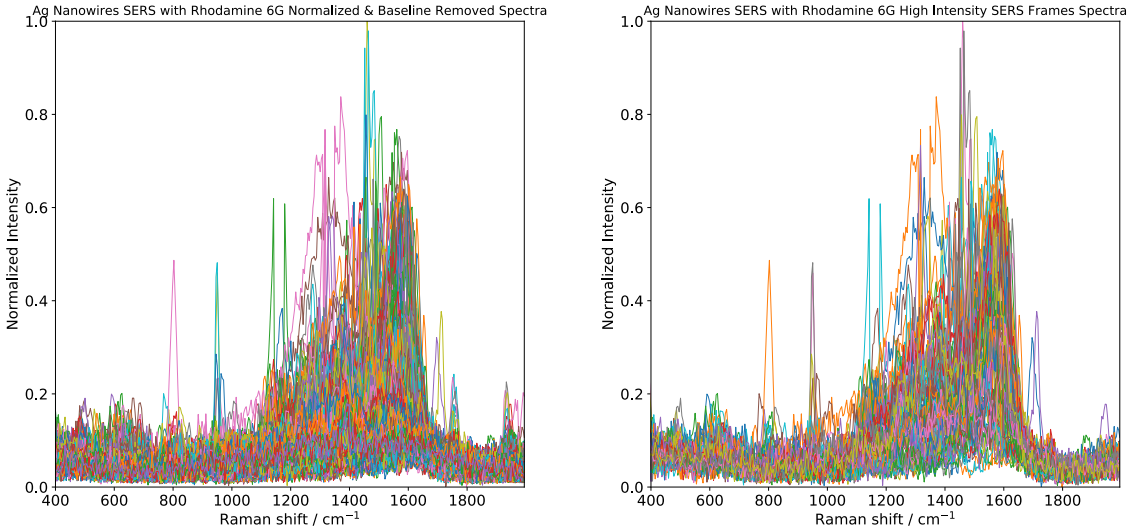

(a) Spectral plot of R6G nanowires SERS spectra made up of 903 spectra

(b) Spectral plot of R6G nanowires high intensity SERS spectra made up of 264 spectra

Figure 50: Spectral plots of Ag nanowire R6G SERS spectra for both normal (a) and high intensity spectra (b).

were isolated and analysed in a similar fashion to the nanocubes to determine if any clustering in the spectra could be observed. There appears to be some evidence of clustering, given the intensity and overlap of peaks around 1600 cm^{-1}, but any clustering was proba-

bly quite weak as there seemed to be minimal consistent peak overlap over the rest of the spectral range. The signal-to-noise ratio of both the initial and high intensity plots are poor, making it difficult to distinguish between the noise of the baseline and the weaker peaks that were expected below 1200 cm^{-1}. It was unlikely that the nanowires were totally incapable of providing enhancement to the weaker peaks below 1200 cm^{-1}, while also providing extensive enhancement to the peaks above 1200 cm^{-1}. These weaker peaks were probably receiving some enhancement but not enough to overcome the baseline noise of the spectra. It was confusing as to why such a large enhancement was observed for the C-C stretching modes, while the C-H bending and stretching modes receive such poor enhancement. A possible explanation was that the lack of sharp edges and corners, resulted in poor LSPR intersections at the corners and edges, lowering the enhancement potential of the nanowires. Given the structure of R6G (Figure 16a) it was expected that even a SERS substrate with a weak enhancement potential would cause the expression of C-C aromatic stretching modes as a large aromatic system makes up most of R6G's structure. The C-H and C-C-C modes are inherently weaker modes and would require a larger enhancement to become visible above the noise.

A possible explanation for the difference in chemical shift and the appearance of unexpected peaks may be the capping agent used to produce the nanowires. Both nanowires and nanocubes were prepared using a PVP as a capping agent which is Raman active and could be the source of this difference in chemical shift and the cause of some unexpected peak appearances. Other factors that could be responsible for the difference in chemical shift and appearance of unexpected peaks was the solvent exposure to molecules adhered to corners and edges becoming solvated and perturbing their electronic structure. This combination of dull corners and edges and solvated molecules adhered to these locations could be the cause of the unexpected peak location and intensity.

Much like the nanocube data, a grid plot of several high intensity R6G nanowire spectra (Figure 51) was produced to better understand what Raman band enhancement may be occurring. There appeared to be some consistent band enhancement patterns occurring within the spectra plotted, with many of the plots sharing similarities, such as plots 4, 5

and 6, and plots 9, 12 and 13. The occurrence of these patterns may be evidence supporting the idea that different regions on the nanostructure produce different SERS signals, as there appears to be several distinctly different SERS spectra present in the grid plot.

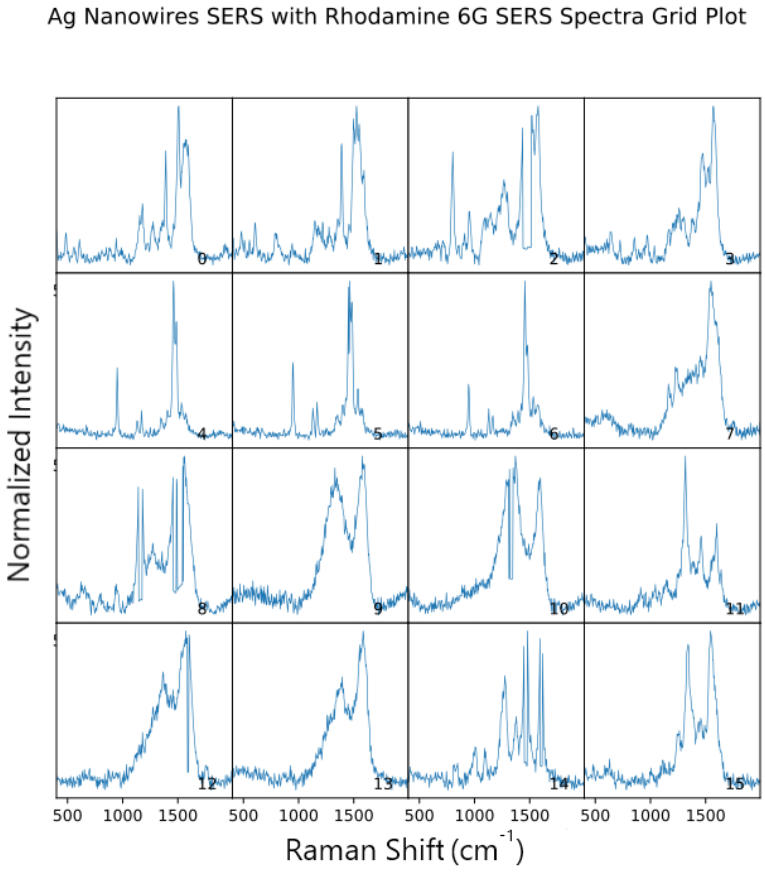

Figure 51: Grid plot of high intensity R6G nanowire spectra

5.2.1.1 Principal Component Analysis Data

The Scree plot (Figure 52) for the nanowire R6G data was dominated by the first PC, which constituted 24% of the total variance of the system, while the subsequent PCs made up progressively less of the total variance. The drop off in variance covered by the later PCs was similar to the trends observed in the R6G nanocube data, with the second PC making up approximately 15% of the total variance and the later PCs covering below 4% of the remaining variance. The high density of the peaks and the lack of many outlier peaks suggested that the large variance coverage of PC1 was reasonable, as the spectral differences between these spectra would be less than those seen in the nanocubes data. This explanation would also account for the rapid decrease in variance coverage by the subsequent PCs, as most spectra contained peaks within a narrow wavenumber range and the lack of outlier peaks would lower the total variance between the spectra. When investigating the

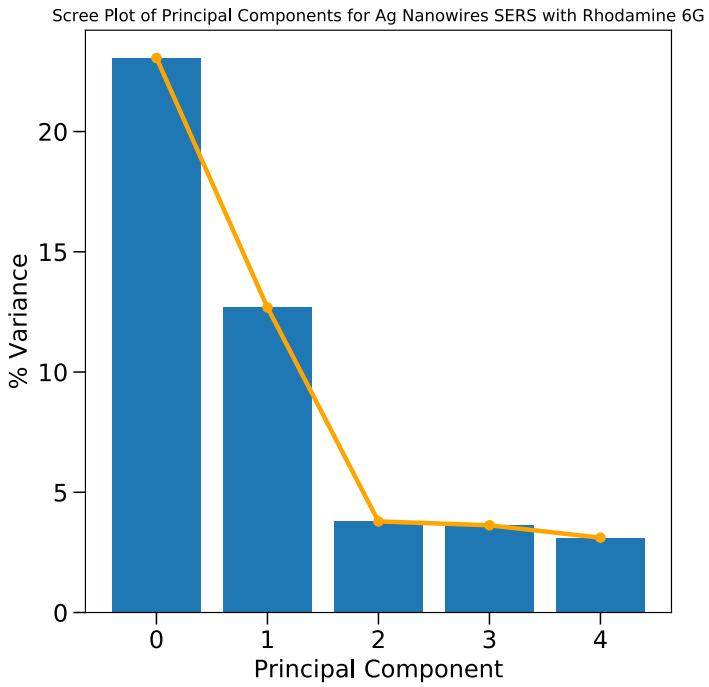

Figure 52: Scree plot of R6G nanowires SERS data

Loadings plot of the R6G nanowire data (Figure 53b), the representation of the first PC showed a region of largest weight between 1200 – 1600 cm^{-1}, while the remaining PCs displayed a range of weighted regions. The Loadings plot for PC5 was interesting as it contained numerous strong sharp peaks across the entire spectral range, rather than the usual smooth baseline of the other Loadings plots. This could be indicative of there be-

ing too many PCs used during the analysis, leading to the later PCs containing minimal weight. The low weight accounted by PC5 shown in the Scree plot supports this explanation although the difference in the weight covered by PC3, PC4 and PC5 was not significant enough to completely validate this idea. This would mean that the appearance of the PC5 Loadings plot were caused by an unknown variable. Comparing the Loadings plot to the average spectra plot (Figure 53b), both appear to share areas of spectral intensity. Outside of this observation, the appearance of both the Loadings and Scree plots were as expected and followed similar trends to the nanocube plots.

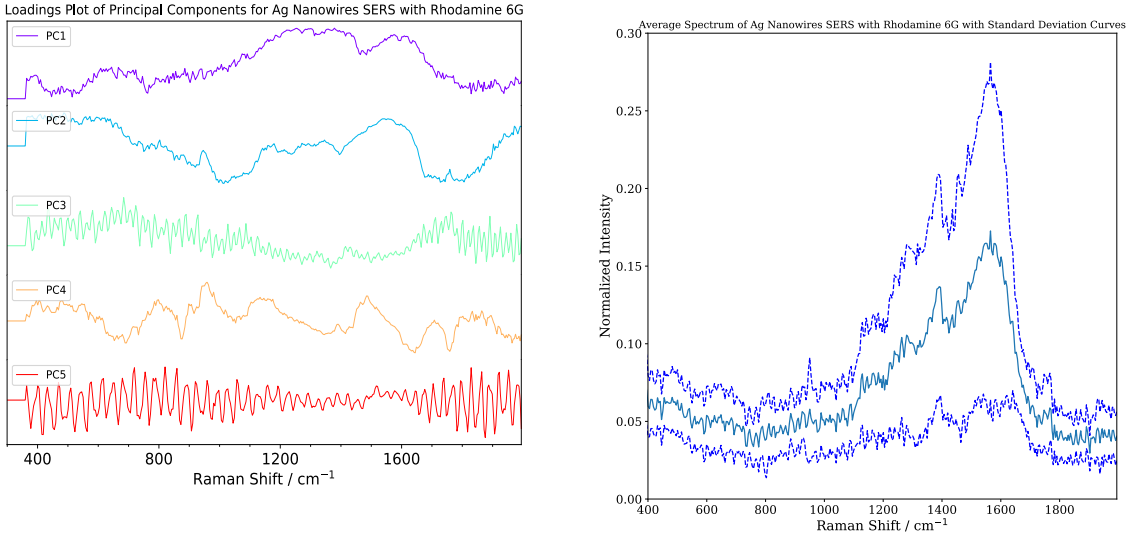

(a) **(b)**

Figure 53: Loadings plot (a) and average spectrum with standard deviation curves (b) for R6G nanowire SERS data.

The primary observation made from the 2D Score's plot array (Figure 54a) was the large spread in the data points over most of the plots, excluding the PC1 vs PC2 plots. This is possibly evidence of this data displaying similar trends to the nanocube data and containing a continuum of different spectra. As there was extensive spread over all the plots, especially over the PC1 plots, it is difficult to determine if any clustering was present in the data using the PCA outputs. Much like the R6G nanocube data, there did seem to be some clustering present in the plots, but the clusters were not consistent over the different plots, making it difficult to identify trends inside the data.

The 3D Score's plot (Figure 54b) provided some insight into the data point clusters observed in the 2D Score's plots for the PC1 and PC2 plots. The data points fit a shape resembling a cone, and the bulk of the data forming a tight string that runs the length of the group, with the remaining data points spreading out from the string. Outside of these observations there did not appear to be any trends in the data, as the remaining data points were sporadically spread across all three axis. The overlapping of data points inside the bulk of the data points was a promising observation, as theoretically the SERS spectra should be identical, but the low number of overlapping occurrences suggested that the experimental data does not fit this idea.

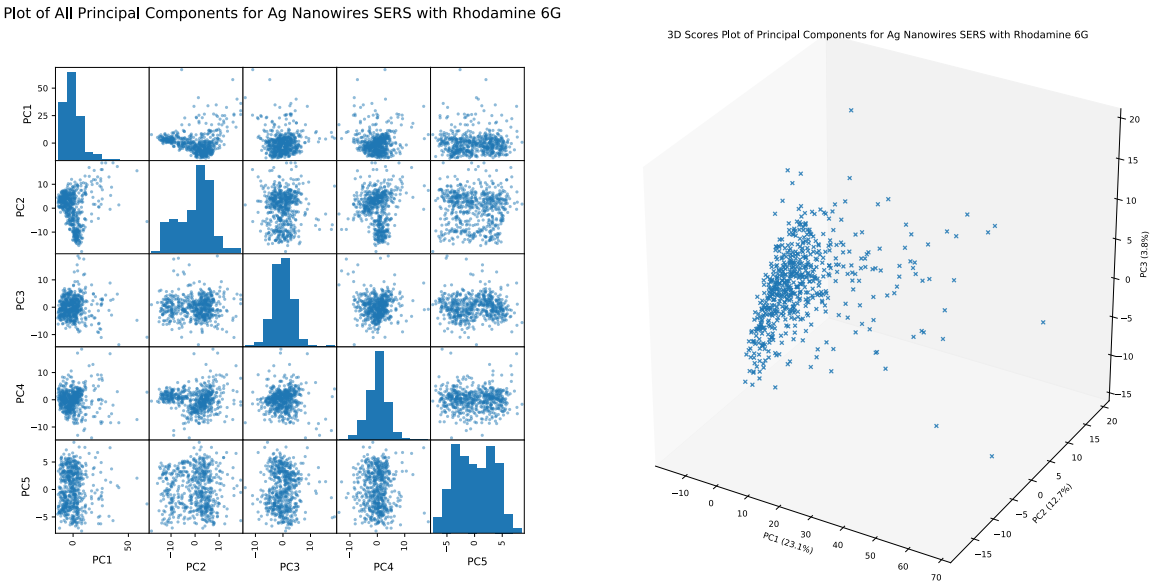

(a) **(b)**

Figure 54: Scores scatter plot (a) and 3D Scores plot (b) for R6G nanowire SERS data.

The experimental data more closely fitted the continuum idea given the connected string of data points, and there was a continuous slight change in spectra from one end of the string to the other. Also the data set did not fit the clustering idea, as multiple discrete clusters were not present in either of the outputs, as would be expected for a data set fitting this idea. Much like the other data sets, the primary data point cluster was surrounded by several outlier peaks that span the entire plot, across all three axis.

The outlier spectra for the R6G nanowire data displayed weak broad enhancement between approximately 1250 cm^{-1} and 1700 cm^{-1}. There did not appear to be any semblance

of patterns inside the outlier spectra. All of the outlier spectra were identified using the same methodology as the nanocube data, with the outlier spectra being linked with the outlier data points of the Score's plots (Figures 54a and 55b). Comparing these outlier plots to the spectra to those displayed in the high intensity grid plot (Figure 51) it appears that the PCA was successful in separating and isolating the spectra, as the outlier spectra appear to share very little similarities with those shown in Figure 51. Comparing these outlier spectra with those displayed in the Euclidean distance map for this data set(Figure 56) with large distance values, it appeared that there was some correlation. Some of the outlier spectra displayed in Figure 55a did appear to have large distance values, spectra 96 and 215, while the remaining spectra (282, 286, 285, and 321), all of which were the largest outlying spectra, appeared to have distance values below 1. This is possibly more evidence that PCA and Euclidean distance mapping do not separate the spectra in similar manner, making it difficult to determine which spectra are distinctly different from others.

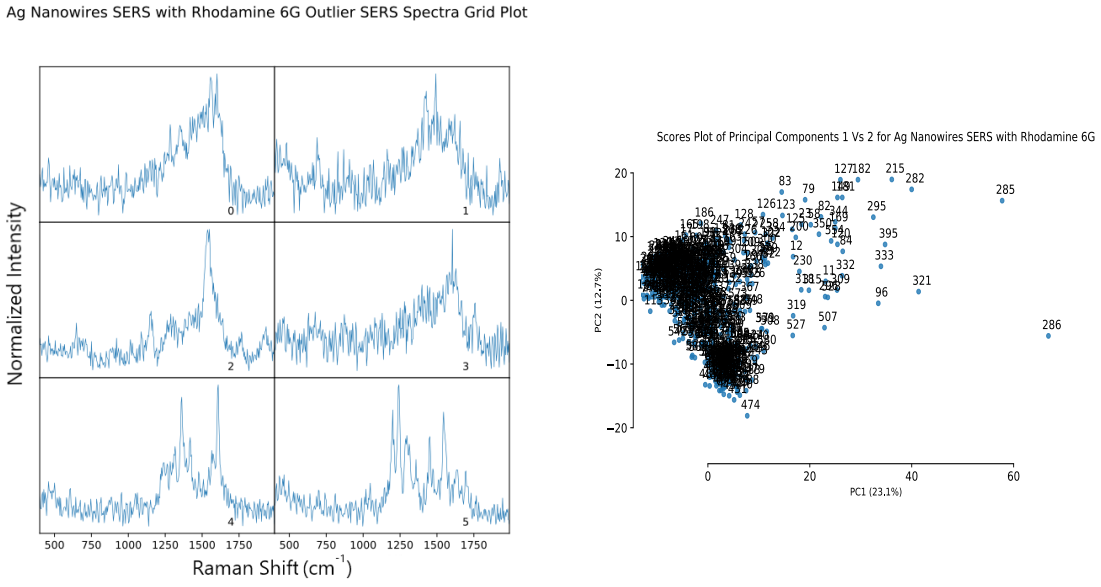

(a) **(b)**

Figure 55: Spectral grid plot of outlier spectra (a) and Scores plot of PC1 and PC2 (b) for R6G nanowire SERS data

5.2.1.2 Clustering Data

The disparity of the data observed in the PCA results were also observed in the clustering technique results, with the Euclidean distance map (Figure 56) showing a number of spectra with a distance above 2, and a cluster of spectra above 4. Most spectra appear to have distance values below 2, which was expected as the Score's plots indicated that most of the data points were inside the cluster and the string. The spectra with a distance value above 4 were probably related to the outlier peaks observed in the Score's plots. When re-

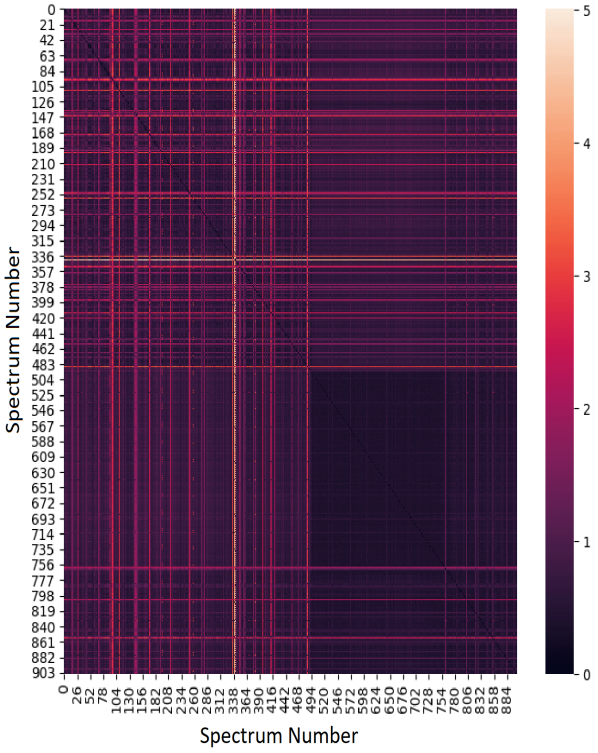

Figure 56: Euclidean distance map of R6G nanowires SERS data

viewing the PCA and clustering results with respect to the appearance of raw spectra, the lack of outlier peaks observed in the raw spectra appeared to correctly represent the analysis output, as the Score's plot contains very clear outlier data points at the extremes of the axes and the Euclidean distance map contained several spectra with a distance above 4.

The self-organising map (Figure 57) contained a group of yellow nodes with a larger distance difference to the neighbouring nodes, which could correlate to the outlier peaks, given their difference to the main cluster of spectra. The blue and green nodes, that correspond to groups of spectra with a distance value below 1.5, make up the largest portion of

the map and, given their low distance values, probably relate to the spectra that make up the cluster and string observed in the Score's plots. These observations appear to fit with the results of the Euclidean distance map and Score's plot, as the main grouping and outlier peaks seem to be correctly represented in all three outputs. The spread of the greenish blue nodes across the left-hand side of the self-organizing map possibly represents the spread in the main group and the string of data points observed in the 3D Score's plot, as they should contain progressively different spectra across a large amount of spectra.

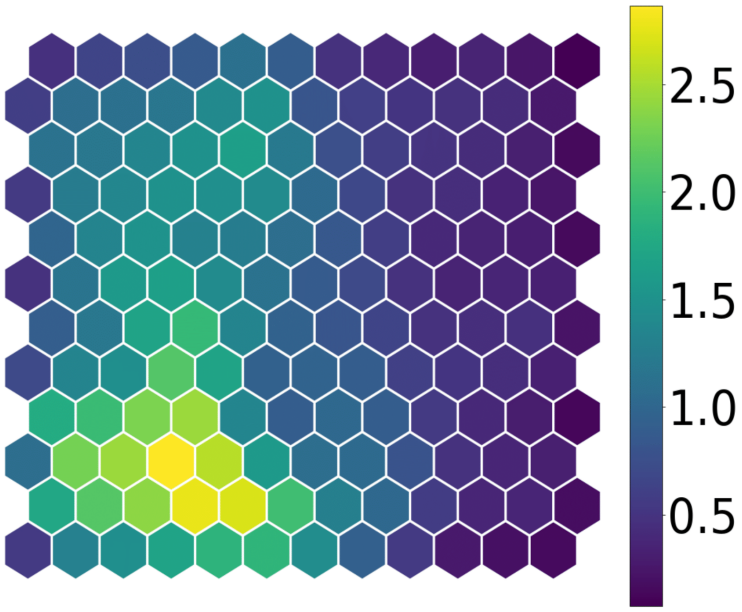

Figure 57: Self-organizing map of R6G nanowires SERS data

5.2.2 Surface-enhanced Raman Scattering of CV

The CV SERS spectra (Figure 58a) collected using the nanowires substrate were consistent with both the literature and the nanocube CV SERS. The initial spectral plot displayed two regions of high peak intensity, one at 800 cm^{-1} and another between 1100 cm^{-1} and 1600 cm^{-1}. The high peak intensity in these regions fits with the theoretical peak location of CV's vibrational modes. The peaks at 800 cm^{-1} have been related to the C-H bending vibrational mode, while the peaks between 1100-1600 cm^{-1} probably correspond to the aromatic C-C bending and stretching vibrational modes, although it was difficult to identify specific modes given the density of peaks in these regions. An expected band that was not expressed as intensely was the C-N bending vibrational mode that should be at 914 cm^{-1}. Some spectra do contain a mode at this wavenumber, but the majority do not. Research has found that the C-N band shifts from 423 cm^{-1} to 214 cm^{-1} due to the decrease in bond length as the nitrogen atom is involved in the coordination of molecule to the Ag surface ([88]). The peaks at 900 cm^{-1} are often associated with the aromatic ring skeletal vibrations, but it was unusual that they are not being expressed as intensely as the other vibrational modes associated with the aromatic ring. This mode may be inherently weaker than the other aromatic modes and could be getting suppressed by the more intense peaks, leading to the skeletal peaks being lost in the baseline noise. Much like the previous nanostructures the same vibrational frequency shifts may be occurring, with solvation of edge and corner molecules being the primary cause of the changes in vibrational frequency. The high intensity spectral plot (Figure 58b) allowed for the identification of the peaks that were being enhanced within the 1100-1600 cm^{-1} region, as the removal of the lower intensity spectra improved the signal-to-noise in these regions. Unlike the peaks at 800 cm^{-1} there did not appear to be much consistency in which peaks were enhanced between 1100 cm^{-1} and 1600 cm^{-1}. There was a high peak density at 1650 cm^{-1} which appeared to be only one side of several overlapping peaks, as the same peak density was not present on the opposite side. The sharp narrow peak distribution at 1170 cm^{-1} was similarly intense in both the initial and high intensity spectral plots, indicating that a proportion of the spectra contained a peak at this position. These peaks were associated with C-H bending vibrations and was expected to be present in all SERS spec-

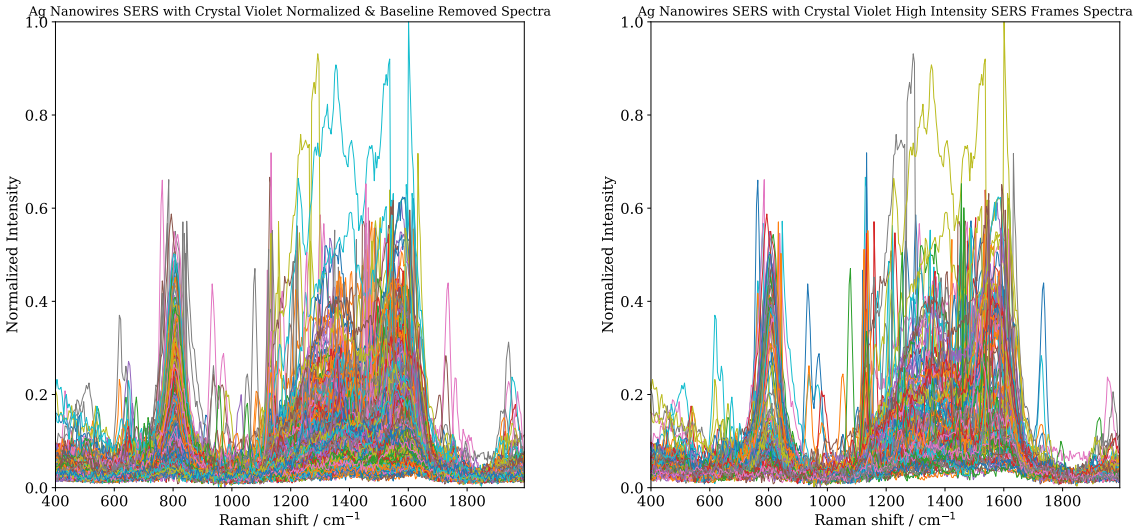

(a) Spectral plot of CV nanowires SERS spectra made up of 790 spectra

(b) Spectral plot of CV nanowires high intensity SERS spectra made up of 344 spectra

Figure 58: Spectral plots of Ag nanowire CV SERS spectra for both normal (a) and high intensity spectra (b).

tra, given the large number of C-H bonds inside the molecule. This C-H bending mode contained two peaks, one at 800 cm^{-1} and another at 1170 cm^{-1}, so it was possible that the 1170 cm^{-1} peaks was the weaker of the two bands and was only expressed sporadically and with less consistency than the 800 cm^{-1} peak, which seemed to occur with a much higher frequency.

Much like the nanocube and previous nanowire data set, the grid plot of the high intensity spectra for the CV nanowire data (Figure 59) appeared to show some spectra that shared similar band enhancement and intensity, plots 0 and 1 and plots 11 and 12, with the remaining plots displayed spectra containing a larger distribution of peak enhancement and intensity. Excluding plots 0-2, the plots appeared to contain either one or two strongly enhancement peaks over a narrow Raman shift, with minimal peak enhancement over the remaining spectral range. It was difficult to determine what conclusions could be made from these spectra, as there did not seem to be any clear trends or patterns inside between them.

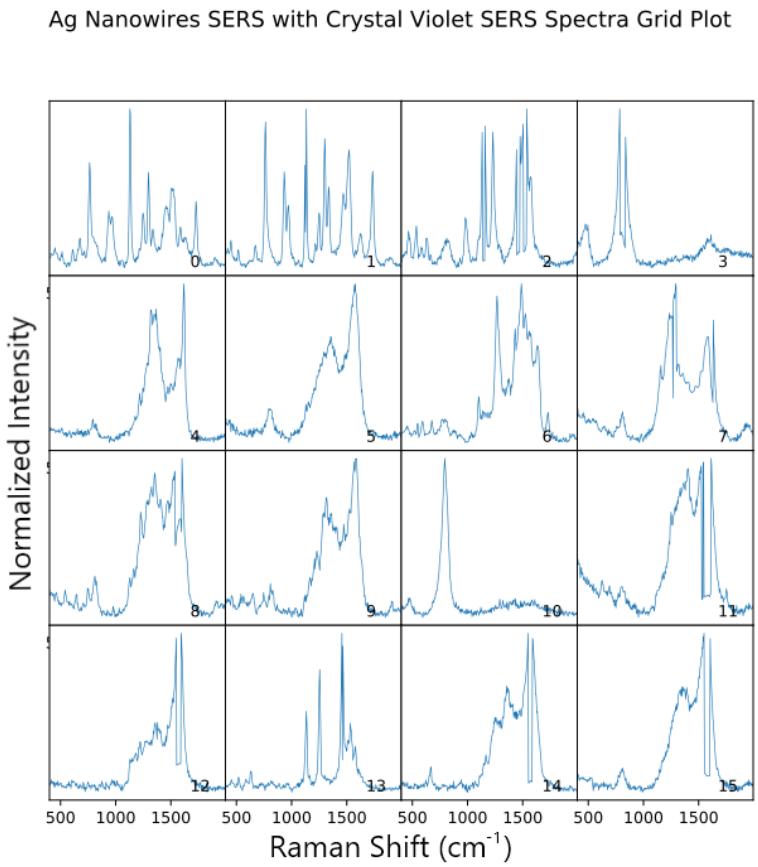

Figure 59: Grid plot of high intensity CV nanowire spectra

5.2.2.1 Principal Component Analysis Data

The Scree plot (Figures 60) fit the trends established in the nanocube and R6G nanowire data, with the first PC containing a significant portion of the total variance while the remaining PCs covered progressively less. When comparing this Scree plot to previous plots, the percentage variance being covered by the first PC was higher than that of the previous plots, with approximately 29% of the total variance being covered. The variance drop-off in the remaining PCs is nearly identical to the previous datasets, with the second PC covering between 10-15% and the remaining three PCs covering approximately 5% each. The large variance coverage achieved by PC1 probably means that a significant portion of the data was spectrally similar and can be effectively covered by a single PC. This degree of coverage could correspond to a large cluster of peaks in the Score's plot, while the coverage of PC2 possibly indicates the presence of either a secondary cluster or other pattern inside the Score's plot. The coverage provided by PC1, which was more than any other PC in this entire study, implied an increased uniformity in the spectra when

analysing the nanowires, as a greater portion of the total spectra are being represented by the PC. The Loadings plot (Figure 61a) for PC1 looked very similar to the average spectra

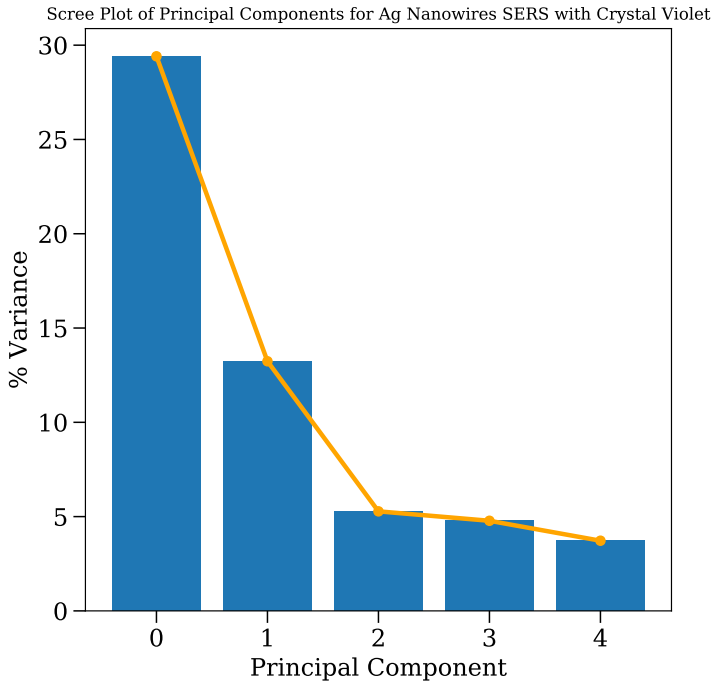

Figure 60: Scree plot of CV nanowires SERS data

of the CV data (Figure 61b), with highly weighted regions at 600 cm^{-1} and a broad region between 1100 cm^{-1} and 1600 cm^{-1}. PC1 also appeared to have low weight at the 800 cm^{-1} region, which should be a highly weighted region based on the spectral plots. PC2 looked to be composed primarily of highly weighted areas at 500 cm^{-1}, 800 cm^{-1} and 1700 cm^{-1}. The appearance of the PC1 and PC2's Loadings plots, suggested that during the PCA process the variance at 800 cm^{-1} and the variance between 1100-1600 cm^{-1} were split into separate PCs to maximise the total variance over the number of PCs available. The plots of the remaining PCs consisted of highly weighted regions over numerous wavenumber ranges, that accounted for the remaining peaks present in the spectral plots. The Score's plot array (Figure 62a) results were consistent with the predictions made from the Scree and Loading's plots, as the plots produced using PC1 and PC2 displayed a single large cluster of data points neighbouring each other, with some separation inside the cluster that could mean that the cluster was made up of multiple smaller clusters. Excluding these plots, the major trend observed in the remaining plots was a single large cluster of data points, surrounded by outlier data points. This observation was prevalent over

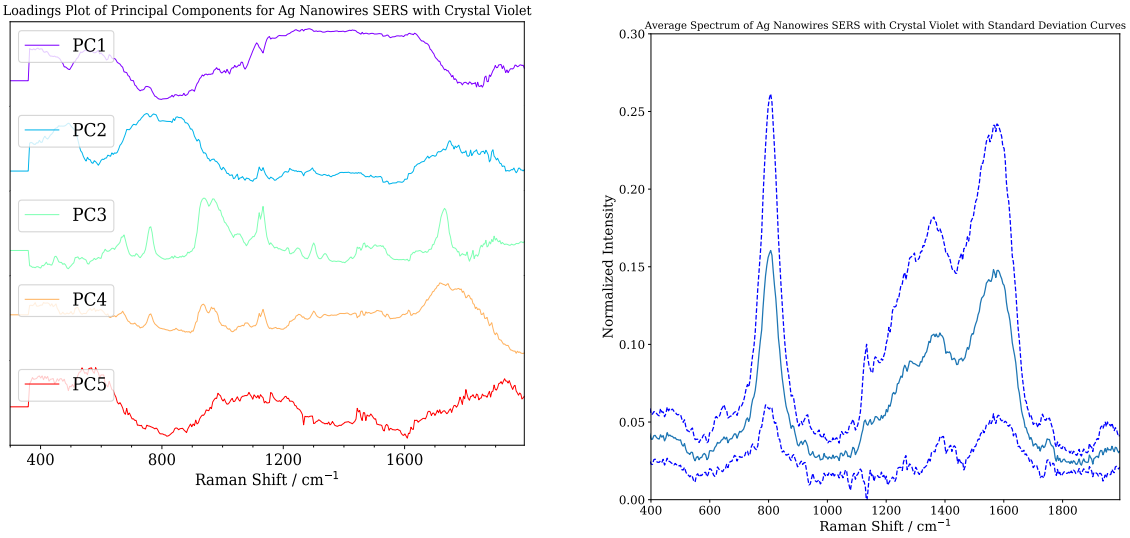

(a) **(b)**

Figure 61: Loadings plot (a) and average spectrum with standard deviation curves (b) for CV nanowire SERS data

the other data sets investigated using the other nanostructures. The cluster observed in the PC1 vs PC2 Score's plots appeared to consist of two areas of large data point density neighbouring each other. Surrounding both clusters were outlier data points that did not conform to either of the clusters. The separation inside the cluster was less apparent than the previous data sets as there was a large amount of overlap that was difficult to interpret given the 2D nature of this plot. As the plot is only 2D the data points at the intersection between clusters may be further from the clusters than originally thought. The outlier data points were probably representative of the outlier spectra observed in the spectral plots, given their significant difference compared to the rest of the data. The 3D Score's plot (Figure 62b) provided greater insight into the possible clustering observed in the 2D Score's plot, showing that there was some weak separation in the data points. Unfortunately, both suspected clusters had high overlap, making it difficult to isolate their shape. The clusters appeared to contain strings of data points that neighbour each other. This could be indicative of the continuum idea, as these strings of data points showed that the spectra contained progressively minor differences from one end of the string to the other, while still containing enough similar spectral data to be grouped together by PCA. The separation between the suspected clusters was not clear enough to form any conclusions into which idea, if any, were responsible for the appearance of the Score's

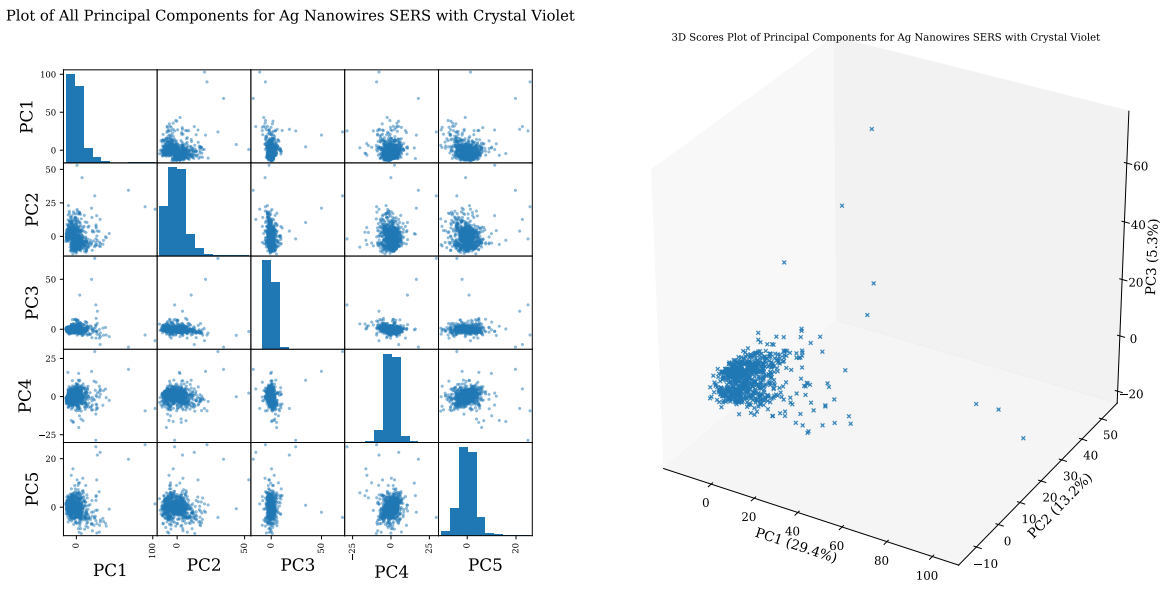

(a) **(b)**

Figure 62: Scores scatter plot (a) and 3D Scores plot (b) of CV nanowire SERS data

plot output.

The outlier grid plot of the CV nanowire data (Figure 63a) shared similarities to the R6G nanowire data, with many of the spectra displaying broad enhancement over large regions of the spectra and no patterns between the plots. All of the outlier spectra displayed in this plot were far spread, from both themselves and other spectra, in both the Score's plots (Figures 62a and 63b), possibly indicating that the PCA deemed them to be distinctly different from one another and the rest of the spectra collected. The Euclidean distance values correlated to these outlier spectra did not appear to share these level of separation, as none of the PCA outlier spectra had a distance value above 3. These spectra were 77, 256, 327, 588, 589 and 619. This observation matched the observations made about the R6G nanowire data, with the majority of those outlier spectra having surprisingly low distance values for how separated they were inside the Score's plots. The spectrum with the largest distance value in the CV nanowire data, spectrum 650 with a value of approximately 7, appeared in the large cluster of spectra in all PCA outputs, and as a result was not considered an outlier.

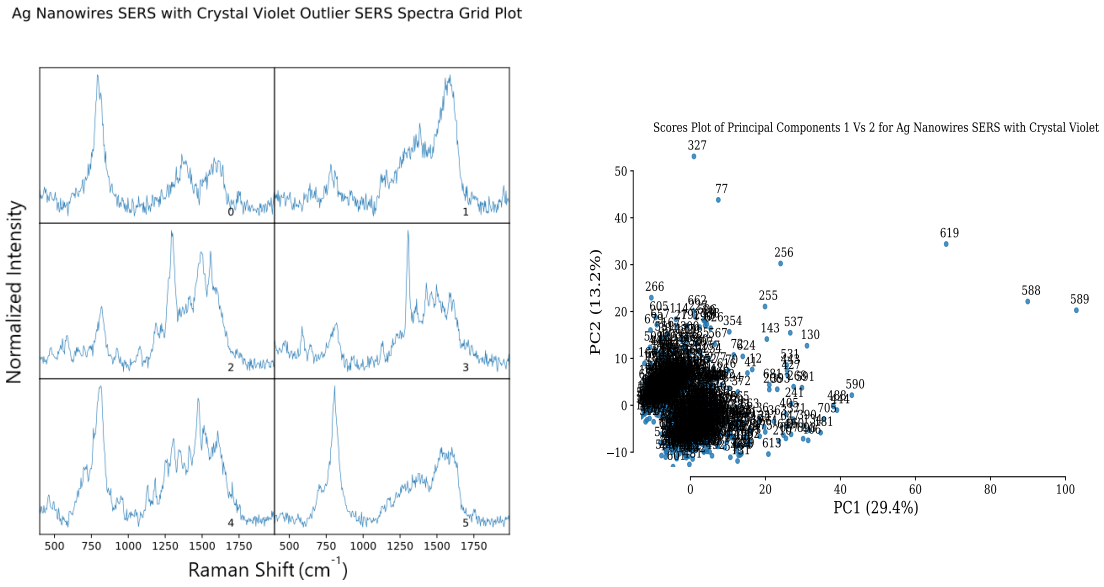

(a) **(b)**

Figure 63: Spectral grid plot of outlier spectra (a) and Scores plot of PC1 and PC2 (b) for CV nanowire SERS data

5.2.2.2 Clustering Data

The quality of information provided by the Euclidean distance map (Figure 64) of this data set was relatively weak, as many of the spectra were similar enough to not produce a large distance difference in the distance plot. There was only a small portion of spectra with a distance value of 5 and 7, and these were possibly the outlier peaks observed in both the spectral plots and the Score's plots. This observation simply provides more evidence towards the confirmation that a small portion of the total spectra are outliers. The Euclidean distance map does allow for the identification of which spectra are outliers, but because only a small portion of the spectra are outliers, their impact on the analysis was minimal. A secondary observation was the remaining spectra appeared to be split into spectra with a distance above 3 and spectra with a distance below 1. It is possible that this separation in the data was evidence of the clustering observed in the Score's plots, as one cluster of data points should be spectrally different to the other cluster, resulting in a distance difference between in the spectra that make the clusters. Like in the Euclidean distance map, the outlier spectra are likely being displayed in the self-organising map

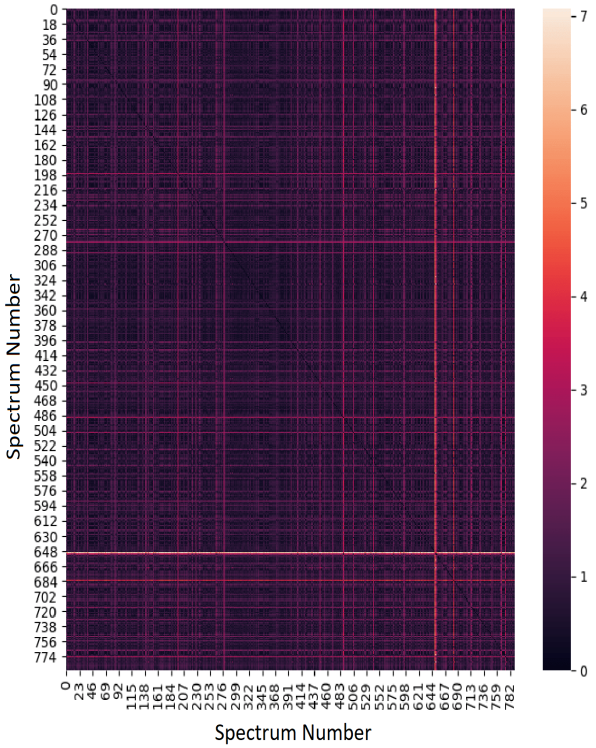

Figure 64: Euclidean distance map of CV nanowires SERS data

via the 3 high distance nodes, coloured yellow and light green, as they have the largest distance difference compared to the other nodes. This trend was common in all the data sets and made sense as the outlier spectra should have a larger distance difference than the other spectra. The green nodes neighbouring the central yellow node were difficult to identify, as they should theoretically correlate to data points inside one of the clusters, but the spread of the green nodes was counter to this theory. In contrast to this, the blue nodes should correlate to the data points inside the other cluster. The spread in both the green and blue nodes could be indicative of the strings of data points observed in the 3D Score's plots. The green nodes were connected and appeared to fit the string of data points idea, but it was difficult to draw definitive conclusions using just this plot. The overall distance difference was only marginal considering the largest difference is only 3, which in comparison to other plots with a difference of 6-7, was relatively low.

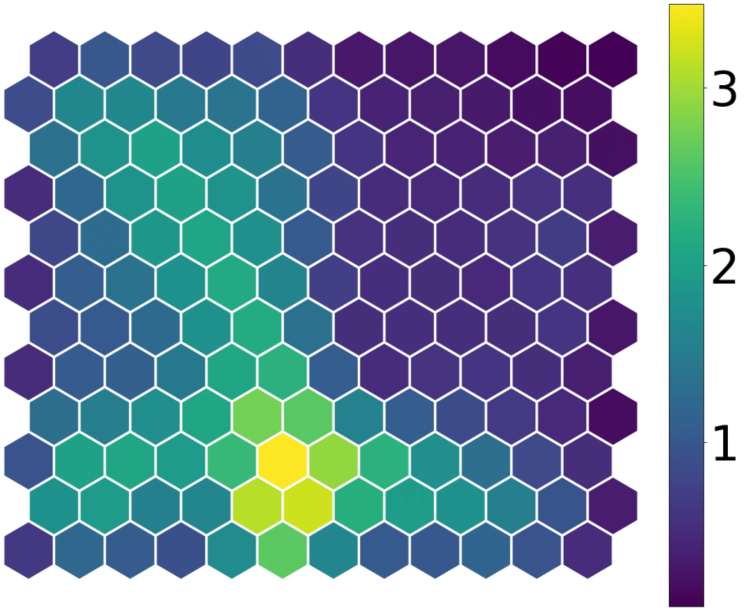

Figure 65: Self-organizing map of CV nanowires SERS data

5.3 Summary

The data collected of both R6G and CV adhered nanowires did not provide the same level of insight into the patterns and trends present in the SERS spectra as obtained for the nanocubes. The R6G data displayed no clear signs of discrete clustering, with the clustering outputs showing a single, large, widespread cluster of data points, and no obvious trends or patterns were present. The amount of vibrational mode enhancement provided by the nanowires for R6G was notably worse than the nanocubes, as several of the lower wavenumber modes were not expressed to the same extent as the nanocubes, or even expressed at all. The CV data was more promising, as the nanowires managed to produce similar enhancement to the nanocubes, with a more tightly packed cluster of data points being observed in the clustering outputs. Some evidence of multiple clustering occurring inside the CV data was observed, but the clustering theory will require more evidence before being validated. It is possible that the physical structure of the nanowires was the cause of the poor enhancement quality, as the low concentration of sharp edges and corners should diminish the enhancement quality they provide. The edge and corner sharpness of the nanowires were inconsistent and worse than the nanocubes, which in combination with the large crystal face surface area, was probably the reason behind the poor enhancement of the weaker vibrational modes in the R6G spectra. Improvements

could be made to the quality and uniformity of the nanowires, which in turn should improve the SERS spectra produced using them, but more time would be required to achieve this. If it were possible to produce the cubic nanowires with higher uniformity then theoretically the SERS enhancement provided should be greatly improved, as the sharp edges and corners should enable the enhancement of the weaker vibrational modes of both dye molecules.

CHAPTER 6

Nanoplates

6.1 Synthesis and Characterisation

Of the three nanostructures produced, the nanoplates were the easiest structure to produce, as a documented method of synthesis was replicated with only minor changes required to produce nanoplates similar to those shown in literature. In terms of optimizing the production of nanoplates, very little changes were required to maximise the yield and quality of nanoplates produced. During testing it was discovered that there were two pivotal steps during nanoplate synthesis, the first being in the growth of seed particles and the second being the temperature control during nanoplate growth. During the synthesis of seed particles if the reagents were not carefully prepared and precisely introduced into the reaction vessel, then the seed particles produced will form over a larger size and shape distribution, which in turn will lead to more irregular nanoplates. Additionally, during the nanoplate growth portion of the reaction, if the reaction temperature exceeded 5°C than the reaction kinetics will increase and nanoplates will begin to form rapidly, leading to increased growth on all crystal facets and resulting in irregular nanostructures forming. No major changes to the literature method were made and the method appeared to be easily reproducible, as the reaction was repeated several times with consistent results.

6.1.1 Transmission Electron Microscopy

The TEM images (Figure 66) collected of the nanoplate samples showed an abundance of plate like structures, with minimal irregular structures. The quality of the nanoplates appeared to vary slightly in edge and corner sharpness, while the size and shape of the

nanoplates was consistent, with an average edge length of 100 nm. Truncation of the corners was observed, which was possibly caused by slight variations in the etching agent concentration or the reaction kinetics. The nanoplate reaction was temperature dependent, so a slight change in the reaction temperature will also impact the growth of the nanoplates, as the reaction kinetics will increase with temperature resulting in nanostructures forming faster and with less control over their size and shape. Some other physical properties of the nanoplates were also observed including the thinness of the nanoplates, the folding and overlapping of nanoplates and the structure of the seed particles used in the synthesis of nanoplates. The thinness of the nanoplates was discussed in the literature where they estimated an approximate depth of 6 nm. The TEM used in this project did not have the resolution required to accurately measure the thinness of the nanoplates synthesised, but the thinness of the nanoplates could still be observed and used to compare with the other nanostructures. The overlap of nanoplates shown in Figure (66c) gave the best example of how thin the nanoplates are, as it was easy to see the outline of one plate underneath another. The TEM relies on an electron beam to generate images, making it difficult to determine the depth of metallics structures as they dissipate the electrons as their depth increases. The contrast seen on the face of the nanoplates could be indicative of a slight variation in thinness or a more probable reason is the trapping of solvent under the nanoplates. An unexpected consequence of the thin nature of the nanoplates was their apparent flexibility and their ability to fold onto themselves, without any noticeable damage to the plate. This could have unexpected results on the SERS data collected using the folded nanoplates, if it were possible to produce a sample of folded nanoplates. It is currently unclear whether this folding process can be controlled or how it was caused, so it is unlikely to be possible to investigate the SERS enhancement of folded nanoplates. This folding could introduce an addition surface plasmon resonance junction, that may cause a change in both the Raman enhancement and the position of the LSPR seen in its UV-vis spectrum.

The TEM images collected of the nanoplate seed particles show a much greater dispersity in both the size and shape of structures present. Some plate-like structures are clearly visible in the seed particle TEM images along with smaller, spherical irregular structures.

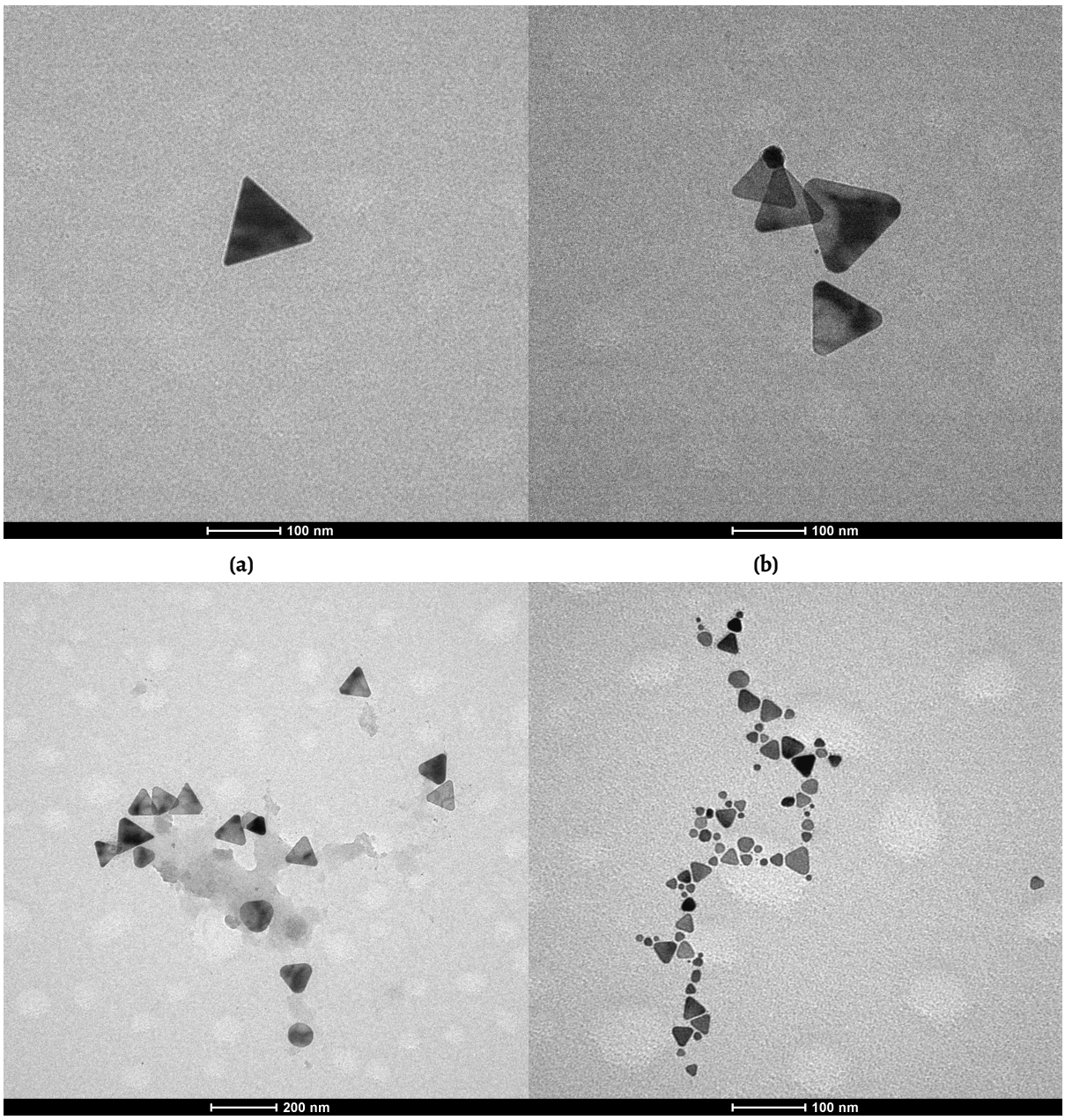

Figure 66: TEM images of triangular Ag nanoplate synthesised using the citrate reduction method discussed in Section 3.4

Many of these irregular structures are removed via oxidative etching, but some remain in solution and grow during the growth step of the nanoplate synthesis, leading to larger irregular structures seen in Figure 66d. These irregular structures are of low enough concentration to not impact the SERS enhancement quality. Like nanocubes, the removal of these irregular structures would be difficult, if not impossible, due to the similarities in size and shape impacting the effectiveness of using separation techniques such as centrifugation or filtering. If more time were available or it was deemed essential, the method of synthesis for the nanoplates could be optimised to lower the concentra-

tion of irregular structures further. As the growth of the structures was dictated by the initial structure of the seed structures, the first step in optimising the reaction would be to minimise the concentration of irregular seed structures and establish stricter control over the reaction kinetics during the growth stage of the nanoplate reaction to minimise unwanted rapid growth.

6.1.2 UV-visible Spectroscopy

The UV-vis spectrum collected of the Ag nanoplates (Figure 67) contains a strong, sharp peak at the 400 nm range with a secondary weaker broad peak at the 500 nm range. The peak at 400 nm was assumed to be the LSPR peak from the nanoplates, as their surface plasmons will be comparable in size to the nanocubes, leading them to absorb at a similar wavelength. The strength and sharpness of this peak was indicative of the high monodispersity of the nanoplates, showing that there was minimal variance in the nanoplate's size and shape. The secondary peak at 500 nm was probably caused by larger nanoplates and other nanostructures, as the broadness of the peak indicated a higher dispersity of structures, while the longer wavelength indicated a larger LSPR was responsible for the peak.

Based on the TEM collected it was possible that this peak was caused by larger plate-like structures that have probably undergone some folding or other changes to their structure. The nanoplates have several surface plasmon resonance junctions at both the edges and corners, where the surface plasmons on the top and bottom faces meet. The ratio of edges to faces was comparable to nanocubes, although given the somewhat two-dimensional nature of the nanoplates, the corner plasmon junctions are made up of two plasmons rather than three plasmons for the nanocubes.

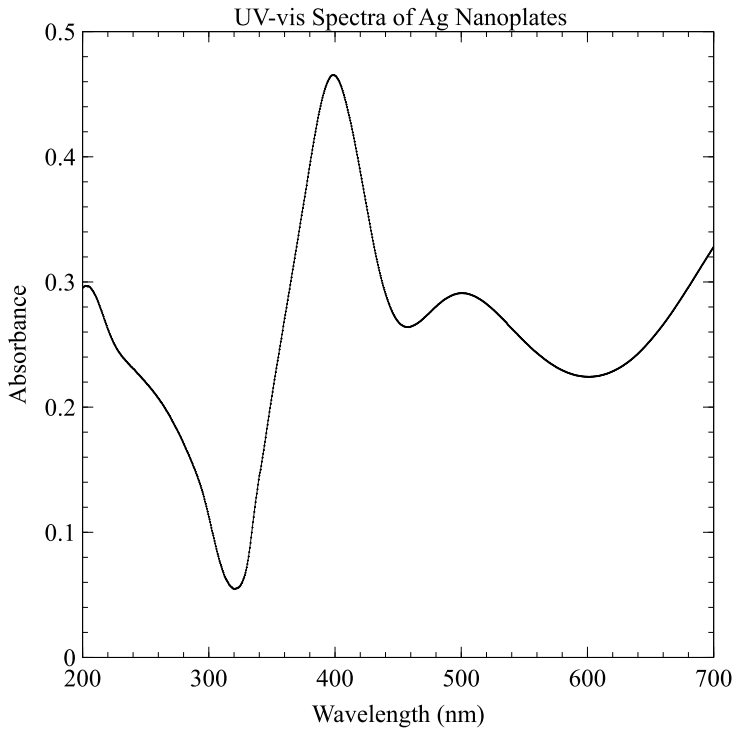

Figure 67: UV-visible spectrum of Ag nanoplates collected in water

6.2 Raman Analysis

6.2.1 Surface-enhanced Raman Scattering of R6G

The first observation of the SERS spectra of R6G adhered to the nanoplates (Figure 68a) was the abundance of SERS peaks over the entire spectral range that all have very similar normalized intensities. Given the low density of these peaks they appeared to stem from single spectrum, making it difficult to discern much from the information they provide, as they were only present for one spectrum out of the several thousand collected. Fortunately, only the peaks above 1700 cm^{-1} were unexpected peaks, as the remaining peaks occurring in or around the wavenumber regions where SERS excitation was expected for R6G, so the peaks above 1700 cm^{-1} can be considered outlier peaks, likely stemming from contaminants present during SERS signal collection. When reviewing the other trends present in the spectra, the regions of peak density are clearly seen above the baseline noise of the spectra, with high peak density at 600 cm^{-1}, 800 cm^{-1}, 1150 cm^{-1}, 1400 cm^{-1}, 1500 cm^{-1} and 1650 cm^{-1}, all of which are expected for R6G SERS signals. Apart from the extreme enhancement of the peak at the 800 cm^{-1}, the remaining SERS peaks appear to have undergone a consistent degree of enhancement. This could have been possibly

caused by both the high degree of uniformity of the nanoplates and the low concentration of irregular secondary structures, which were both higher and lower respectively than those observed in the nanocube and nanowire analysis.

Surprisingly, the high intensity spectral plot (Figure 68b) did not provide any additional insight in the trends in the data over the initial spectral plot. A possible reason for this was the signal-to-noise ratio of the initial spectral plot was not large enough to discern a significant amount of information. With the decrease in spectra that makes up the high intensity plot, the trends observed in the initial spectral plot became harder to see. The most useful trend for understanding what was occurring inside the data was the strong baseline peak regions that clearly show which wavenumber regions are most readily expressed. The aromatic C-C stretching modes at 1364 cm^{-1}, 1512 cm^{-1}, 1576 cm^{-1} and 1652 cm^{-1} are all present and readily expressed, along with the in-phase C-O-C and C-H bending at 1312 cm^{-1} and 1183 cm^{-1} and the C-H and C-C-C out-of-phase bending at 779 cm^{-1} and 614 cm^{-1} respectively. This was possibly indicating the degree and quality of SERS enhancement that the nanoplates provide.

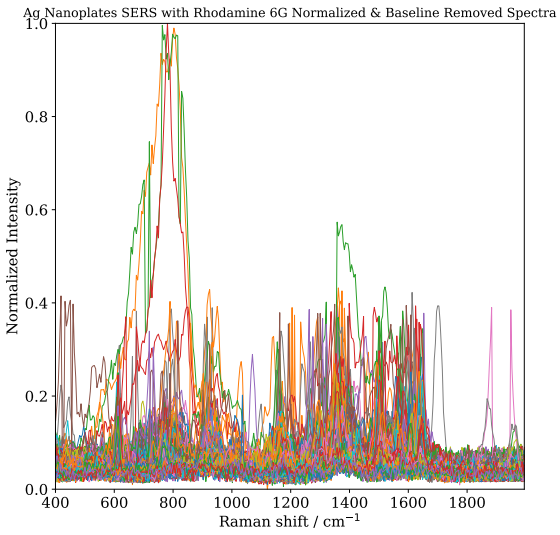

(a) Spectral plot of R6G nanoplates SERS spectra made up of 734 spectra

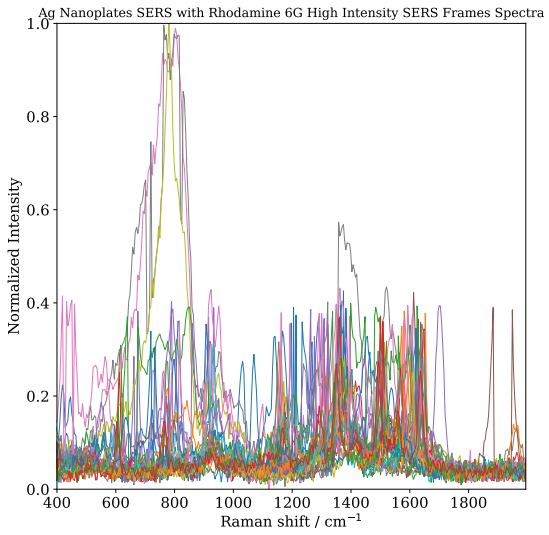

(b) High intensity spectral plot of R6G nanoplates SERS Spectra made up of 168 spectra

Figure 68: Spectral plots of Ag nanoplates R6G SERS spectra for both normal (a) and high intensity spectra (b).

Excluding the extremely strong peaks at 800 cm^{-1} and 1400 cm^{-1}, the SERS peaks were surprisingly consistent in both intensity and peak shape. Most of the peaks were sharp,

narrow, and had a normalized intensity of approximately 0.4 intensity. Comparing these results to the Raman data collected with the other nanostructures, this uniformity in peak shape and intensity was only seen in the nanoplate SERS data.

The high intensity spectra, plotted in the grid plot (Figure 69), followed the trends from the previous nanostructure data sets, with some of the spectra sharing similarities in peak enhancement, location and intensity. Many of the spectra shared these similarities, with plots 0-2 sharing being the most similar, with the remaining spectra being made up of a distribution of peak enhancement and intensity. Several plots, 4, 5, 6 and 14, appeared to only contain a single strongly enhanced peak, often neighbouring a weak, broad secondary peak. These plots were the most dissimilar from the other plots. There did not seem to be any other clear patterns or trends, which made it difficult to draw any further conclusions from the spectra displayed.

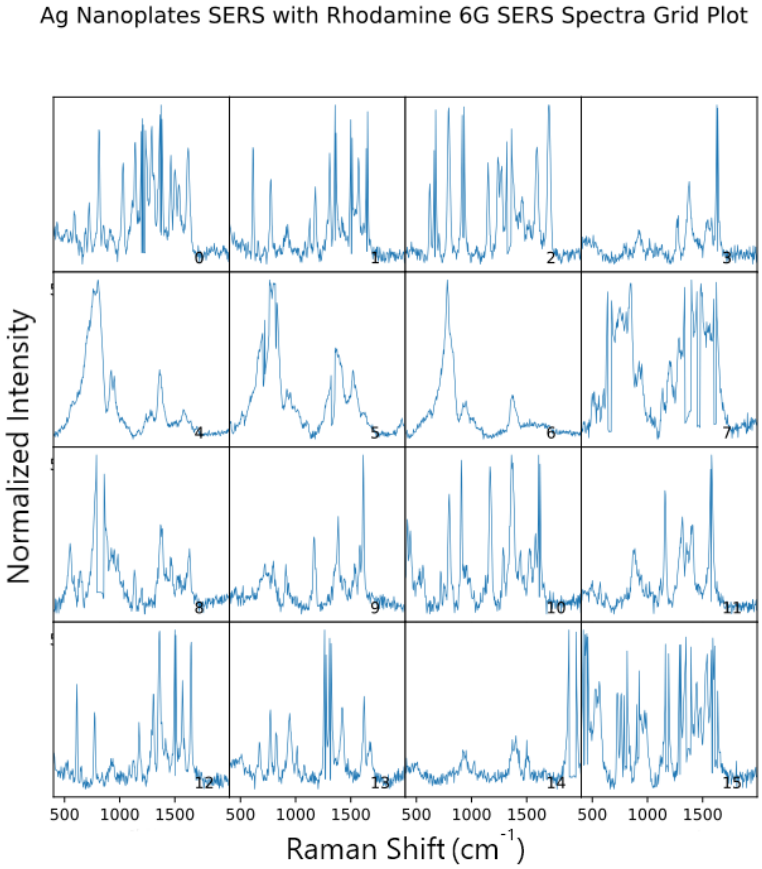

Figure 69: Grid plots of high intensity R6G nanoplates SERS spectra

6.2.1.1 Principal Component Analysis Data

The Scree and Loadings plots (Figures 70 and 71a) showed similar trends to the previous nanostructures, with the first PC making up a large portion of the total variance, with the subsequent PCs comprising progressively less. Noteworthy observations about the Scree plot include PC1 constituting approximately 25% of the total variance, which is larger than previous nanostructures, and PC2 making up a significant portion of the variance (15%). The expected drop off variance coverage was still observed in the later PCs, with the drop off being consistent with previous nanostructures. The relatively high variance covered by PC2 could be indicative of clustering as there were two different PCs that covered a significant portion of the total variance. The Loadings plots showed similar trends to the previous nanostructures, with PC1 and PC2 having highly weighted regions similar to those seen in the spectral plots. The weighted regions differed between PC1 and PC2, which was expected as they were representing different amounts of variance. PC1 had two large regions, one between 600 – 1000 cm^{-1} and the other between 1200 – 1600 cm^{-1}, while PC2 had a region between 800 – 1600 cm^{-1}. Given the large number of peaks within these wavenumber regions, having high variance over two principal components in the same wavenumber range was theoretically possible. The drop-off in variance covered by

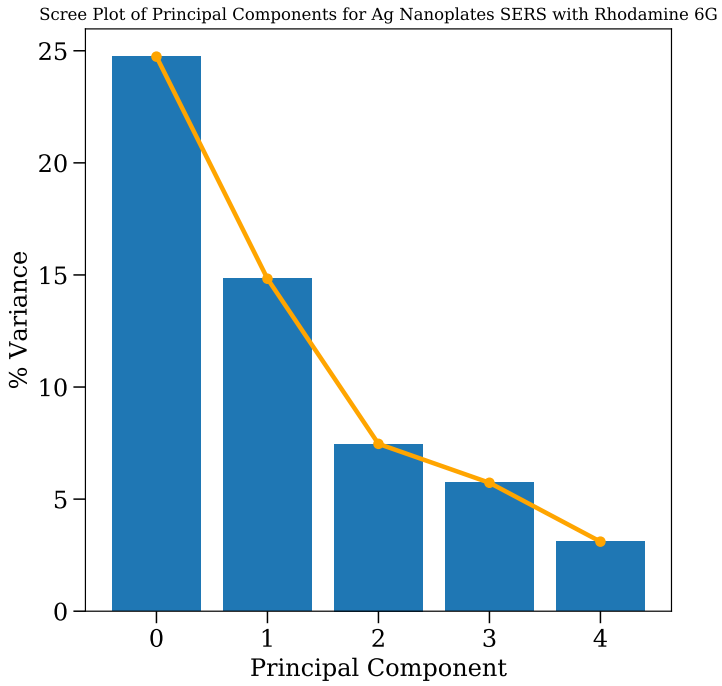

Figure 70: Scree plot of R6G nanoplates SERS data

the each of the PCs follows the trends seen in the other sets of data, with the primary and secondary PC containing a large portion of the total variance, while the remaining PCs made up around 5% of the variance each.

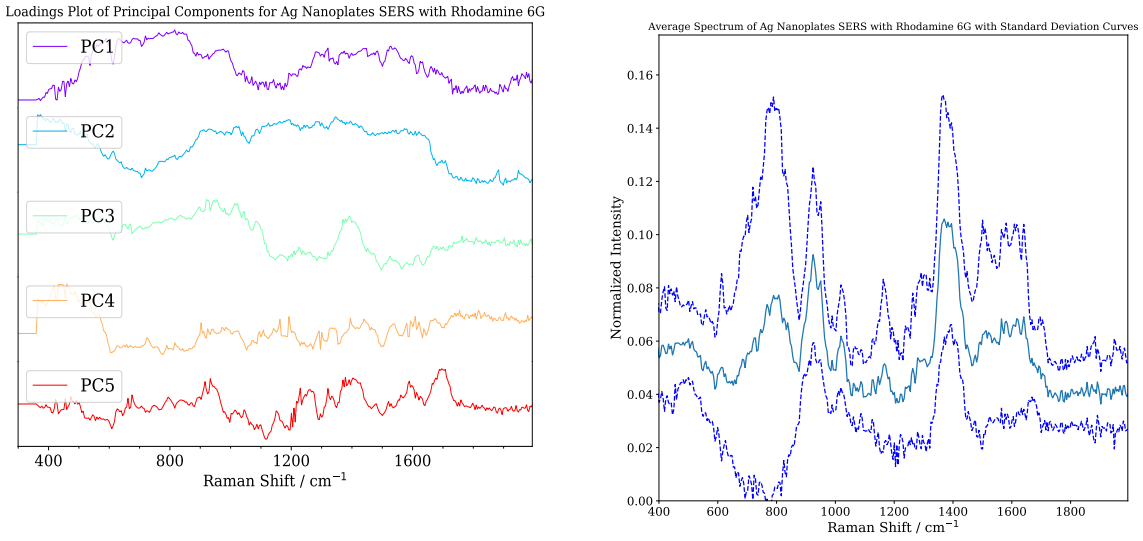

(a) **(b)** .

Figure 71: Loadings plot (a) and average spectrum with standard deviation curves (b) for R6G Ag nanoplate SERS data.

The Score's plot (Figure 72a) for the R6G nanoplate data displayed interesting patterns, ranging from clustering to long streams of data points, to combinations of both. Score's plots produced using PC1 exhibited mainly clustering, while PC2 plots displayed patterns closer to the ones seen in the R6G nanocube data, where a stream of data points leads to a cluster of data. The difference between the PC1 and PC2 plots was another promising piece of evidence suggest the existence of two distinctly different types of spectra present inside the data set. The plots produced using the remaining PCs showed loosely fitting clusters, like those seen in the PC1 plots.

The 3D Score's plot (Figure 72b) clearly shows the stream of data points connecting to the large cluster of data points. The bulk of the data points made up the cluster, with a small portion used in the creation of the stream while the remaining points were outlier points existing at the extremes of the axis. The cluster appeared to be tightly packed with a low number of extreme outlier points.

It was possible that the distribution of data points shown in the 3d Score's plot could be representative of two or more different spectra existing inside the data. The outlier data

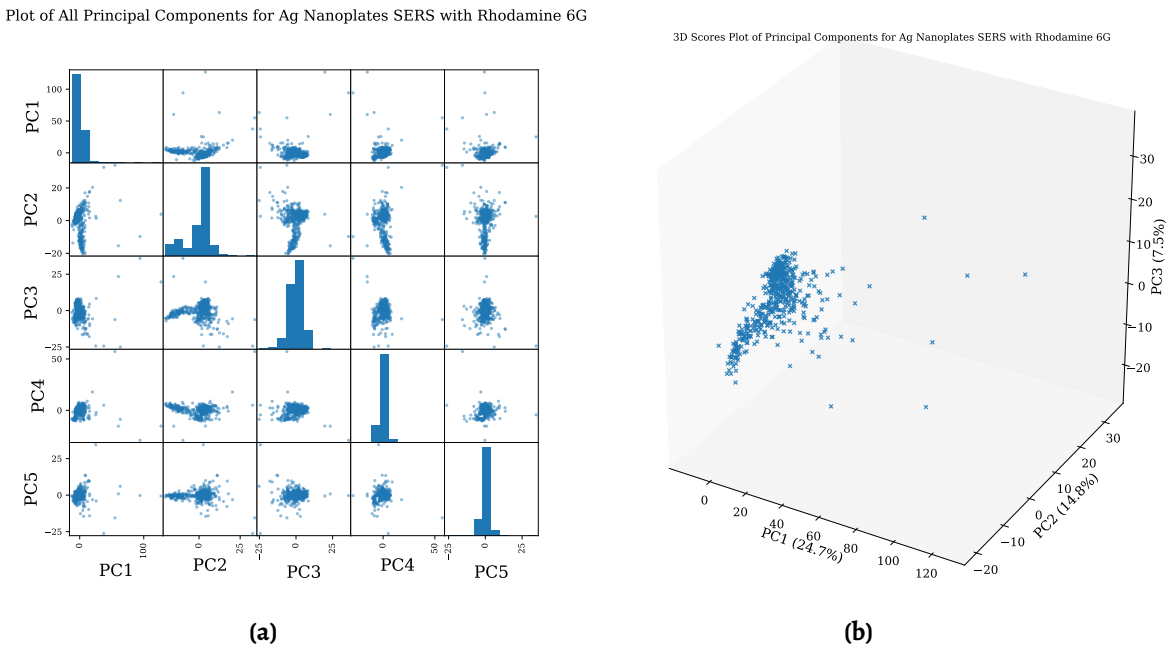

(a) (b)

Figure 72: Scores scatter plot (a) and 3D Scores plot (b) for R6G Ag nanoplate SERS data.

points were probably spectra that contain contaminant peaks and/or the spectra with the extreme enhancement. The data points that made up the cluster were tightly clustered suggesting that they should be spectrally similar, while the data points that made up the stream were somewhat similar to the clustered data points but grow progressively different as they travelled away from the cluster. This sort of trend does not fit with the clustering theory hypothesis and was possibly evidence of the continuum theory instead, as this progressive change in spectral data was more consistent with the data shown in previous nanostructures data sets.

The outlier spectra displayed in the Score's plots produced using the R6G nanoplate data set were plotted and displayed in the grid plot seen in Figure 73a. These outlier spectra followed the trends observed in the nanocube and nanowire data sets, with a range of spectra being displayed, all of which contained a different distribution of peak enhancement and intensity. Unlike many of the other data sets there did not appear to be any clear patterns or trends within these spectra, as none of them shared any clear similarities. After referring back to the Score's plot (Figure 73b) used to identify the outlier spectra, all 6 spectra displayed in Figure 73a were clearly separate from the main cluster of spectra. When comparing this separation to the Euclidean distance for the respective spectra, it appeared that only one of the outlier spectra, spectra 57 displayed in plot 5 of Figure 73a,

had a distance value that matched the separation observed in the Score's plot. All other outlier spectra (1, 25, 26, 27 and 249) did not appear to have distance values close to what would be expected given the separation observed in the Score's plots, as all their distance values were below 2. Given the huge difference in distance value of spectra 57 compared to other spectra, the distance value of the other outlier spectra may have been disproportionally represented or suppressed, resulting in them not be accurately represented in the Euclidean distance map. Excluding this observation, it appeared that the trend of the PCA separation not matching the Euclidean distance value continued for this data set.

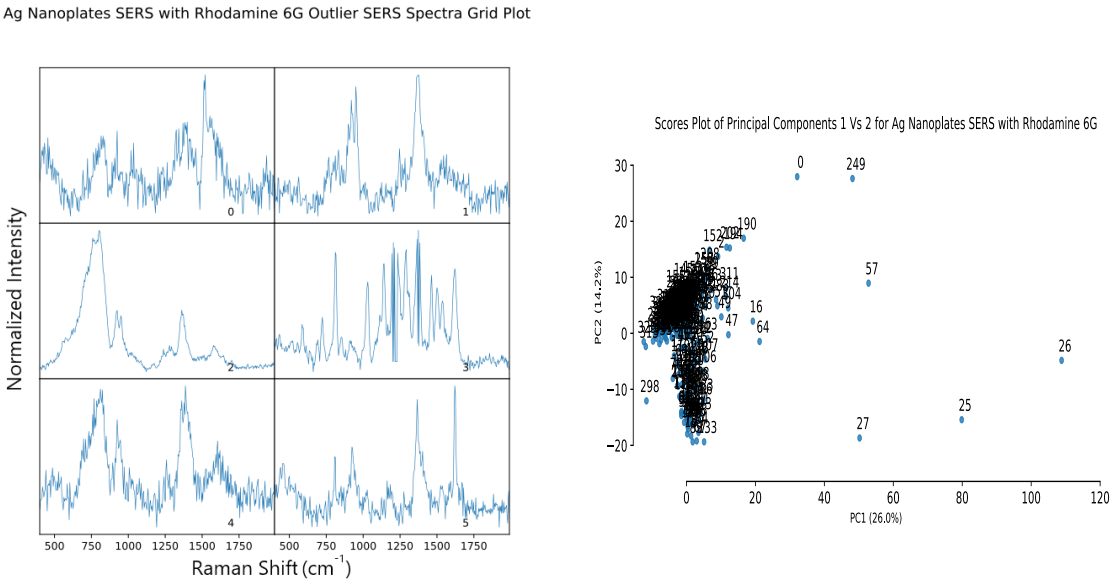

Figure 73: Spectral grid plot of outlier spectra (a) and Scores plot of PC1 and PC2 (b) for R6G nanoplates SERS data

6.2.1.2 Clustering Data

The Euclidean distance map (Figure 74) appeared to correlate with the Score's plot, as many of the spectra were similar, as shown in the high number of spectra with a distance value of approximately 2 or lower. There was some diversity within these spectra, with some spectra having a distance within the 2-3 distance range. These are most probably the spectra that make up the string of data points observed in the Score's plot. The outlier data points seen in the Score's plots were also present in the distance map, with several spectra containing a distance value above 5, indicating a large difference between those spectra and their neighbours. The dark regions inside the distance map relate to the spectra inside the cluster, as their distance values are below 1, indicating a high degree of similarity between them. These observations matched the appearance of Score's plot and act as possible evidence towards validating the theory that a continuum of spectra was present inside the spectra.

The low distance between the spectra is also displayed in the self-organizing map (Figure

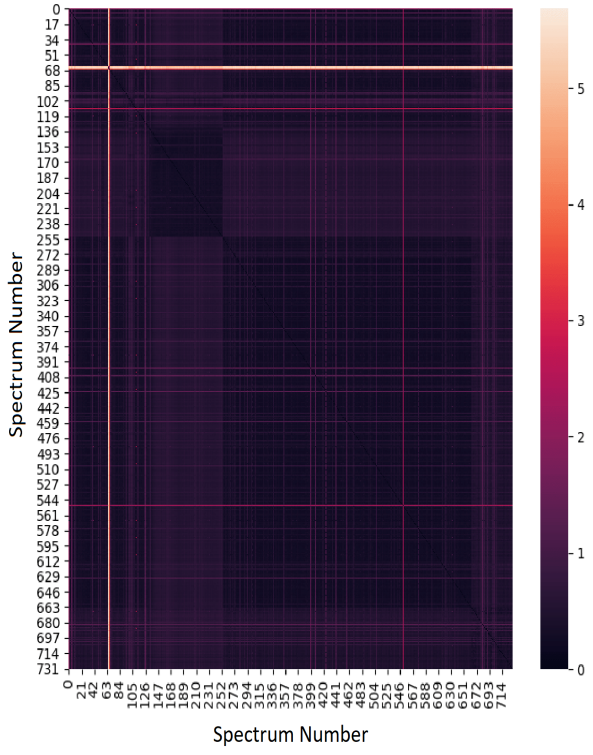

Figure 74: Euclidean distance map of R6G Ag nanoplates SERS data

75) generated from this data set, as unlike previous data sets, the distance scale bar on the right of the map showed a maximum distance of 1.25, in comparison to other data sets which had a maximum distance well above this. A single cluster of nodes with a large dis-

tance difference in comparison to neighbouring nodes was present inside the map and was probably due to the outlier peaks. The reason for this assessment stems from the evidence provided by the Euclidean distance map, that showed only a few spectra had a high distance value and the appearance of outlier peaks shown in the Score's plots. The spectra that make up the cluster and stream of data points in the Score's plots were probably not being represented by the cluster in the self-organising map, as they had very low distance differences and were quite tightly clustered. For this reason, it was more likely that the yellow node was the outlier peaks, while the greenish blue nodes were the spectra inside the cluster and stream. The Euclidean distance and self-organising maps did not provide any additional information into the validity of either of the leading theories.

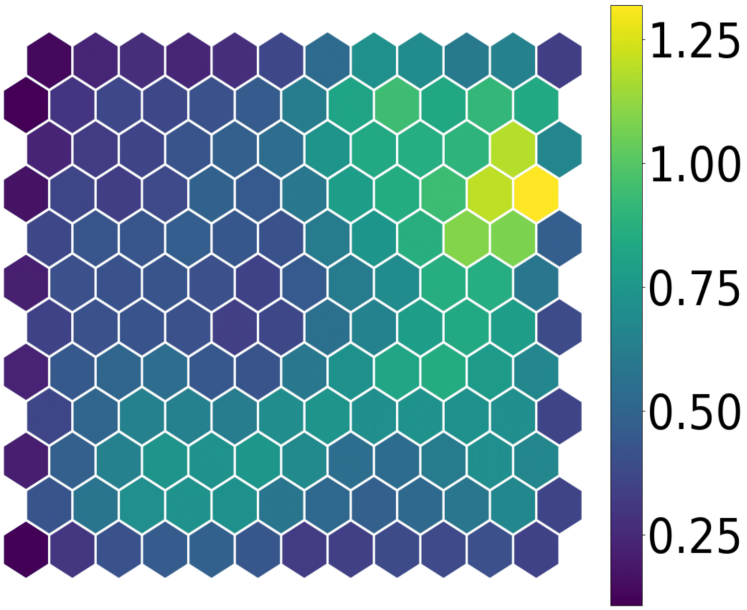

Figure 75: Self-organizing map of R6G Ag nanoplates SERS data

6.2.2 Surface-enhanced Raman Scattering of CV

The SERS spectra collected of the CV adhered to the nanoplates (Figure 76) displayed several strong peaks over the entire spectral range. Within these peaks are some that are only present in a single spectra and occur at wavenumbers that are uncommon in comparison to both the other spectra as well as the literature wavenumber values for CV. Much like the SERS spectra of R6G that was collected using the nanoplates, the peak positions with the highest density were clearly visible in the baseline of the spectral plot, making it easier to distinguish which peak positions were being regularly expressed during a SERS event. Unlike the R6G nanoplate spectral plot, the signal-to-noise in the region between 1100-1600 cm^{-1} was improved and allowed for better identification of peaks positions inside this region. The expected peaks for CV all appear to be present within the spectral plot, with some minor shifts in wavenumber that may have been due to fluctuations in bond length given the very slow exposure time used during SERS data collection. The peaks between 1500 cm^{-1} and 1650 cm^{-1} appear to have undergone the largest peak shifting, which was possibly being caused by the fluctuation of aromatic C-C bond lengths inside the aromatic rings. This peak shifting was especially prominent because of the very low

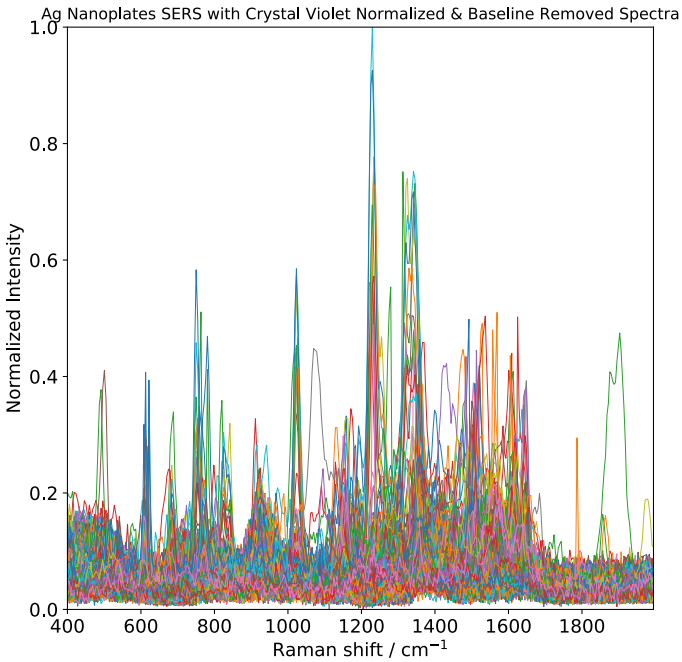

Figure 76: Spectral plot of CV Ag nanoplates SERS spectra made up of 572 spectra

exposure time of the spectrometer, as bond length fluctuation would be easier to detect

in comparison to literature values that are collected with long exposure times. Within the 1500-1650 cm^{-1} range there is expected to be two peaks, one at 1590 cm^{-1} and the other at 1622 cm^{-1}, both of which correspond to the C-C aromatic stretch. The peaks at 1371 cm^{-1} correspond to the C-C centre stretching vibrational mode, while the peaks at 1178 cm^{-1} and 806 cm^{-1} were C-H bending vibrational modes. The peaks at 914 cm^{-1} are typically associated with radical-ring skeletal vibrational modes. The only unidentified peaks were at approximately 1200 cm^{-1} and could possibly be attributed to either a shift of the 1178 cm^{-1} peaks or they could correspond to another vibrational mode that is unaccounted for in the literature. The peaks at this position were strong and frequent, indicating that they were unlikely to be caused by contaminants and are possibly either peak shifted C-C centre stretching or C-H bending vibrations, although their origin was unclear.

As observed with the R6G nanoplate data, the high intensity spectral plot (Figure 77a) showed the consistency in the bands being enhanced. Many of the outlier peaks were removed in the high intensity spectral plot, with most of the peaks fitting with the expected peak positions. The high intensity plot had an improved signal-to-noise, which further enabled peak identification and showed the amount of peak shifting that occurs between SERS spectra. This improvement made the identification of outlier peaks, such as the peak at 1900 cm^{-1}, much easier. Similar to the R6G nanocube data set, there was a distinct group of spectra that contained identical peaks across the entire spectral range, although unlike the nanocubes data, the signal-to-noise for this data set was considerably worse. The identical spectra present in the high intensity spectra were isolated and plotted to improve the signal-to-noise ratio. Ten spectra made up the isolated spectral plot with only one of these spectra appearing to contain peaks that did not fit the trends of other spectra (Figure 77b).

The high intensity grid plot for the CV nanoplate data set (Figure 78) showed the largest amount of similarity between the spectra plotted. The grid plot consisted of 16 spectra, 12 of which shared a high degree of similarity with regard to their peak enhancement and intensity. There did not appear to be much variance with regard to which bands were enhanced and how intense the enhancement was between these spectra, possibly indicating that this was the most dominant spectra generated during SERS signal collection.

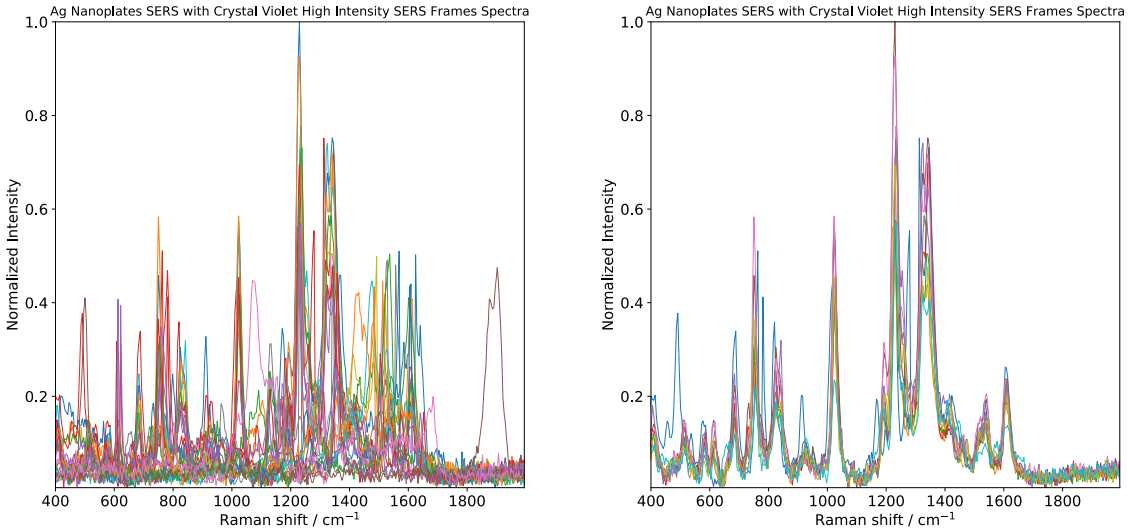

(a) High intensity spectral plot of CV nanoplate SERS spectra made up of 215 spectra

(b) High intensity spectral plot of CV nanoplate SERS spectra made up of 10 spectra

Figure 77: Spectral plots of Ag nanoplates CV SERS spectra for both high intensity (a) and maximum spectra (b).

Excluding this pattern the only observation of note was in plot 4, which appeared to consist of two strong sharp peaks with no other peak enhancement. This is possibly caused by a cosmic spike not being removed during the statistical analysis portion of the data processing protocol.

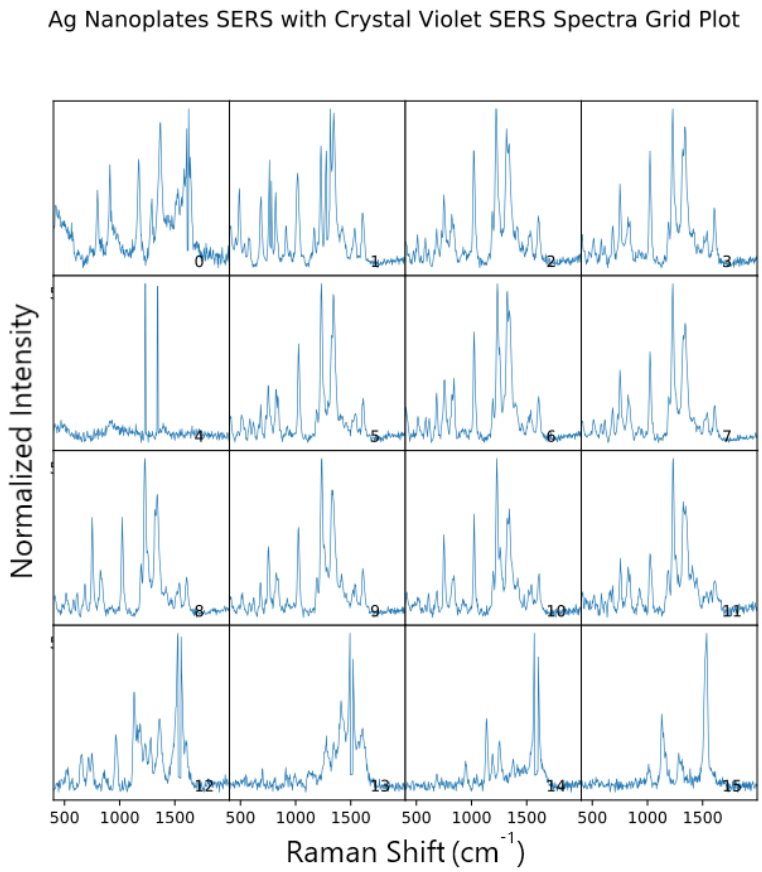

Figure 78: Grid plots of high intensity CV nanoplates SERS spectra

6.2.2.1 Principal Component Analysis Data

The Scree and Loadings plots (Figures 79 and 80a) for the CV nanoplate data set followed the trends established from the previous data sets, with PC1 and PC2 covering large portions of the total variance each while the remaining PCs cover progressively lower amounts of variance, with the last PCs covering approximately 5% each. The coverage provided by PC1 was comparable to previous data sets, with it making up approximately 23% of the total variance. The drop-off in variance between PC1 and PC2 is approximately 7%, which was lower when compared to other data sets. The Scree plot is similar in appearance to the Scree plot produced using the CV nanowire data set, as both contain PC2 peaks that were responsible for a large variance coverage. In the CV nanowire data set, the variance covered by PC2 was related to the peak density at 800 cm^{-1} and correlated to the C-H bending vibrational mode. The Loadings plot of the CV nanoplate data set did not appear to continue this trend, as the PC2 plot showed high weighted regions at multiple wavenumber regions that coincided with peaks on the spectral plot. Unlike the CV

nanowire data set, the Loadings plots of PC1 and PC2 for the CV nanoplate data shared several regions of high weight over the entire spectral range. These regions of variance do coincide with peaks in the spectral plot, but it was curious that there was such a large overlap in high variance areas, especially in the peaks in the region between 600-1000 cm^{-1}. Some overlap had been observed in other data sets but was usually confined to regions that coincided with high peak density, such as the peaks between 1200-1600 cm^{-1} in the spectral plot. Both PC1 and PC2 have Loading plots that could be representative of different spectra inside the data set, as both contain peaks in all areas of interest for CV SERS. This could mean that PC1 represented one subset of spectra, while PC2 was representative of another, both of which were sufficiently different to be distinguished by the PCA. Correlating this explanation to the spectral plots it was possible that one of the PCs was representative of the spectra displayed in the isolated high intensity spectra, while the other PC represented the remaining spectra. The spectra displayed in the isolated high intensity plot only made up a small portion of the total spectra used in the PCA, 10 spectra out of a 300, and could possibly have been represented by one of the PCs with a low weight coverage, leaving the larger PCs to represent the non-identical peaks. Outside of these observations the Loadings and Scree plots followed the same trends pre-

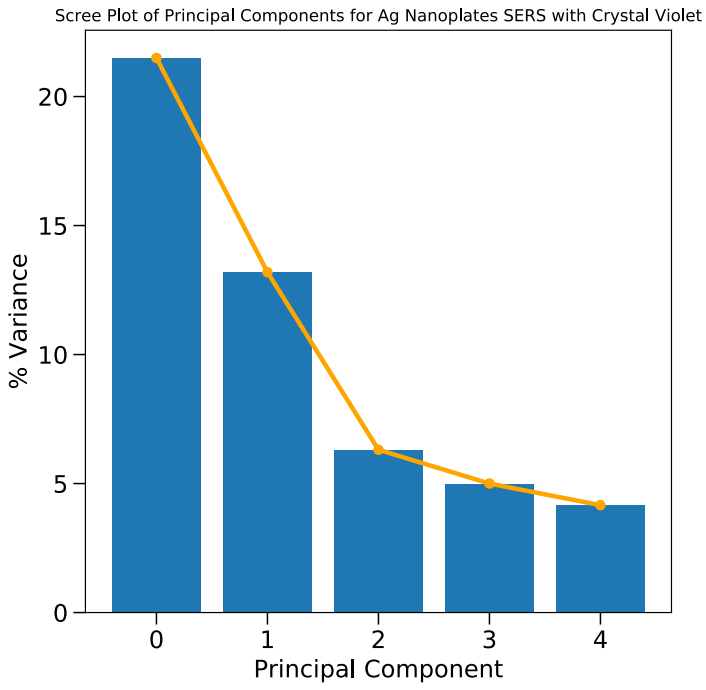

Figure 79: Scree plot of CV Ag nanoplates SERS data

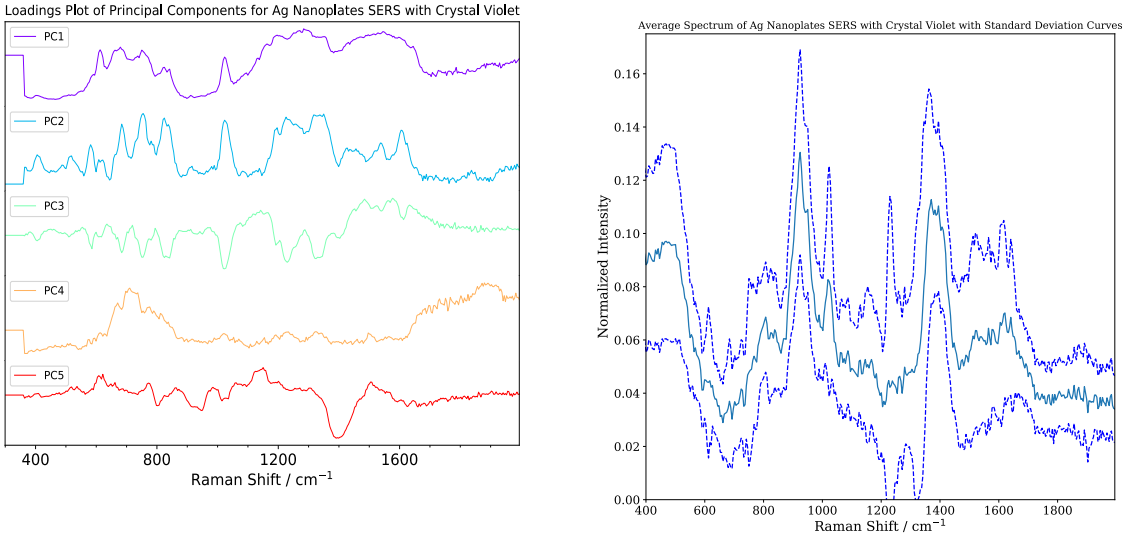

(a) **(b)**

Figure 80: Loadings plot (a) and average spectrum with standard deviation curves (b) for CV Ag nanoplate SERS data.

sented in all the data sets investigated in this project. The Score's plot (Figure 81a) of the CV nanoplate data provided the greatest evidence of clustering inside any of the data sets investigated, as there was clearly a separation in the data points observed in many plots, especially in the plots containing PC1 and PC2. Plots with PC1 show the greatest separation and clustering in the data, with two obvious clusters, one more tightly packed than the other, while PC2 plots was dominated by a single cluster surrounded by outlier peaks. Some of the trends observed in previous data sets such as the strings of data points did not appear to be present in these plots. The clusters shown in the PC1 plots had the greatest separation observed in any of the data sets, but it appeared that one of the clusters present was tightly packed, while the other was more loosely fit, with its packing density depending on which other PC it was being plotted against. As PC1 and PC2 made up the largest portion of the variance of all the PCs, the plots produced using these PCs were probably a better indication of any separation in the data. The separation between the data point clusters was even more apparent in the 3D Score's plot (Figure 81b) as there was a clear separation between the two groups of data points. Despite this separation the secondary group of data points did not appear to be as tightly packed as originally expected based on the 2D Score's plot. The introduction of the additional dimension revealed that the data points making up the less packed cluster were merely overlapping

with each other along the additional axis. Both clusters contained some spread, especially the weakly packed cluster, this was suspected to be caused by small variations inside the spectra. The tightly packed cluster could be representative of spectra shown in the isolated spectral plot, given the low spread in the cluster and the uniformity of the spectra. The separation in the clusters potentially meant that there were two or more groups of spectra present inside the data, each of which were different enough to be distinguishable using PCA. Given the obvious separation in the clusters, it was safe to assume that at least two groups of spectra were present, but determining if additional groups were present becomes difficult, as the spread around both clusters may be representative of this, but it was not as obvious. It was possible that the data points surrounding both clusters still belonged to their respective group, but contained slight differences in peak position or intensity, resulting in their separation from the centre of the cluster. The out-

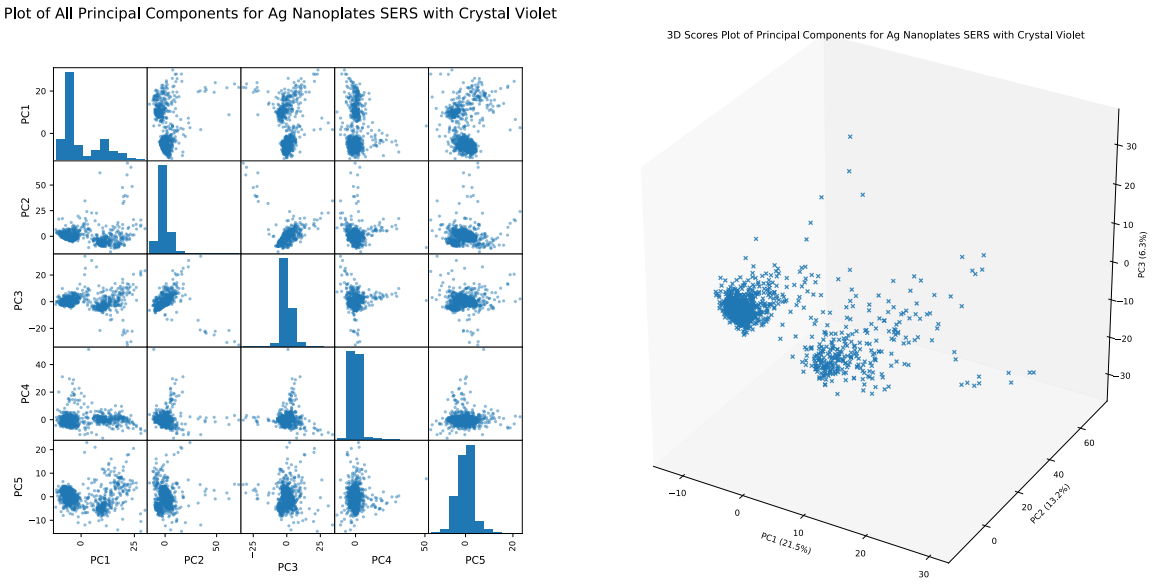

(a) **(b)**

Figure 81: Scores scatter plot (a) and 3D Scores plot (b) of CV Ag nanoplates SERS data

lier spectra for the CV nanoplate data set (Figure 82a) showed an interesting collection of spectra that did not appear to follow the same trends shown in the previous data sets, as the majority of the spectra contained sharp consistent peak enhancement, with plots 0, 3, 4 and 5 are very similar to the spectra displayed in Figure 78. The suspected cosmic spike spectra, shown in plot 2, matches the spectra displayed in Figure 78 which was expected given its differences to the other spectra. The addition of plots 0, 3, 4 and 5 to the list of outlier spectra could suggest that the high intensity spectra, displayed in Figures

77b and 78, make up a very small portion of the total spectra, leading to them being isolated by PCA and segregated from the main cluster of spectra. Another observation that was made about the outlier spectra was found after consulting the Score's plot used for the identification of the outliers. Another observation for the outlier spectra stemmed from the Score's plot used to identify them (Figures 82b), as the outlier spectra were in a sequential order. All other data sets contained outlier spectra that were spread throughout all SERS spectra and not in any sequential order. Given the similarities in the outlier spectra and the fact that they are in sequential order, it was possible that these spectra were collected from the same nanoplate + dye molecule combination that could possibly be trapped within the focus of the laser, similar to the spectra displayed in Figure 19. Comparing the outlier spectra (spectra 91-100) with their corresponding Euclidean distance values, it appeared that the similar trend observed in the previous data sets was present inside the CV nanoplate data, as all of the outlier spectra had low Euclidean distance values, between 0.5-1. None of the high distance value spectra, 360-370, were all located within the main clusters of the Score's plots, while all outlier spectra displayed in the Score's plots had low corresponding distance values. Given that this trend was present through the majority of the data sets, it appears that the outlier spectra displayed in the PCA outputs were not supported by the Euclidean distance evidence, making it difficult to accurately determine which spectra are truly different from others.

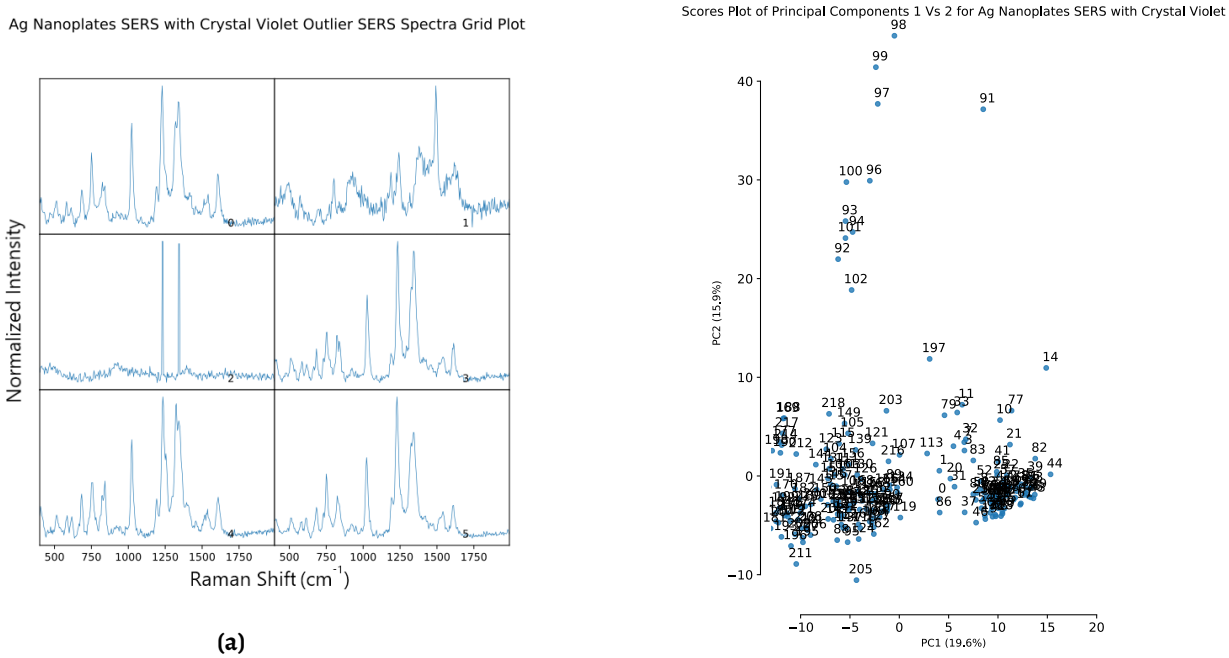

Figure 82: Spectral grid plot of outlier spectra (a) and Scores plot of PC1 and PC2 (b) for CV nanoplates SERS data

6.2.2.2 Clustering Data

The Euclidean distance map (Figure 83) appeared to follow the trends seen in the Score's plots, with a large portion of the spectra having a distance value of 0.5, another portion having a distance value of 1.5 and a small portion having a value above 3.5. The spectra with values of 0.5 and 1.5 fitted with the two clusters observed in the Score's plots, as most spectra observed in the Score's plots were grouped together into one of two groups. The outlier peaks sitting at the extremes of the Score's plot were represented by the spectra with distance values above 3.5, which both fits the trends established from previous data sets and makes sense given the distance between the outlier points and the other data points in the Score's plots. It was difficult to determine which cluster was being represented by the 0.5 and 1.5 distance spectra, as the point of reference for the distance measurement is unknown. As the difference in spread between the two cluster was drastically different, it was probable that the spectra with a distance value around 1.5 are the loosely packed cluster, while the 0.5 spectra made up the tightly packed cluster. The self-organising map output (Figure 84) was not as easy to interpret as, excluding the yellow

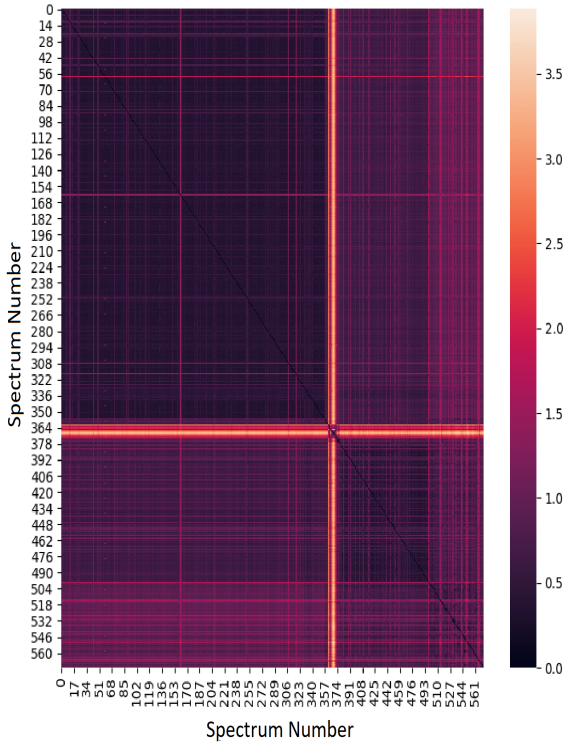

Figure 83: Euclidean distance map of CV Ag nanoplates SERS data

nodes which possibly represent the outlier peaks, there did not appear to be an obvious trend inside the remaining nodes. Assuming the conclusions drawn from the PCA and Euclidean outputs were correct, then the self-organising map should show three regions with difference distance values, two correlating to different clusters and one correlating to the outlier peaks. The outlier peaks appeared to be represented by the yellow nodes, as they have the highest distance difference, but there did not appear to be two distinct regions that could be associated with the two clusters observed in the Score's plots. Based on the results of previous data sets it would be reasonable to assume that one cluster would be represented by blue nodes and the other by greenish blue nodes, as there should be a distance difference between them. There were some regions of blue and green-blue nodes, but they did not fit the expected pattern derived from the PCA and Euclidean outputs. It was plausible that the yellow nodes represent the clusters, but this assumption does not appear to fit with the other evidence, as it would imply that the nodes surrounding the yellow "cluster" nodes have a lower distance difference than the spectra inside the clusters. As these spectra are outliers, their distance values should be large and varied, which was observed in the PCA and Euclidean outputs and would not fit the idea that the yellow nodes represent the clustered spectra.

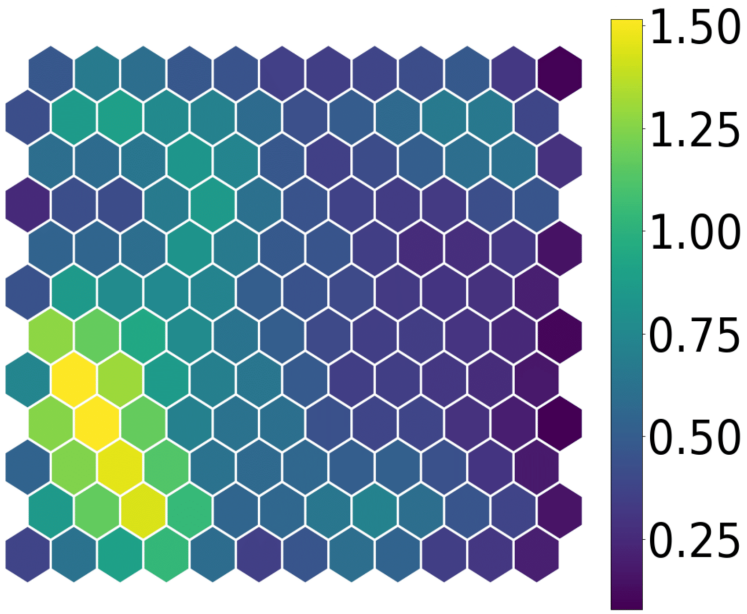

Figure 84: Self-organizing map of CV Ag nanoplates SERS data

6.3 Summary

The nanoplate data appeared to offer the greatest evidence towards the clustering theory, as both the R6G and CV data displayed patterns that were consistent with this theory, as seen in their respective Score's plots. The spectra for both dye molecules contained consistent, strong enhancement across all regions of interest for both dye molecules. Although the strength of the enhancement was weaker compared to the nanocubes, the consistency in the enhancement over all vibrational modes was superior to both the nanocubes and nanowires. This consistent enhancement can be linked to the superior uniformity of the nanoplates compared to the other structures, while the decreased enhancement strength most probably stems from the comparative dullness of the edges and corners of the nanoplates. These theories would fit the outputs of both the nanoplates and the other nanostructures, as the structures with the weakest enhancement also contained the lowest uniformity and quality. The output of the CV data set showed a distinct separation between two sets of clusters, while the R6G data set showed a single cluster with a string of connected data points. The difficulty in making conclusions as to which theory fits the data outputs better stems from the inconsistency in results between the different dye molecules. The R6G outputs appeared to favour the continuum theory, as the connected string of data points indicated only slight differences separated the spectra from each other, while the CV outputs ran counter to this, with two isolated groups of data points

that favoured the cluster theory rather than the continuum. Despite all Scree plots displaying a sharp drop-off in variance coverage after PC3, five PCs were still investigated to gain a more complete understanding of the trends inside the data. Using five PCs over three did not change the outputs of any plots used to make any conclusions (3D Score's plot, Euclidean distance map or self-organizing map) as the two maps did not use the PCA data and the 3D Score's plot only used the first three PCs.

CHAPTER 7

Additional Experiments

7.1 Contaminant Peaks

One consistent trend present in all nanostructures was the occurrence of outliers SERS peaks within wavenumber ranges not typically associated with either dye molecules. Several assumptions were made to account for these peaks, with the major assumptions being contaminations and peak shifting. After considering what contaminants could be present in all nanostructures, the obvious culprits were the capping agents used in the synthesis of all three structures. Each of the structures required a capping agent to maintain their respective shape long-term as they would become irregularly shaped if the capping agent was removed or was not present. Unfortunately, both capping agents used were Raman active and contained vibrational modes similar to the vibrational modes of the dye molecules. The capping agents in question were PVP, used for the nanocubes and nanowires, and TSC used for the nanoplates. Both PVP and TSC (Figures 85a and 85b) contained several vibrational modes, including the C-C bending mode, C-H bending and stretching modes, and the C=O stretching mode. All of these modes could be present in the spectrum collected at similar wavenumber regions as both dye molecules, and may have been responsible for the enhancement provided by structures. Fortunately, both PVP and TSC are considered weak Raman scattering compounds, meaning that despite containing Raman active vibrational modes, they would only undergo weak enhancement over these bands. When combined with a strong Raman scattering compound, such as R6G or CV, the vibrational modes from PVP and TSC would still be present but would most probably be suppressed. An important difference between the capping

agents and the dye molecules used for SERS is the intrinsic resonance enhancement of the dye molecules. This intrinsic enhancement stemmed from their $\pi - \pi^*$ transitions that are in the visible region and close to the wavelength of the laser. This enhancement can be several orders of magnitude and is not present inside the capping agents, resulting would likely dominate any SERS signal stemming from the capping agents. Attempts were made to collect SERS spectra of TSC and PVP experimentally by collecting just the signal from the nanostructures in solution, absent a dye molecule, but no obvious peaks were present for any of the nanostructures. This could mean that PVP and TSC are either too weak of scattering compounds for their signals to be observed, or not enough SERS events were occurring for a consistent signal to be produced. The concentration of the capping agents during these experiments would be approximately 1 mM, making it unlikely that a Raman signal would be observed from such weak scattering compounds, especially given the very low excitation power. A possible theory for why the PVP and TSC modes may only be present when a dye compound is present may be due to the charge exchange component of SERS theory, as the dye molecule will readily undergo this charge exchange and enable the capping agent, that were bonded to the Ag atoms, to also under this charge exchange interaction. Having the capping agent bonded to the Ag atoms may be negatively impacting the SERS mechanism for PVP or TSC if the dye molecule was not present to facilitate that interaction.

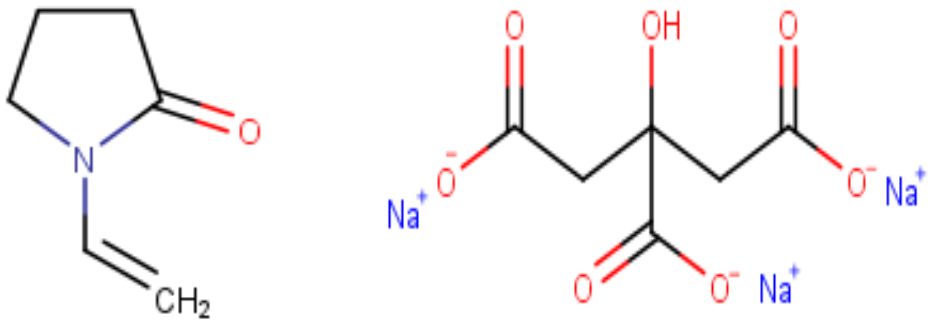

(a) **(b)**

Figure 85: Chemical structure of vinylpyrrolidone (a) and trisodium citrate (b)

7.2 Extreme Concentration SERS

To determine the limitations of the techniques used to characterise the nanostructures, SERS experiments were performed using both R6G and CV at extremely low concentrations and adhering to all three nanostructures. The experimental setup was unchanged with the exception of a change in the dye molecules. The reason for undertaking these experiments was twofold, firstly to test the concentration limit for SERS collection using the different structures, and secondly the decreased concentration would mean that any SERS signal collected was caused by a single dye molecule adhered to the structure. This should eliminate the suspicion that multiple dye molecules could be adhered to a structure during SERS collection, meaning that any SERS signal collected should be generated from a single molecule adhered to either a face, edge, or corner. This may also provide some validation of the clustering idea, where differences in SERS signal can be related to the position at which the dye molecule adhere. Unsurprisingly, the amount of SERS spectra collected using the nanocubes was substantially lower than any of the previous concentration ranges, while the nanoplates and nanowires failed to provide the required enhancement to produce a SERS signal strong enough to be observed over the baseline noise of the spectrometer. The 3D Score's plots (Figure 86) for each of the dye molecules and concentrations were plotted and compared to determine if any trends were present. As each of the experiments contained a small number of spectra, approximately 30, the 3D Score's plot provided the best insight into how the spectra relate to one another.

The other clustering techniques implemented for the high concentration spectra were not suitable for these spectra, as they require a larger sample set to achieve accurate outputs. Deciphering what trends were present in the 3D Score's plots was challenging, as the low number of spectra led to possible misleading patterns. An argument could be made for the appearance of grouping in the both the R6G plots and the $1x10^{-14}$ M CV plot (Figures 86a, 86c), as there was a distinct separation between multiple groups of data points. This grouping was most prevalent in the R6G $1x10^{-15}$ M plot (Figure 86d), although the number of data points in this plot was much lower than the other plots, leading to a higher uncertainty as to whether this grouping was truly representative of the spectra. Both the CV plots showed the weakest evidence of grouping, with a wide spread of

data points across the entire plot and minimal data point grouping. The spread in the data points observed in all these plots appeared to be similar to the higher concentration plots, indicating that the region-specific clustering idea may be an incorrect assumption to make when considering the generation of SERS spectra. Ideally the low concentration spectra would fit into three tight clusters, one per region, if they were following the region-specific clustering theory, but given the evidence collected from both the low and high concentration data, it appeared that this theory was incorrect.

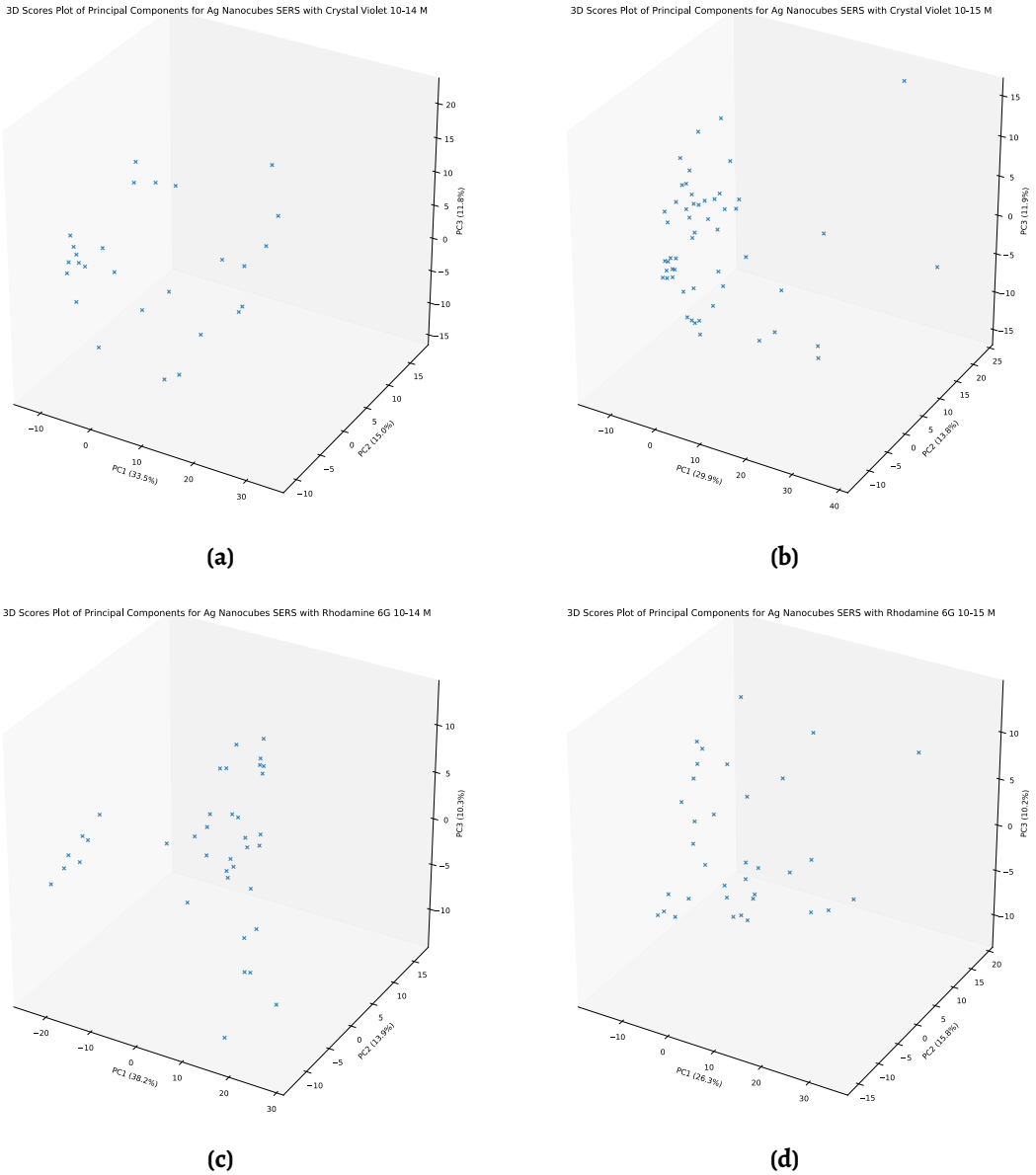

Figure 86: 3D Scores plots for CV (a, b) and R6G (c, d) at 1x10^{-14} M and 1x10^{-15} M using nanocubes as the substrate

7.3 Raman Tweezers

The Raman tweezer experiments were not completed due to the time constraints of the project. The decoration of silica micron spheres with controlled uniform AgNS was successfully completed before being trapped using the conventional optical tweezers setup. Several attempts were made to implement the Raman spectrometer into the optical tweezer setup, but the task was more complex than original expected and was not successfully implemented.

CHAPTER 8

Comparison of Nanostructures

Comparing the three nanostructures when considering their SERS enhancement can be difficult, as there are various components to enhancement and there may be nanostructures that are more suited to one component than others. This made it necessary to establish several parameters to compare the nanostructures against to gain a complete understanding of the differences between the nanostructure's enhancement. These parameters included the ratio of SERS spectra to total spectra collected, the amount of enhancement observed in the SERS spectra collected and the amount of variation between the SERS spectra collected. The ratio of SERS spectra to total spectra collected and the amount of SERS enhancement observed were the most investigated parameters as they offered the most information into the effectiveness of using a certain nanostructure as a SERS substrate. The final parameter, the amount of variation between SERS spectra, was investigated as it provided insight into whether a discrete number of SERS spectra clusters were being recorded. The hypothesis was that dye molecules situated on different regions of the controlled structures would lead to different spectral signals being recorded. The difference in SERS signal is believed to be caused by the change in which vibrational modes were being expressed due to different LSPR energies being present at faces, edges, and corners. All SERS data collected for each of the nanostructures were tabulated and analysed to determine which of the nanostructures fits the parameters best (Tables 7, 8, 9, 10). The ratio of SERS spectra to total spectra parameter was most dominant in the nanowires, with a SERS occurrence rate of 7.5% and 6.6% (Tables 7 and 8). As the nanowires were larger in size compared to the nanocubes and nanoplates, it

was expected that the nanowires would produce more SERS spectra. This was because the nanowires were less effected by both random thermal fluctuations causing Brownian motion and motion caused by the gradient force of the laser, meaning they are more likely to spend longer inside the focus of the laser. If a nanowire was present inside the focus of the laser and meets the requirements for SERS to occur, it will remain in the focus longer and more SERS spectra would be collected. This was observed experimentally as the SERS data for the nanowires consisted of long periods of sustained enhancement rather than the typically sporadic, short term enhancement observed with the nanocubes and the nanoplates. It was difficult to assess the sustained enhancement and determine whether it was a result of the laser gradient force trapping the nanowires in the focus or if the nanowires were simply too large to be removed from the focus as quickly as the other nanostructures. The SERS spectra occurrence was comparable between the nanocubes and nanoplates, with a SERS ratio between 4.4-5.8% for both while nanowires had a ratio of 6.6-7.5%. Despite the high rate of SERS spectra recorded using the nanowires the amount of enhancement provided by them was worse compared to the smaller nanostructures. This decrease in enhancement could be caused by the lack of sharp edges and corners on the nanowires compared to the other nanostructures.

Table 7: Table of SERS spectra occurrence in R6G samples

Table of R6G SERS spectra occurrence			
	Nanocubes	Nanowires	Nanoplates
Total spectra collected	12000	12000	12000
Total SERS spectra	526	903	734
SERS spectra : Total spectra ratio	0.044	0.075	0.058
SERS spectra : Total spectra percentage	4.4%	7.5%	5.8%

Table 8: Table of SERS spectra occurrence in CV samples

Table of CV SERS spectra occurrence			
	Nanocubes	Nanowires	Nanoplates
Total spectra collected	12000	12000	12000
Total SERS spectra	706	790	572
SERS spectra : Total spectra ratio	0.059	0.066	0.043
SERS spectra : Total spectra percentage	5.9%	6.6%	4.3%

The amount of enhancement was determined by applying a cut-off threshold to the processed spectral data and finding the number of SERS spectra that contained a peak

above this threshold. The threshold cut off value was set 25% above the baseline noise of each dataset, which was determined using the baselined and normalized spectral plots. The nanocubes provided the most SERS spectra that were over the cut-off threshold, indicating that they provided the largest enhancement more often than the other nanostructures (Tables 9 and 10). Although the rate of SERS spectra occurrence may be lower than nanowires, the SERS spectra produced by the nanocubes, on average, showed greater enhancement over all the Raman bands associated with both dye molecules. The increased amount of enhancement was expected due to the increased number of sharp edges and corners observed in the nanocubes when compared to the nanoplates followed by the nanowires. Given the sharp edges and corners of the nanocubes, this difference in enhancement is somewhat expected when comparing the nanocubes to nanowires. Conversely, this theory of sharp edges and corners was not supported by the spectra for the nanoplates as they showed less spectra above the threshold than the nanowires. The nanowires were expected to produce weaker SERS enhancement as they possess the least number of sharp edges and corners. These results suggested that the factors influencing SERS enhancement were more nuanced than originally expected and other physical properties of the nanostructures are impacting their ability to produce SERS enhancement.

Table 9: Table of high intensity SERS spectra occurrence in R6G data

Table of R6G high intensity SERS spectra occurrence			
	Nanocubes	Nanowires	Nanoplates
Total SERS spectra	526	903	734
Total high intensity Spectra	261	264	168
High intensity SERS spectra : Total SERS spectra ratio	0.496	0.292	0.229
High intensity SERS spectra : Total SERS spectra percentage	49.6%	29.2%	22.9%

Table 10: Table of high intensity SERS spectra occurrence in CV data

Table of CV high intensity SERS spectra occurrence			
	Nanocubes	Nanowires	Nanoplates
Total SERS spectra	706	790	572
Total high intensity spectra	298	344	215
High intensity SERS spectra : Total SERS spectra ratio	0.422	0.435	0.376
High intensity SERS spectra : Total SERS spectra percentage	42.2%	43.5%	37.6%

The immediate property that could be impacting the quality of SERS enhancement for the nanoplates was their size and thickness. The nanoplates were substantially thinner than the other structures, which may lead to inferior stability while inside the focal volume of the laser. The kinetic calculations for determine the time a nanostructure spent inside the focal volume were assuming a cubic structure, so it was possible that given the size difference between the nanoplates and nanocubes the nanoplates spend less time inside the focal volume than the nanocubes. If the time spent inside the focal volume was lower than the exposure time of the spectrometer than only a partial signal would be collected as the nanoplates travel rapidly through the focal volume, rather than remain in the volume long enough to have their signal collected by the spectrometer. The nanoplates may also suffer from thermal instability when inside the focus of the laser. As they have already been shown to fold, it is possible that the energy exerted on the nanoplates via the laser could disrupt their crystal structure, causing damage that may negatively impact the SERS enhancement.

Lastly the variance parameter was investigated using the statistical analysis outputs. Primarily, the array of Score's plots and the self-organizing map plots provided the greatest insight into how the data points relate to one another and whether any clustering exists inside the data. The initial hypothesis of the existence of distinctly different SERS spectra based on the location the dye molecule on the SERS substrate did not appear to be supported by the experimental data, as no distinct consistent clustering was observed for either of the dye molecules over the different nanostructures. Instead of the theorised discrete number of clusters of SERS spectra, which was expected given the three different regions on the nanostructures, the most observed data distribution was a broad continuum of data points that contained SERS spectra at each of the extremes. These data points were spectrally different from each other while the spectra inside the continuum were an amalgamation of the spectra at the extremes. The spectra at the extremes may have originated from dye molecules isolated to one of the three regions, while the spectra in the body of the continuum may arise from dye molecules located at multiple regions. A portion of the data used in all three nanostructure experiments was within the single molecule concentration range ($1x10^{-11}$ – $1x10^{-13}$ M), meaning that only a single dye

molecule should be present on the nanostructure during SERS collection. Assuming the theory of region-specific SERS signals was accurate then the single molecule data should only contain 3 spectra, one representing each of the different regions on the nanostructures, faces, edges and corners. Given the appearance of PCA outputs for all nanostructures this was obviously not the case, as the single molecule data conforms with the continuum theory expressed by the higher concentration data. This theory was tested further by lower the concentration even further to $1x10^{-14}$ M and $1x10^{-15}$ M, but similar results were observed, with the data conforming closer to the continuum theory than the cluster theory.

CHAPTER 9

Conclusion

All but one of the research aims were achieved during the course of this research. Three novel Ag nanostructures were successfully synthesised, each of which containing sharp edges and corners, while maintaining a small size and shape distribution. These nanostructures were then successfully used as substrates in a variety of SERS experiments with the data collected from these experiments being analysed and used to draw conclusions from. The only aim that was not achieved was the development of a Raman tweezer setup that would have been used to investigate the collection of SERS data from a single molecule on a single crystal. Unfortunately the development of this setup was a more complex task than originally anticipated and the limited time frame of the project meant that there was simply not enough time to fully investigate the Raman tweezers setup.

The original hypothesis of the project did not appear to be supported by the SERS data collected, as none of the different nanostructure:dye molecule permutations displayed any discrete clustering in their respective statistical analysis output. Given the difference in surface area between the three regions on the substrates it was anticipated that three clusters would be present, one large cluster representing face adhered molecules and two smaller clusters representing edge and corner adhered molecules. An idea involving the formation of a continuum of progressively different spectra forming at all regions of the substrate was discussed to possibly account for the appearance of the statistical analysis outputs. Although this idea does not completely account for all observations made from the outputs, it could serve as a starting point for a more complete explanation for what

is occurring during SERS signal generation. Even though the hypothesis for this project was not supported by the experimental evidence, the results of this project provided insight into both the synthesis of several different Ag nanostructures and SERS generation at the single molecule scale. Both of these insights could be built upon by future students to construct a more complete understanding for how the different substrate regions impact SERS generation. Given the success of the nanostructure synthesis portion of the project the results of this work could be used to complete the optical tweezers experiment that was not completed during this project. As the decorated silica spheres were successful trapped using optical tweezers it should be theoretically possible to continue this work and collect SERS data from trapped spheres. The synthesis of each AgNS in this project had been extensively researched and documented in literature, along with their use in SERS experiments. Where this project built on the literature was in the extremely low concentration SERS experiments and the decoration of silica spheres with controlled uniform AgNS. Current literature pertaining to this topic involved the deposition of irregular Ag spherical particles onto the surface and did not take into consideration the final structure of the AgNS once adhered to the silica surface. Raman tweezers have also been extensively researched but the collection of SERS from controlled uniform AgNS while trapped using optical tweezers has not been researched as extensively. As the Raman tweezers experiment was not completed during this project, future researchers can continue this work using the results discussed in this thesis.

Bibliography

(1) Jensen, L.; Aikens, C. M.; Schatz, G. C. *Chemical Society Reviews* **2008**, *37*, Publisher: The Royal Society of Chemistry, 1061–1073, DOI: 10.1039/B706023H (cited on page 2).

(2) Zhao, J.; Jensen, L.; Sung, J.; Zou, S.; Schatz, G. C.; Van Duyne, R. P. *Journal of the American Chemical Society* **2007**, *129*, Publisher: American Chemical Society, 7647–7656, DOI: 10.1021/ja0707106 (cited on page 2).

(3) Hokr, B. H.; Bixler, J. N.; Noojin, G. D.; Thomas, R. J.; Rockwell, B. A.; Yakovlev, V. V.; Scully, M. O. *Proceedings of the National Academy of Sciences* **2014**, *111*, Publisher: National Academy of Sciences Section: Physical Sciences, 12320–12324, DOI: 10.1073/pnas.1412535111 (cited on page 4).

(4) Ong, T. T. X.; Blanch, E. W.; Jones, O. A. H. *Science of The Total Environment* **2020**, *720*, 137601, DOI: 10.1016/j.scitotenv.2020.137601 (cited on page 4).

(5) Schatz, G. C.; Young, M. A.; Van Duyne, R. P. In *Surface-Enhanced Raman Scattering: Physics and Applications*, Kneipp, K., Moskovits, M., Kneipp, H., Eds.; Topics in Applied Physics; Springer: Berlin, Heidelberg, 2006, pp 19–45, DOI: 10.1007/3-540-33567-6_2 (cited on page 6).

(6) Trivedi, D. J.; Barrow, B.; Schatz, G. C. *The Journal of Chemical Physics* **2020**, *153*, Publisher: American Institute of Physics, 124706, DOI: 10.1063/5.0023359 (cited on page 6).

(7) Wang, X.; Huang, S.-C.; Hu, S.; Yan, S.; Ren, B. *Nature Reviews Physics* **2020**, *2*, 253–271, DOI: 10.1038/s42254-020-0171-y (cited on page 6).

(8) Kelley, A. M. *The Journal of Chemical Physics* **2008**, *128*, Publisher: American Institute of Physics, 224702, DOI: 10.1063/1.2931540 (cited on page 6).

(9) Sriram, S.; Bhaskaran, M.; Chen, S.; Jayawardhana, S.; Stoddart, P. R.; Liu, J. Z.; Medhekar, N. V.; Kalantar-Zadeh, K.; Mitchell, A. *Journal of the American Chemical Society* **2012**, *134*, Publisher: American Chemical Society, 4646–4653, DOI: 10.1021/ja208893q (cited on page 6).

(10) Ding, S.-Y.; Yi, J.; Li, J.-F.; Ren, B.; Wu, D.-Y.; Panneerselvam, R.; Tian, Z.-Q. *Nature Reviews Materials* **2016**, *1*, 1–16, DOI: 10.1038/natrevmats.2016.21 (cited on page 6).

(11) Park, W.-H.; Kim, Z. H. *Nano Letters* **2010**, *10*, Publisher: American Chemical Society, 4040–4048, DOI: 10.1021/nl102026p (cited on pages 6, 11).

(12) Dykstra, H. M.; Hall, S. B.; Waterland, M. R. *Journal of Raman Spectroscopy* **2017**, *48*, 405–412, DOI: 10.1002/jrs.5050 (cited on page 7).

(13) A. Dmitriev, P.; G. Baranov, D.; A. Milichko, V.; V. Makarov, S.; S. Mukhin, I.; K. Samusev, A.; E. Krasnok, A.; A. Belov, P.; S. Kivshar, Y. *Nanoscale* **2016**, *8*, Publisher: Royal Society of Chemistry, 9721–9726, DOI: 10.1039/C5NR07965A (cited on page 7).

(14) Cao, Y.; Zhang, J.; Yang, Y.; Huang, Z.; Long, N. V.; Fu, C. *Applied Spectroscopy Reviews* **2015**, *50*, 499–525, DOI: 10.1080/05704928.2014.923901 (cited on page 7).

(15) Jain, P. K.; Huang, X.; El-Sayed, I. H.; El-Sayed, M. A. *Accounts of Chemical Research* **2008**, *41*, Publisher: American Chemical Society, 1578–1586, DOI: 10.1021/ar7002804 (cited on page 7).

(16) Li, Z.; Li, Z.; Li, C.; Li, C.; Yu, J.; Li, Z.; Zhao, X.; Liu, A.; Jiang, S.; Yang, C.; Zhang, C.; Zhang, C.; Man, B.; Man, B. *Optics Express* **2020**, *28*, Publisher: Optical Society of America, 9174–9185, DOI: 10.1364/OE.389886 (cited on page 7).

(17) Li, Y.; Bai, H.; Zhai, J.; Yi, W.; Li, J.; Yang, H.; Xi, G. *Analytical Chemistry* **2019**, *91*, Publisher: American Chemical Society, 4496–4503, DOI: 10.1021/acs.analchem.8b05282 (cited on page 7).

(18) Kelly, K. L.; Coronado, E.; Zhao, L. L.; Schatz, G. C. *The Journal of Physical Chemistry B* **2003**, *107*, Publisher: American Chemical Society, 668–677, DOI: 10.1021/jp026731y (cited on page 8).

(19) Agrawal, A.; Kriegel, I.; Milliron, D. J. *The Journal of Physical Chemistry C* **2015**, *119*, Publisher: American Chemical Society, 6227–6238, DOI: 10.1021/acs.jpcc.5b01648 (cited on page 8).

(20) Ringe, E.; Zhang, J.; Mark, R. L.; Sohn, K.; Cobley, C.; Au, L.; Xia, Y.; Chad, A. M.; Huang, J.; Laurence, D. M.; Van Richard, P. D. *MRS Online Proceedings Library* **2010**, *1208*, 1002, DOI: 10.1557/PROC-1208-O10-02 (cited on page 8).

(21) Rycenga, M.; Camargo, P. H. C.; Li, W.; Moran, C. H.; Xia, Y. *The journal of physical chemistry letters* **2010**, *1*, 696–703, DOI: 10.1021/jz900286a (cited on page 8).

(22) Choi, H.-K.; Lee, K. S.; Shin, H.-H.; Koo, J.-J.; Yeon, G. J.; Kim, Z. H. *Accounts of Chemical Research* **2019**, *52*, Publisher: American Chemical Society, 3008–3017, DOI: 10.1021/acs.accounts.9b00358 (cited on page 9).

(23) Nie, S.; Emory, S. R. *Science* **1997**, *275*, Publisher: American Association for the Advancement of Science Section: Report, 1102–1106, DOI: 10.1126/science.275.5303.1102 (cited on page 9).

(24) Ru, E. L.; Etchegoin, P., *Principles of Surface-Enhanced Raman Spectroscopy: and Related Plasmonic Effects*; Elsevier: 2008; 688 pp. (cited on page 9).

(25) Artur, C.; Le Ru, E. C.; Etchegoin, P. G. *The Journal of Physical Chemistry Letters* **2011**, *2*, Publisher: American Chemical Society, 3002–3005, DOI: 10.1021/jz2013787 (cited on page 9).

(26) Zhang, Z.; Deckert-Gaudig, T.; Singh, P.; Deckert, V. *Chemical Communications* **2015**, *51*, 3069–3072, DOI: 10.1039/C4CC09008J (cited on page 9).

(27) Lindquist, N. C.; de Albuquerque, C. D. L.; Sobral-Filho, R. G.; Paci, I.; Brolo, A. G. *Nature Nanotechnology* **2019**, *14*, 981–987, DOI: 10.1038/s41565-019-0535-6 (cited on page 10).

(28) Doering, W. E.; Nie, S. *The Journal of Physical Chemistry B* **2002**, *106*, Publisher: American Chemical Society, 311–317, DOI: 10.1021/jp011730b (cited on page 10).

(29) Applegate, R. W.; Marr, D. W. M.; Squier, J.; Graves, S. W. *Optics Express* **2009**, *17*, 16731–16738, DOI: 10.1364/OE.17.016731 (cited on page 10).

(30) S. Indrasekara, A. S. D.; Meyers, S.; Shubeita, S.; C. Feldman, L.; Gustafsson, T.; Fabris, L. *Nanoscale* **2014**, *6*, Publisher: Royal Society of Chemistry, 8891–8899, DOI: 10.1039/C4NR02513J (cited on page 11).

(31) Tang, Y.; Zeng, X.; Liang, J. *Journal of chemical education* **2010**, *87*, 742–746, DOI: 10.1021/ed100186y (cited on page 11).

(32) Kunwar, S.; Pandey, P.; Pandit, S.; Sui, M.; Lee, J. *Applied Surface Science* **2020**, *504*, 144545, DOI: 10.1016/j.apsusc.2019.144545 (cited on page 11).

(33) Dong, Z.-G.; Liu, H.; Li, T.; Zhu, Z.-H.; Wang, S.-M.; Cao, J.-X.; Zhu, S.-N.; Zhang, X. *Physical Review B* **2009**, *80*, Publisher: American Physical Society, 235116, DOI: 10.1103/PhysRevB.80.235116 (cited on page 12).

(34) Tian, Z.-Q.; Ren, B.; Wu, D.-Y. *The Journal of Physical Chemistry B* **2002**, *106*, Publisher: American Chemical Society, 9463–9483, DOI: 10.1021/jp0257449 (cited on page 12).

(35) Wang, Y.; Wan, D.; Xie, S.; Xia, X.; Huang, C. Z.; Xia, Y. *ACS NANO* **2013**, *7*, Place: 1155 16TH ST, NW, WASHINGTON, DC 20036 USA Publisher: AMER CHEMICAL SOC Type: Article, 4586–4594, DOI: 10.1021/nn401363e (cited on pages 12, 18, 19, 23, 67, 69).

(36) Lee, K.-S.; El-Sayed, M. A. *The Journal of Physical Chemistry. B* **2006**, *110*, 19220–19225, DOI: 10.1021/jp062536y (cited on page 12).

(37) González, A. L.; Noguez, C. *physica status solidi c* **2007**, *4*, 4118–4126, DOI: 10.1002/pssc.200675903 (cited on page 12).

(38) Choudhary, M. K.; Kataria, J.; Sharma, S. *Journal of Cleaner Production* **2018**, *198*, 882–890, DOI: 10.1016/j.jclepro.2018.09.015 (cited on page 12).

(39) Kim, J. S.; Kuk, E.; Yu, K. N.; Kim, J.-H.; Park, S. J.; Lee, H. J.; Kim, S. H.; Park, Y. K.; Park, Y. H.; Hwang, C.-Y.; Kim, Y.-K.; Lee, Y.-S.; Jeong, D. H.; Cho, M.-H. *Nanomedicine: Nanotechnology, Biology and Medicine* **2007**, *3*, 95–101, DOI: 10.1016/j.nano.2006.12.001 (cited on page 12).

(40) Mogensen, K. B.; Kneipp, K. *The Journal of Physical Chemistry C* **2014**, *118*, Publisher: American Chemical Society, 28075–28083, DOI: 10.1021/jp505632n (cited on page 12).

(41) McLellan, J. M.; Li, Z.-Y.; Siekkinen, A. R.; Xia, Y. *Nano Letters* **2007**, *7*, Publisher: American Chemical Society, 1013–1017, DOI: 10.1021/nl070157q (cited on pages 13, 14).

(42) Hao, E.; Schatz, G. C. *The Journal of Chemical Physics* **2004**, *120*, 357–366, DOI: 10.1063/1.1629280 (cited on page 13).

(43) Rycenga, M.; Kim, M. H.; Camargo, P. H. C.; Cobley, C.; Li, Z.-Y.; Xia, Y. *The journal of physical chemistry. A* **2009**, *113*, 3932–3939, DOI: 10.1021/jp8101817 (cited on page 14).

(44) Rycenga, M.; Cobley, C. M.; Zeng, J.; Li, W.; Moran, C. H.; Zhang, Q.; Qin, D.; Xia, Y. *Chemical Reviews* **2011**, *111*, Publisher: American Chemical Society, 3669–3712, DOI: 10.1021/cr100275d (cited on page 14).

(45) Lee, S.; Kim, H.; Lee, J.; Kim, C. *Optics Express* **2017**, *25*, Publisher: Optical Society of America, 9105–9115, DOI: 10.1364/OE.25.009105 (cited on page 15).

(46) Zhang, Y.; Shen, J.; Xie, Z.; Dou, X.; Min, C.; Lei, T.; Liu, J.; Zhu, S.; Yuan, X. *NANOSCALE* **2017**, *9*, Place: THOMAS GRAHAM HOUSE, SCIENCE PARK, MILTON RD, CAMBRIDGE CB4 0WF, CAMBS, ENGLAND Publisher: ROYAL SOC CHEMISTRY Type: Article, 10694–10700, DOI: 10.1039/c7nr02406a (cited on page 15).

(47) Murphy, C. J.; Jana, N. R. *Advanced Materials* **2002**, *14*, 80–82, DOI: https://doi.org/10.1002/1521-4095(20020104)14:1<80::AID-ADMA80>3.0.CO;2-# (cited on page 15).

(48) Kan, C.-X.; Zhu, J.-J.; Zhu, X.-G. *Journal of Physics D: Applied Physics* **2008**, *41*, Publisher: IOP Publishing, 155304, DOI: 10.1088/0022-3727/41/15/155304 (cited on pages 15, 22, 25, 27).

(49) Kumar, G.; Soni, R. K. *Plasmonics* **2020**, *15*, 1577–1589, DOI: 10.1007/s11468-020-01172-0 (cited on page 15).

(50) Liu, X.; Li, L.; Yang, Y.; Yin, Y.; Gao, C. *Nanoscale* **2014**, *6*, Publisher: The Royal Society of Chemistry, 4513–4516, DOI: 10.1039/C4NR00254G (cited on pages 17, 27, 28, 30, 36).

(51) Zou, X.; Dong, S. *The Journal of Physical Chemistry B* **2006**, *110*, Publisher: American Chemical Society, 21545–21550, DOI: 10.1021/jp063630h (cited on page 17).

(52) Zhou, S.; Li, J.; Gilroy, K. D.; Tao, J.; Zhu, C.; Yang, X.; Sun, X.; Xia, Y. *ACS Nano* **2016**, *10*, Publisher: American Chemical Society, 9861–9870, DOI: 10.1021/acsnano.6b05776 (cited on pages 17, 21, 29).

(53) Tian, Y.; Liu, H.; Chen, Y.; Zhou, C.; Jiang, Y.; Gu, C.; Jiang, T.; Zhou, J. *Sensors and Actuators B: Chemical* **2019**, *301*, 127142, DOI: 10.1016/j.snb.2019.127142 (cited on page 19).

(54) Chen, Z.; Balankura, T.; Fichthorn, K. A.; Rioux, R. M. *ACS Nano* **2019**, *13*, Publisher: American Chemical Society, 1849–1860, DOI: 10.1021/acsnano.8b08019 (cited on pages 20, 22).

(55) Zhang, Q.; Li, W.; Wen, L.-P.; Chen, J.; Xia, Y. *Chemistry (Weinheim an der Bergstrasse, Germany)* **2010**, *16*, Publisher: NIH Public Access, 10234, DOI: 10.1002/chem.201000341 (cited on pages 21, 23, 24, 35, 67, 70).

(56) Wang, Y.; Zheng, Y.; Huang, C. Z.; Xia, Y. *Journal of the American Chemical Society* **2013**, *135*, Publisher: American Chemical Society, 1941–1951, DOI: 10.1021/ja311503q (cited on pages 21, 66).

(57) Zhang, Q.; Li, W.; Moran, C.; Zeng, J.; Chen, J.; Wen, L.-P.; Xia, Y. *Journal of the American Chemical Society* **2010**, *132*, 11372–11378, DOI: 10.1021/ja104931h (cited on pages 21, 23).

(58) Ghosh, S.; Manna, L. *Chemical Reviews* **2018**, *118*, Publisher: American Chemical Society, 7804–7864, DOI: 10.1021/acs.chemrev.8b00158 (cited on page 21).

(59) Xia, Y.; Xiong, Y.; Lim, B.; Skrabalak, S. E. *Angewandte Chemie (International Ed. in English)* **2009**, *48*, 60–103, DOI: 10.1002/anie.200802248 (cited on pages 22, 29).

(60) Cousins, C. S. G. *Nature* **1980**, *283*, 751–752, DOI: 10.1038/283751a0 (cited on page 22).

(61) Rekha, C. R.; Nayar, V. U.; Gopchandran, K. G. *Journal of Science: Advanced Materials and Devices* **2018**, *3*, 196–205, DOI: 10.1016/j.jsamd.2018.03.003 (cited on page 22).

(62) Koczkur, K. M.; Mourdikoudis, S.; Polavarapu, L.; Skrabalak, S. E. *Dalton Transactions* **2015**, *44*, Publisher: The Royal Society of Chemistry, 17883–17905, DOI: 10.1039/C5DT02964C (cited on page 22).

(63) Marks, L. D. *Reports on Progress in Physics* **1994**, *57*, Publisher: IOP Publishing, 603–649, DOI: 10.1088/0034-4885/57/6/002 (cited on page 23).

(64) Niu, W.; Zhang, L.; Xu, G. *Nanoscale* **2013**, *5*, Publisher: The Royal Society of Chemistry, 3172–3181, DOI: 10.1039/C3NR00219E (cited on page 24).

(65) Sun, Y.; Mayers, B.; Herricks, T.; Xia, Y. *Nano Letters* **2003**, *3*, Publisher: American Chemical Society, 955–960, DOI: 10.1021/nl034312m (cited on page 25).

(66) Huang, H. H.; Ni, X. P.; Loy, G. L.; Chew, C. H.; Tan, K. L.; Loh, F. C.; Deng, J. F.; Xu, G. Q. *Langmuir* **1996**, *12*, Publisher: American Chemical Society, 909–912, DOI: 10.1021/la950435d (cited on page 26).

(67) Métraux, G. S.; Mirkin, C. A. *Advanced Materials* **2005**, *17*, 412–415, DOI: 10.1002/adma.200401086 (cited on page 27).

(68) Zhang, Q.; Li, N.; Goebl, J.; Lu, Z.; Yin, Y. *Journal of the American Chemical Society* **2011**, *133*, 18931–18939, DOI: 10.1021/ja2080345 (cited on page 28).

(69) Hofmeister, H. *Crystal Research and Technology* **1998**, *33*, 3–25, DOI: 10.1002/(SICI)1521-4079(1998)33:1<3::AID-CRAT3>3.0.CO;2-3 (cited on page 28).

(70) Yu, D.; Yam, V. W.-W. *Journal of the American Chemical Society* **2004**, *126*, Publisher: American Chemical Society, 13200–13201, DOI: 10.1021/ja046037r (cited on page 28).

(71) Najafi, M.; Yousefi, Y.; Rafati, A. A. *Separation and Purification Technology* **2012**, *85*, 193–205, DOI: 10.1016/j.seppur.2011.10.011 (cited on page 37).

(72) Ward, R. L.; Williams, M. A. K. *Microfluidics and Nanofluidics* **2021**, *25*, 50, DOI: 10.1007/s10404-021-02452-9 (cited on page 39).

(73) Sherry, L. J.; Chang, S.-H.; Schatz, G. C.; Van Duyne, R. P.; Wiley, B. J.; Xia, Y. *Nano Letters* **2005**, *5*, Publisher: American Chemical Society, 2034–2038, DOI: 10.1021/nl0515753 (cited on page 45).

(74) Kirubha, E.; Palanisamy, P. K. *Advances in Natural Sciences: Nanoscience and Nanotechnology* **2014**, *5*, Publisher: IOP Publishing, 045006, DOI: 10.1088/2043-6262/5/4/045006 (cited on page 49).

(75) Huang, D.; Cui, J.; Chen, X. *Colloids and Surfaces A: Physicochemical and Engineering Aspects* **2014**, *456*, 100–107, DOI: 10.1016/j.colsurfa.2014.05.027 (cited on page 49).

(76) Meng, W.; Hu, F.; Jiang, X.; Lu, L. *Nanoscale Research Letters* **2015**, *10*, 34, DOI: 10.1186/s11671-015-0746-1 (cited on page 50).

(77) Jensen, L.; Schatz, G. C. *The Journal of Physical Chemistry A* **2006**, *110*, Publisher: American Chemical Society, 5973–5977, DOI: 10.1021/jp0610867 (cited on page 50).

(78) Upender, G.; Sathyavathi, R.; Raju, B.; Bansal, C.; Narayana Rao, D. *Journal of Molecular Structure* **2012**, *1012*, 56–61, DOI: 10.1016/j.molstruc.2011.12.044 (cited on page 50).

(79) Yan, W.; Yang, L.; Chen, J.; Wu, Y.; Wang, P.; Li, Z. *Advanced Materials* **2017**, *29*, 1702893, DOI: 10.1002/adma.201702893 (cited on page 51).

(80) Guo, H.; Li, Z. *Science China Physics, Mechanics and Astronomy* **2013**, *56*, 2351–2360, DOI: 10.1007/s11433-013-5355-3 (cited on page 53).

(81) Hajizadeh, F.; S.Reihani, S. N. *Optics Express* **2010**, *18*, Publisher: Optical Society of America, 551–559, DOI: 10.1364/OE.18.000551 (cited on page 54).

(82) Pearce, K.; Wang, F.; Reece, P. J. *Optics Express* **2011**, *19*, Publisher: Optical Society of America, 25559–25569, DOI: 10.1364/OE.19.025559 (cited on page 54).

(83) Danielsson, P.-E. *Computer Graphics and Image Processing* **1980**, *14*, 227–248, DOI: 10.1016/0146-664X(80)90054-4 (cited on page 62).

(84) Wong, M. L. D.; Jack, L. B.; Nandi, A. K. *Mechanical Systems and Signal Processing* **2006**, *20*, 593–610, DOI: 10.1016/j.ymssp.2005.01.008 (cited on page 63).

(85) Kohonen, T. *Neural Networks* **2013**, *37*, 52–65, DOI: 10.1016/j.neunet.2012.09.018 (cited on page 63).

(86) Vettigli, G. MiniSom: minimalistic and NumPy-based implementation of the Self Organizing Map, Github https://github.com/JustGlowing/minisom/ (accessed 12/22/2021) (cited on page 63).

(87) Zhang, P.; Wyman, I.; Hu, J.; Lin, S.; Zhong, Z.; Tu, Y.; Huang, Z.; Wei, Y. *Materials Science and Engineering: B* **2017**, *223*, 1–23, DOI: 10.1016/j.mseb.2017.05.002 (cited on page 93).

(88) Liu, L.; Wu, Y.; Yin, N.; Zhang, H.; Ma, H. *Journal of Quantitative Spectroscopy and Radiative Transfer* **2020**, *240*, 106682, DOI: 10.1016/j.jqsrt.2019.106682 (cited on page 107).